NSF Grant ATM-9015485, ATM-9321361
National Science Foundation

DOPPLER RADAR OBSERVATIONS OF AN ASYMMETRIC MCS AND ASSOCIATED VORTEX COUPLET

by James D. Scott

Steven A. Rutledge, P.I.

Colorado State University

DEPARTMENT OF ATMOSPHERIC SCIENCE

PAPER NO. 566

DOPPLER RADAR OBSERVATIONS OF AN ASYMMETRIC MCS AND ASSOCIATED VORTEX COUPLET

by

James D. Scott

Department of Atmospheric Science

Colorado State University

Fort Collins, CO 80523

Research Supported by

National Science Foundation

under Grant ATM-9015485

and ATM-9321361

October, 1994

Atmospheric Science Paper No. 566

ABSTRACT

A study of the 28 May 1985 "asymmetric" mesoscale convective system (MCS) observed during PRE-STORM (Preliminary Regional Experiment for Stormscale Operational and Research Meteorology) is presented. Radar documented the evolution of this MCS from a linear squall line, to a symmetric MCS with a trailing stratiform region, to an asymmetric MCS. Before the transition to the asymmetric stage, shallow, counter-rotating circulations were observed below the melting level in the trailing stratiform region of the system. With time, the anticyclonic circulation in the southern portion of the stratiform cloud began to weaken and migrate toward the convective line, while the northern, cyclonic circulation rapidly intensified, creating a asymmetric precipitation pattern. At maximum extent, the closed cyclonic circulation had horizontal dimensions of 80 km and a depth of 7 km. Retrieved horizontal pressure perturbations depict a pressure minimum in the center of the cyclonic circulation, suggesting the presence of quasi-balanced flow within the vortex. A strong and deep rear inflow jet was closely linked to the amplification and maintenance of the cyclonic vortex. A similar sequence of mesoscale flow evolution has been documented in recent modeling studies.

ACKNOWLEDGEMENTS

I would like to thank my advisor, Dr. Steven A. Rutledge, for his availability for consultation, suggestions, and constructive criticisms on this research. Additional thanks are in order for my other thesis committee members, Dr. Richard H. Johnson and Dr. Richard F. Eykholt.

I would also like to thank Doug Burks for his computer support and Tom Rickenbach for the use of his feature identification subroutine. Scot Loehrer provided valuable assistance with the surface pressure analysis.

A special thanks goes out to Dr. Tom Matejka for his notes on thermodynamic retrieval and Dr. Brian Klimowski for his notes on CEDRIC. This research was supported by the National Science Foundation under grant ATM-9015485.

TABLE OF CONTENTS

LIST OF FIGURES

LIST OF TABLES

Chapter 1

INTRODUCTION

The ability of convective cells to group together to form organized structures much larger and distinct from isolated convection is one of the more prominent examples of upscale interaction. Convection tends to organize in this way when there is low level wind shear and high convective available potential energy (CAPE) in the environment. Early stages of organization are usually facilitated by the presence of boundary layer convergence generated by a density current, such as a frontal boundary, convective outflow boundary, or dry line. Convective systems that organize in this fashion are generally termed mesoscale convective systems (MCSs). Specifically, an MCS has been defined as "a precipitating system that has a horizontal scale of 10-500 km and includes significant convection during some part of its lifetime" (NCAR, 1984). This broad class of convective systems includes squall lines, bow echoes (Fujita 1978) and mesoscale convective complexes (MCCs; Maddox 1980).

A squall line is usually made up of a narrow band of strong convection at the leading edge of the system, with a broad, trailing region of stratiform precipitation (Houze and Hobbs 1982). Occasionally, squall lines have been known to evolve into bow echoes (Fig. 1.1, Fujita 1978). These types of systems have been known to produce damaging straight line winds. The strong surface winds and the bulging of the echo pattern were postulated by Fujita to be associated with a strong rear inflow jet. The declining stage of a bow echo is often characterized by a hook or comma shaped echo, with cyclonic rotation on the northern end of the system.

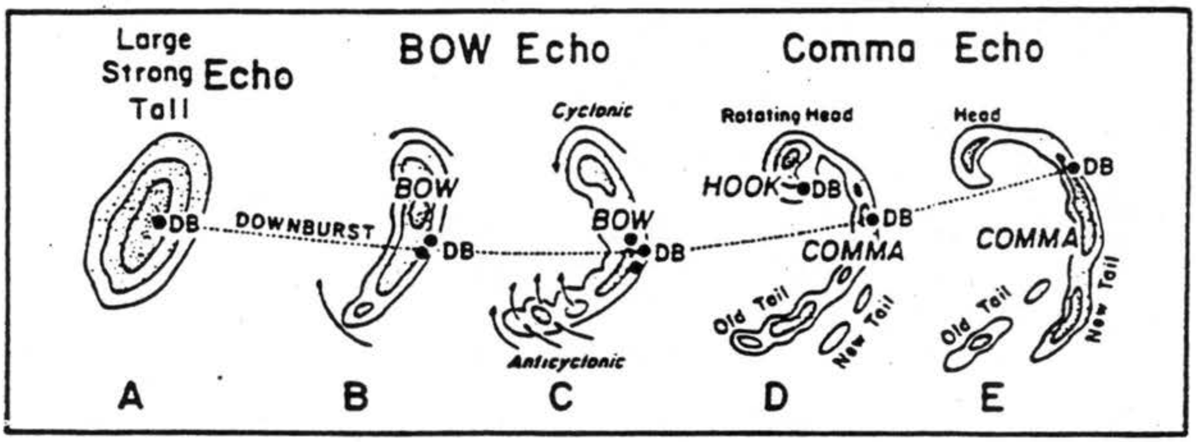

Figure 1.1: A typical morphology of radar echoes associated with bow echoes that produce strong and extensive downbursts, labeled DB on the figure (from Fujita 1978).

The MCC is one of the larger types of MCSs. The criteria for MCCs were developed by Maddox (1980) and are based on the IR-satellite images of the convective system. A satellite based classification scheme was proposed because of the wide range of spatial scales resolved and the ability to easily track a system over long distances. Maddox's criteria (Table 1.1) limit the MCCs to the meso α scale (200-2000 km) in order to make observations using the standard synoptic upper air and surface data sets feasible. These criteria further limit MCCs to long-lived phenomena (>6 hrs.) and make them distinct from linearly organized systems (eccentricity >0.7).

In a composite analysis of 10 MCCs that occurred during the period 1975-1978 over the central US, Maddox (1983) describes the prominent features of these systems. The MCC is spawned in a region of mesoscale ascent east of the Rocky Mountains generated by strong low level warm air and moisture advection and augmented by weak positive vorticity advection at mid-levels. This region is typically south of a surface front. MCCs are largely nocturnal, maturing in association with the strengthening of a southerly low level jet, which enhances the low level warm air and moisture advection into the storm. The duration and intensity of vertical motion associated with MCCs allows them to modify the large scale environment. The mature environment of the MCC is characterized by a deep warm core at mid-levels, associated with strong upward motion, overlain with an upper-level cold core and strong anticyclonic, divergent outflow. The mid-level warm core structure is apparently due to latent heat release in the convective updrafts. Once all the moisture in the updrafts has condensed or frozen, the continued upward motion generates the cold core aloft through adiabatic expansion. Cloud top radiative cooling may also contribute to the upper-level temperature perturbation (Chen and Cotton 1988, Johnson *et al.* 1990). Low levels of the MCC environment are characterized by a cool mesohigh, which is generated by the melting and evaporation of precipitation. Upper-level and low-level temperature perturbations and enhanced mid-level positive vorticity often persist after the MCC has decayed. The enhancement of the

Table 1.1: Criteria used to identify Midlatitude Mesoscale Convective Complexes in Infrared satellite data (from Maddox 1980).

	Physical Characteristics
Size:	(A) Cloud shield with continuously low infrared temperature ≤ - 32 °C must have an area ≥ 100,000 km^2 (B) Interior cold cloud region with temperature ≤ - 52 °C must have and area ≥ 50,000 km^2
Initiate:	Size definitions (A) and (B) are first satisfied
Duration:	Size definitions (A) and (B) must be satisfied for a period ≥ 6 hr
Maximum Extent:	Contiguous cold cloud shield (infrared temperature ≤ - 32 °C reaches maximum size
Shape:	Eccentricity (minor axis/major axis) ≥0.7 at time of maximum extent
Terminate:	Size definitions (A) and (B) no longer satisfied

mid-level positive vorticity or short-wave trough was attributed to a large-scale adjustment to the temperature anomaly.

A more extensive composite study of 90 MCCs by Cotton *et al.* (1989) confirmed and expanded upon the findings of Maddox. Their larger data set allowed for a more detailed breakdown of the life cycle of MCCs. During the initial stage of the MCCs, Cotton *et al.* observed peak upward motion near 700 mb and an apparent heat source of 9-12 °C day^{-1} near 850 mb. An intensification of positive vorticity in the surface to 700 mb layer and negative vorticity in the upper troposphere were also observed. During the mature stage, the precipitation efficiency exceeded 100%, as moisture accumulated during the growth stage of the system is released. The enhanced precipitation contributes to a low and mid-level apparent heat sink of -6 to -9 °C day^{-1}, mainly due to evaporation and melting of the precipitation. The decay of the system is initiated as it moves into a region of less low-level moisture and higher stability. Middle-tropospheric cyclonic and upper-tropospheric anticyclonic circulations continue to amplify during the decay stage, apparently due to a delayed adjustment to the strong thermal perturbations generated by the mature stage. This adjustment is attributed to the fact that the average "dynamic radius" (322 km) of the MCCs analyzed exceeded the estimated Rossby radius (300 km) by ~20 km. Under these circumstances the wind field will adjust to perturbations in the mass field (Schubert 1980). This led Cotton *et al.* to define MCCs based on dynamic criteria: "A mature MCC represents an inertially stable mesoscale convective system which is nearly geostrophically balanced and whose horizontal scale is comparable to or greater than the Rossby radius".

The limitation of using satellite and conventional sounding data to document MCSs is that they do not provide high resolution detail of the internal structure and kinematics of these systems. The use of radar data often provides detail not seen in satellite imagery, especially in the case of a mature MCS, where a large cold-cloud shield obscures the mid- and low-level features of the MCS from the satellite perspective. There have been relatively few attempts to develop a climatology of MCSs from the radar perspective. One such study (Houze *et al.* 1990) documented the characteristics of MCSs using the Oklahoma City National Weather Service WSR-57 radar for six consecutive years for the period of April-June each year. The authors of this study looked at the organizational structure of mesoscale convective systems that were considered "major rain events". A major rain event was defined as a 24 hour period that accumulated >25 mm of rain over at least 10% of the study area. In their analysis, Houze *et al.* (1990) determined that approximately 2/3 of the 51 cases examined were organized enough to be classifiable. There were two distinct types of organization, each accounting for approximately 1/3 of the cases.

The first type was classified as the symmetric case (Fig. 1.2). This type of organization exhibits no preference for the location of the most intense cells along the line and new cell formation occurs at the leading edge of the system. A trailing stratiform region follows the center of the convective line. There have been numerous more detailed studies of MCSs that exhibit this type of precipitation structure. A classic case is one presented by Rutledge *et al.* (1988). This study focused on single-Doppler analysis of an MCS that occurred on 10-11 June, 1985 and was observed during the PRE-STORM experiment (details of the experiment are provided in Chapter 2). One of the most defined features of the system was a strong rear inflow jet which penetrated the back edge of the stratiform region at upper levels and descended through the system, reaching the surface at the convective line (Fig. 1.3). Above this layer of storm-relative rear to front flow was a region of front to rear flow. Mesoscale updrafts were diagnosed in this portion of the storm. A mesoscale downdraft was observed to initiate near the top of the rear inflow jet at varying heights within the stratiform region. It was believed that the dry air entrained by the rear inflow jet generated mesoscale subsidence through the processes of sublimation and evaporation. Strong convergence at the tilted interface of these opposing flows also contributed to downward motion over varying depths within the stratiform

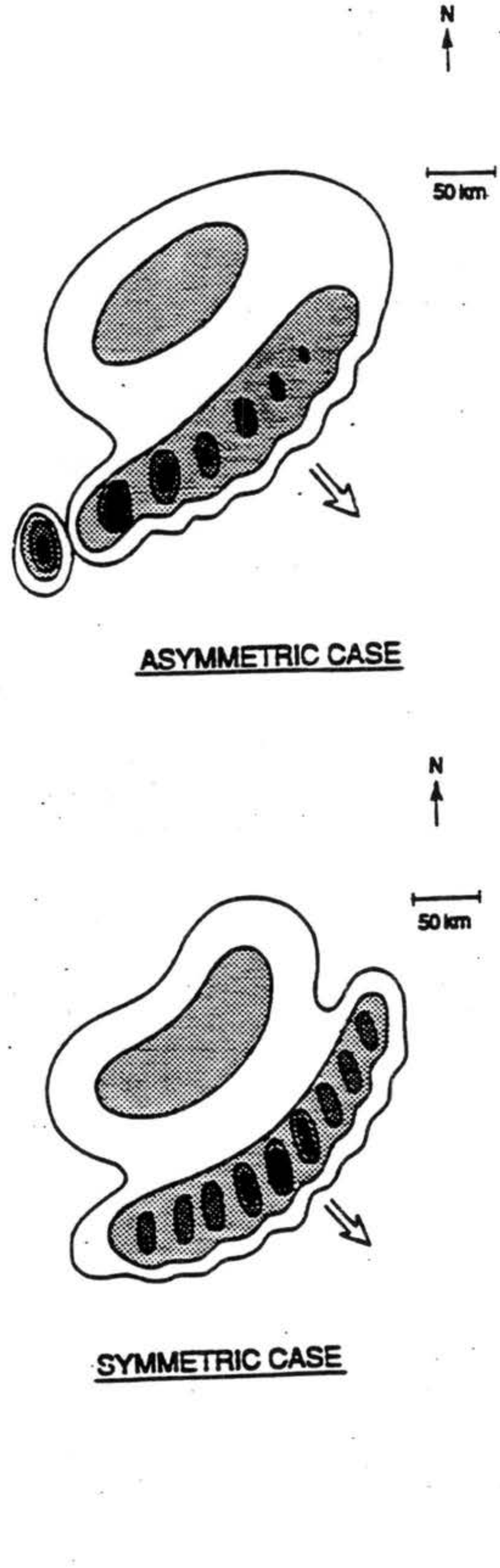

Figure 1.2: Schematic depicting asymmetric (top) and symmetric (bottom) pattern of leading line / trailing stratiform MCS organization (from Houze *et al.* 1990).

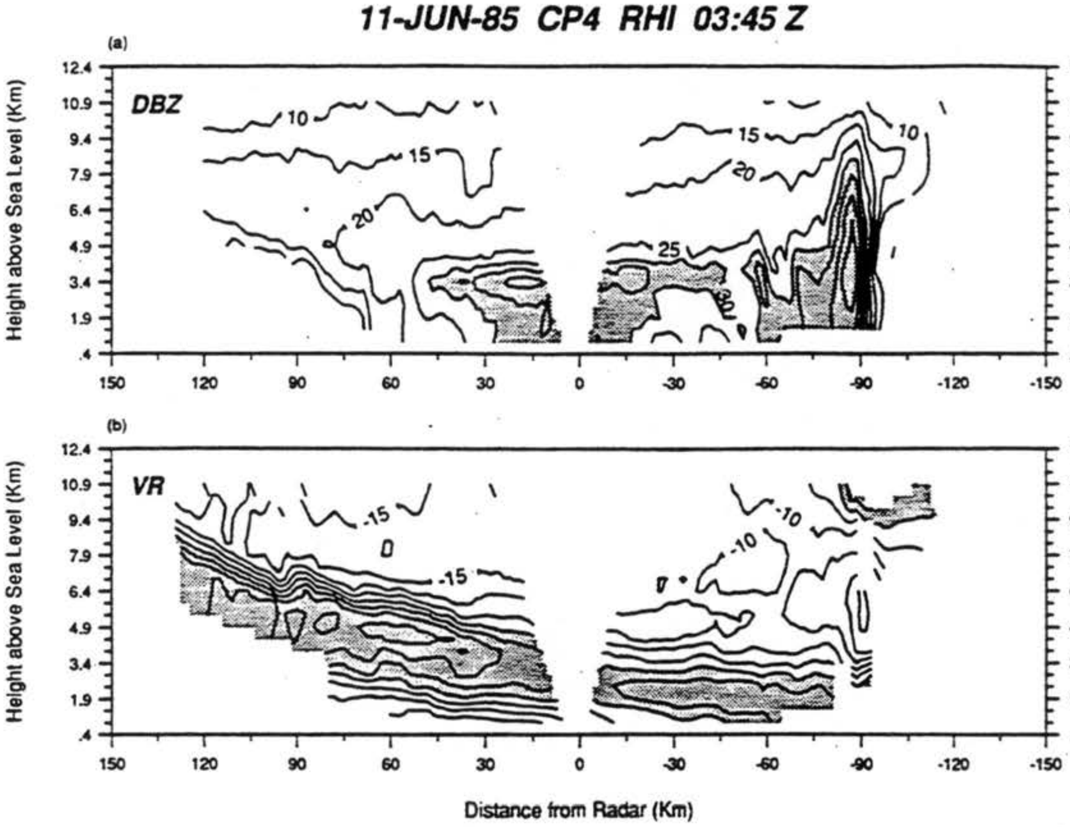

Figure 1.3: Vertical cross sections of reflectivity and horizontal flow along the 300°-120° radials at the CP-4 radar. (a) Reflectivity in dBZ. Contour interval is 5 dBZ. Shading denotes reflectivities > 30 dBZ. (b) Horizontal relative flow in ms^{-1}. Contour interval is 5 ms^{-1}. Shading denotes velocities > 0, or left-to-right motion relative to the storm (from Rutledge *et al.* 1988).

region. The strength and dryness of the rear inflow jet was linked with the intensity of the mesoscale downdraft.

A study by Johnson and Hamilton (1988) focused on the surface pressure features associated with the same symmetric MCS. They diagnosed three distinct surface pressure features associated with the MCS: a pre-squall mesolow, a squall mesohigh, and a wake low (Fig. 1.4). The pre-squall low had previously been attributed to convectively induced subsidence warming ahead of squall lines (Hoxit *et al.* 1976). It has also been generally accepted the squall mesohigh is largely due to the latent cooling of evaporating rainfall (Sawyer 1946, Fujita 1959). The wake low, typically observed on the back edge of the stratiform cloud, has also been attributed to subsidence warming creating a hydrostatic reduction in pressure at the surface. The mechanisms involved in generating this subsidence were the focus of the Johnson and Hamilton (1988) investigation. They found a very close association between the development of a wake low and the development of the stratiform precipitation. A connection was also drawn between the subsiding rear inflow jet and the wake low. They suggest that the wake low is a surface manifestation of the descending rear inflow jet and that the wake low resides on the back edge of the stratiform cloud because subsidence warming is maximized here, as there is insufficient evaporative cooling to offset the adiabatic compression associated with the descending rear inflow.

The second major organizational structure of MCSs was classified by Houze *et al.* (1990) as asymmetric (Fig. 1.2). This type of system had the younger, more intense convective cells on the southern end of the system, with the stratiform region skewed to the north. Strong cyclonic circulations at mid-levels in the trailing stratiform region of asymmetric MCSs have been documented numerous times and are responsible for the highly asymmetric precipitation patterns associated with the asymmetric MCS. These cyclonic circulations, termed mesoscale convectively-generated vortices, or MCVs (Menard and Fritsch 1989), are the subject of the following background study.

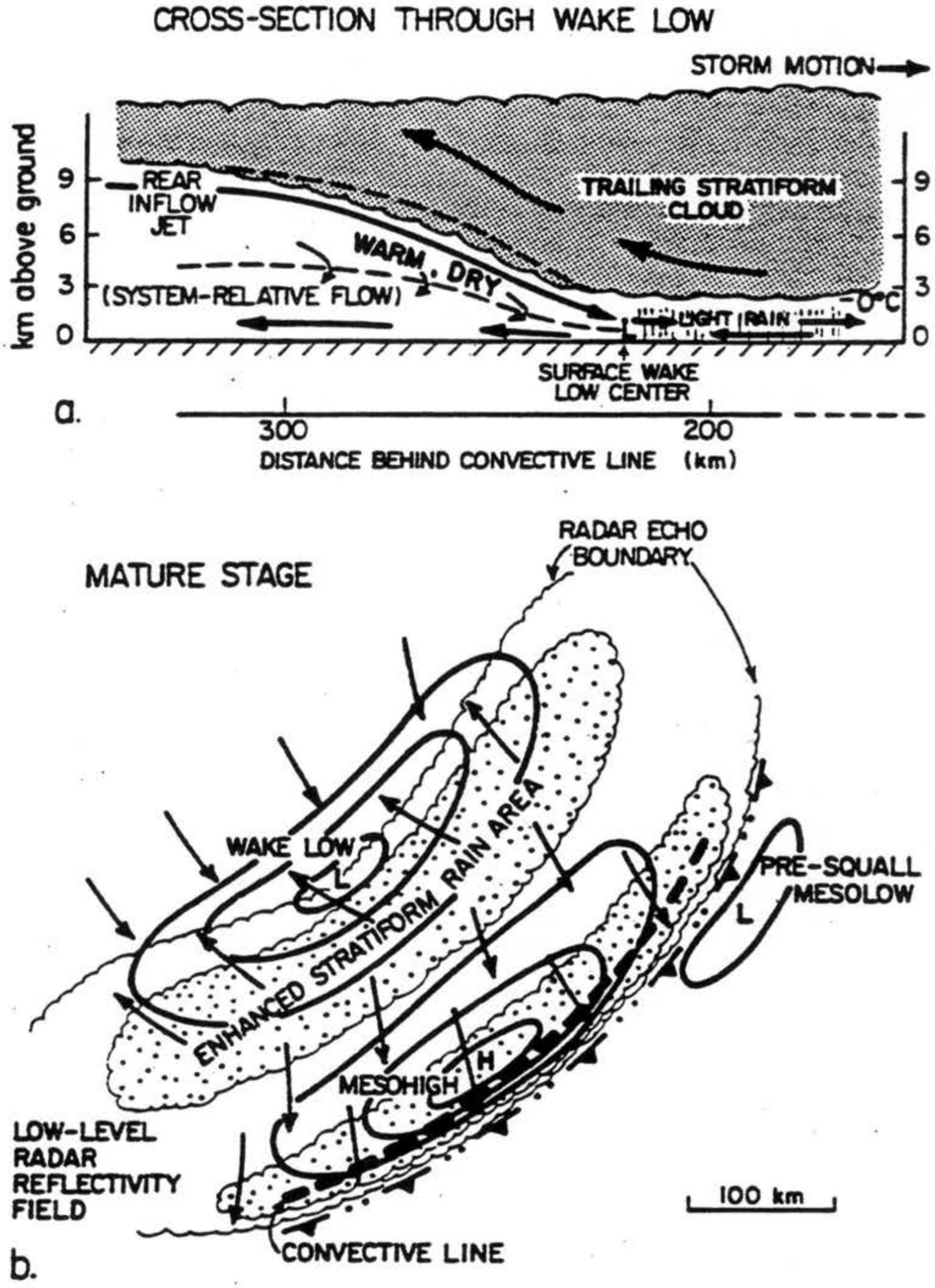

Fig. 1.4: Schematic cross section through a wake low (a) and surface pressure and wind fields and precipitation distribution during squall line mature stage (b). Winds in (a) are system-relative with the dashed line denoting zero relative wind. Arrows indicate streamlines, not trajectories, with those in (b) representing actual winds. Note that horizontal scales of the two schematics are not the same (from Johnson and Hamilton 1988).

MCVs were apparently first identified in satellite imagery by Johnston (1981). Johnston noted strong cyclonic circulations in the low and mid-level cloud patterns of mesoscale convective systems, following the dissipation of the cirrus anvils associated with the mature MCS. There were 26 MCVs documented in his study. IR satellite estimates showed MCVs primarily were located in the 2.5-4.5 km (MSL) layer. The average diameter of the circulations ranged from 50-100 km and the relative vorticity was on the order of $2x10^{-5}$ s^{-1}. The "tropical cyclone-like" circulations persisted for long periods after the parent MCS had dissipated and occasionally appeared to initiate new convection. Johnston's documentation of these features sparked an interest in this subject and many observational and modeling studies on MCVs have followed.

Menard and Fritsch (1989) used satellite imagery and the conventional upper air soundings of the National Weather Service (NWS) to document the evolution of an inertially stable, warm core MCV generated by an MCS. The convection initially was linearly organized along a cold front that was moving into a region of high instability and weak shear. A strong low-level jet was providing an ample supply of moisture to the developing system. The localized area of moisture convergence in vicinity of the low-level jet caused the linearly organized convection to consolidate into an intense MCC. As the MCC began to dissipate, a strong cyclonic circulation was detected in both the satellite and sounding data. At 500 and 700 mb the MCV had a horizontal extent of 1000 km. Height depressions of 5-10 m were observed 100-200 km from the vortex center at these levels. The Rossby number for the disturbance was calculated to be 0.5, indicating there was a significant component of geostrophic balance in the circulation. Weak advection of temperature and vorticity were observed on the large scale, so it is believed that the heat released in the convective system created a balanced response in the wind field, initiating the MCV. The MCV persisted for more than 2 days and its characteristics changed very little over this period. The MCV kinematics consisted of a deep layer of convergence, positive vertical relative vorticity and saturated ascent. The longevity of the circulation was attributed to its inertial stability and a surrounding environment of weak shear.

A more comprehensive study of the general characteristics of MCVs and their environments was performed by Bartels and Maddox (1991). Satellite data was used to identify 24 cases of MCVs over the central US from 1981-1988 and statistics on the structure of the MCVs and their environment were compiled using the NWS sounding network. Their study found the typical genesis environment of MCSs containing MCVs to be characterized by moderate to high values of potential instability, weak vertical shear and weak vorticity advection at 500 mb. The MCVs were typically larger than those found by Johnston (1981), with diameters ranging from 100-400 km. They found the MCV circulations to be warm core, with the most intense rotation at the base of the warm temperature perturbation (typically near the melting level). They suggest that the presence of maximum vorticity at the transition between a warm anomaly above the melting level (due to latent heat release) and a cold anomaly below the melting level (due to evaporative cooling and melting) qualitatively indicates the presence of geostrophic balance in these circulations. The limitations of this study were the density of the upper air observations and the fact that the MCVs were only detectable after the parent MCS had dissipated. Thus the mechanisms involved in the initiation of these circulations could not be explored. More detailed observations of MCVs have been provided by Doppler radar observations and mesoscale sounding networks.

Brandes (1990) used detailed radar observations, mesonet sounding and surface data, as well as satellite and wind profiler data from the PRE-STORM experiment (see Ch. 2 for an overview of this experiment) to document an asymmetric MCS and its associated MCV in unprecedented detail. The synoptic conditions in the genesis environment of this MCS were quite similar to those found by Maddox (1983) for genesis of mesoscale convective complexes described above. The low level reflectivity structure evolved from a symmetric MCS to a highly asymmetric MCS as a mesovortex developed in the trailing stratiform region. Surface pressure features similar to the ones described by Johnson and Hamilton (1988) were also found. Characteristics of the MCV were analyzed using the special sounding network used in PRE-STORM. The vortex core was characterized by positive vorticity over a depth >5 km, with peak values as large as $15 \times 10^{-5}\ s^{-1}$. The positive vorticity was also correlated with mesoscale convergence, leading the author to believe vortex stretching was the primary source of the spinup of the MCV. The mesoscale convergence in the vortex was associated with the mesoscale downdraft, not the mesoscale updraft in this case. Brandes calculated a vortex of this magnitude could be generated through the convergence of the Earth's vorticity in a period of 1.5 hours by the mesoscale convergence observed in this system. The thermodynamic structure of the MCV was found to be somewhat different than in Menard and Fritsch (1989). Below the melting level the vortex was cold core and above the melting level it was warm core. In a follow-up study on the same case, Brandes and Ziegler (1993) propose additional mechanisms for the development of the MCV. They believe an important source of vertical vorticity was created by the tilting of horizontal vorticity that occurred as air entered the mesoscale downdraft. The horizontal vorticity was presumed to be generated by the baroclinicity created by sublimation, evaporation and melting in the stratiform region, which was subsequently tilted into the vertical by the mesoscale downdraft and then enhanced by convergence.

An analysis of an MCV that was closely linked to a synoptic scale short wave using another PRE-STORM data set was performed by Johnson and Bartels (1992). The closed vortex circulation, which had a horizontal diameter of 100 km, formed along the axis of a mid-level trough at the back edge of the trailing stratiform region of the MCS. The MCV was confined between 3-8 km and had a thermodynamic profile that consisted of a warm anomaly above the melting level, a cool anomaly near the melting level and another warm anomaly at low levels, near 850 mb. An analysis of the vorticity budget during the decaying stages of the squall line showed convergent amplification of vorticity was the primary mechanism for the maintenance and intensification of the MCV at this time.

An example of an MCV being diagnosed by airborne Doppler radar is provided by Jorgensen and Smull (1993). This MCV was again spawned in the northern stratiform region of an MCS that developed in advance of a synoptic scale short wave. Kinematic analyses of the circulation show that it had a relative vorticity $>2\text{x}10^{-4}$ s^{-1} on a scale of 100 km. The strongest circulation was near the melting level, yet extended up to 5 km. The southern branch of the circulation was advecting drier air into the rear of the system, creating a distinct notch in the reflectivity field. Strong subsidence warming was also suspected in this region because a wake low was observed below this notching in the reflectivity field. Air motion within the vortex was strongly convergent and downward as it was in the Brandes and Ziegler (1993) study. As in most observational studies of MCVs to date, the system was mature to dissipating at the time of analysis, so there was little information available concerning the development of the MCV circulation. This is why numerical models have been employed to fill the gaps in our knowledge regarding this type of phenomena.

The modeling study by Schubert *et al.* (1980) looked at the problem of geostrophic adjustment in an axisymmetric vortex. The purpose of the study was to demonstrate the relative efficiencies perturbations in the base state momentum or geopotential fields have in contributing to geostrophic flow. They examined varying scales of initial disturbances and concluded that for small scale (relative to the Rossby radius of deformation) momentum disturbances the efficiency of geostrophic energy generation is very high and for small scale heating the efficiency is very low. This means for small scale heating, most of the energy is transferred to gravity waves and little energy is transferred to balanced flow. In order to get an appreciable contribution to geostrophic flow, the heating must be over an area comparable to the Rossby radius of deformation. For example, heating on the scale of the Rossby radius (such as in the stratiform region of a large MCS) would transfer approximately 1/3 of the energy into balanced flow. The rest would be transferred out of the region by gravity wave propagation. Schubert *et al.* also showed that the presence of pre-existing vorticity could enhance the effectiveness of the generation of balanced flow by heating on scales smaller than the Rossby radius. Cotton *et al.* (1989) determined the average Rossby radius for MCCs in the central US is 300 km. There have been MCVs observed that are of this scale, but many are 1/2-1/3 the size of the Rossby radius. MCVs have also been observed with or without the presence of pre-existing vorticity. Thus it appears that the process of geostrophic adjustment may have varying degrees of importance in the initiation of MCV circulations. The balanced dynamics of MCVs have also been explored from a potential vorticity perspective.

A modeling study by Hertenstein and Schubert (1991) examined the effects of diabatic heating in a squall line on the potential vorticity and associated wind and mass fields within the system. Using apparent heat sources diagnosed from an actual squall line as input to their two dimensional semigeostrophic model, the authors found that a strong positive potential vorticity anomaly developed at mid-tropospheric levels within the stratiform region of the simulated MCS. Weaker negative anomalies developed above and below the mid-tropospheric maximum. The balanced flow field associated with the mid-level potential vorticity anomaly was strongly cyclonic. Lower pressure was also diagnosed in the positive anomaly. The presence of a strong positive potential vorticity anomaly at mid-levels was attributed to the bipolar nature of stratiform heating rates. The total derivative of potential vorticity depends on the vertical derivative of the apparent heat source. Therefore, the strong vertical gradients between the region of latent cooling below the melting level and latent heating above the melting level are responsible for generating a positive potential vorticity anomaly over time. This agrees well with observations that show MCVs have their strongest circulations in vicinity of the melting level, where vertical gradients in diabatic heating are the largest. One of the limitations of this modeling study was the fact that it was only two-dimensional. In fact, many modeling studies that have provided valuable information on line-oriented convective systems have been two-dimensional or three-dimensional with periodic constraints in the along line direction. Since observations indicate the processes involved in MCV generation are inherently three-dimensional, it would seem most appropriate to more fully represent these effects in a model.

The efforts of Skamarock *et al.* (1994) have addressed this issue. They employed a fully 3-D, nonhydrostatic adaptive-grid model that resolves both convective and system scales, without the constraint of along-line periodicity. Additionally, a full representation of Coriolis effects were included in the model. The simulated convective system initially (up to 4 hours of model time) took on the appearance of a symmetric MCS. Evidence of both cyclonic and anticyclonic rotation on the northern and southern ends of the system respectively were evident at this time (Fig. 1.5). The presence of counter-rotating "bookend" vortices was largely attributed to the tilting of ambient and system-generated horizontal vorticity into the vertical by differential downward vertical motion. After 6 hours of simulation, the cyclonic rotation on the northern end of the system had intensified and the southern anticyclonic circulation had diminished. The precipitation field had taken on a highly asymmetric pattern due to the strong cyclonic circulation in the northern portion of the system (Fig. 1.6). A mid-level mesolow was diagnosed in the center of the mature MCV and was attributed to the positive buoyancy anomaly above and the negative buoyancy anomaly below the melting level. The evolution of the system from a symmetric orientation to an asymmetric orientation was attributed to the inclusion of Coriolis effects in the model. Over time, the Earth's rotation deflects the positive buoyancy anomaly associated with the mesoscale updraft and front to rear system relative flow northward. This enhances the cyclonic circulation in the northern portion of the system through a hydrostatic lowering of mid-level pressure, enhanced convergence, and a quasi-balanced response by the wind field. At the same time the low-level cold pool associated with the rear to front flow is deflected to the south. The strong buoyancy gradients at the leading

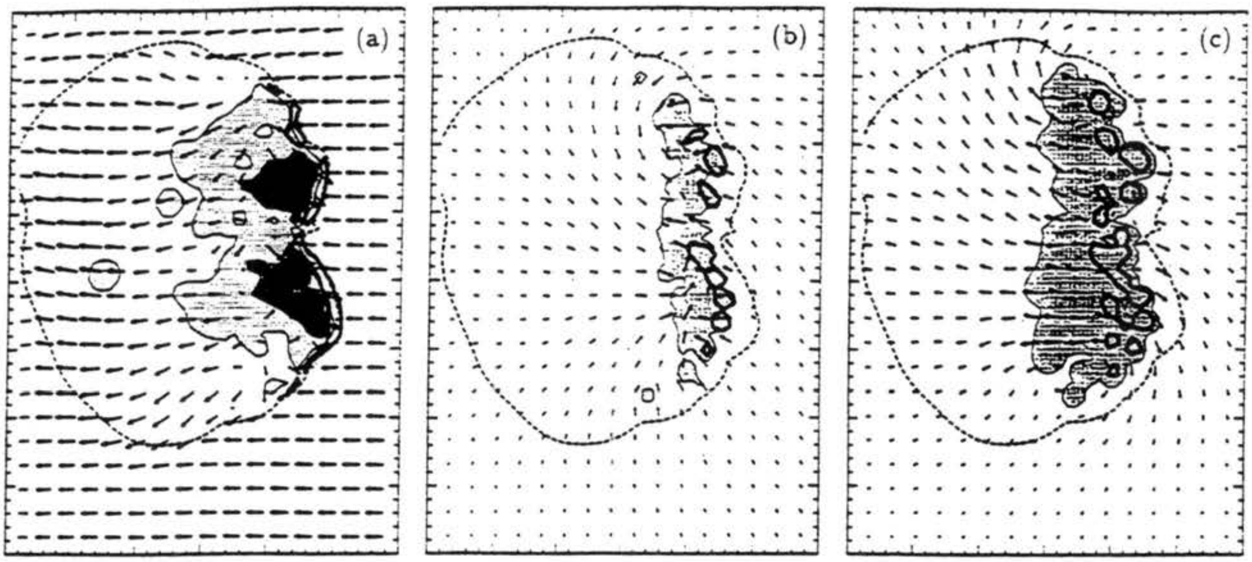

Figure 1.5: Horizontal cross sections at (a) 350 m, (b) 3000 m, (c) 8000 m for the Coriolis simulation at 4 hr. The flow vectors are storm relative. The dashed line denotes the outflow boundary. In (a) potential temperature perturbations of -4 and -6 °C are stippled light and dark respectively, in (b) stippling indicates rainwater > 0.5 g kg^{-1}, and in (c) stippling indicates cloudwater > 0.1 g kg^{-1}.(from Skamarock *et al.* 1994).

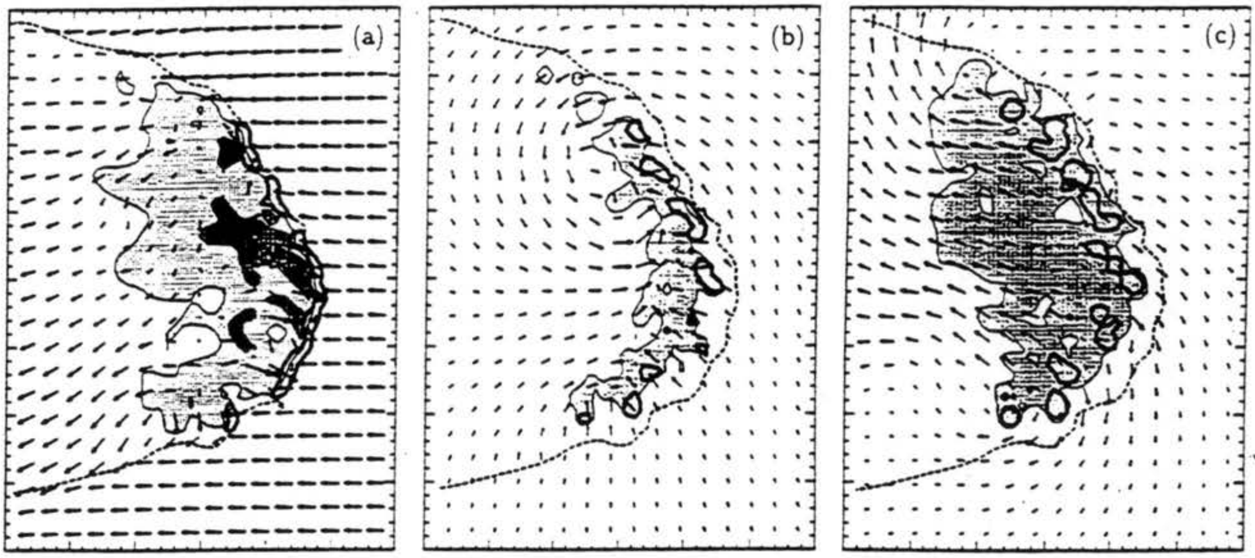

Figure 1.6: As in Figure 1.5, except at 6 hours into simulation (from Skamarock *et al.* 1994).

edge of the cold pool enhance the convection in the southern portion of the MCS. The anticyclonic circulation diminishes as the mid-level pressures on the southern side of the system increase due to the northward displacement of the positive buoyancy anomaly. This study reproduced many of the observed features of MCSs and MCVs. An important aspect of these simulated features were that they developed in the absence of large-scale forcing. Thus it appears that large-scale features (such as fronts and troughs) may not be a prerequisite for the development of asymmetric MCSs and MCVs.

The motivation for the study of MCVs is driven by their longevity and their ability to regenerate convection after the parent MCS has dissipated. In a climatology of MCVs, Bartels and Maddox (1991) found that convection reforms in vicinity of MCVs approximately 50% of the time. Furthermore, this convection is more likely to become organized into a new MCS than it is to remain disorganized. It has been estimated that MCSs contribute 30-70% of the warm season rainfall over the central US. (Fritsch et al. 1986). Also, MCSs have been known to produce flash floods (Zhang and Fritsch 1987), frequent lightning (Rutledge and MacGorman 1988, Rutledge et al. 1990), large hail, as well as occasional tornadoes. Thus, if MCVs are a frequent precursor to MCS regeneration, then a better understanding of how MCVs form and how they focus convective activity would have a large impact on the short-term forecasting of heavy rainfall and severe weather over the central US. In addition, the potential vorticity anomalies left behind by these systems could contaminate extended range forecasts.

This thesis focuses on one particular MCS that was observed in detail by dual-Doppler radar and a surface mesonet, as well as conventional sounding and satellite data on 28 May, 1985 during the PRE-STORM experiment. It is the purpose of this study to further document the evolution of an MCV and how it relates to the evolution of the parent MCS from a symmetric to an asymmetric organizational structure. It is hoped that the comparisons with previous modeling studies will aid and re-focus future efforts in the modeling community on this topic.

Chapter 2

DATA AND ANALYSIS PROCEDURES

2.1 Overview of the PRE-STORM Experiment

A major field experiment was conducted to investigate the mesoscale structure, dynamics, and microphysics of MCSs during May and June 1985 in Oklahoma and Kansas. The experiment, known as the Oklahoma-Kansas Preliminary Regional Experiment for STORM-Central (or simply PRE-STORM), was a cooperative research effort between the National Center for Atmospheric Research (NCAR), the National Oceanic and Atmospheric Administration (NOAA) and several universities. PRE-STORM was designed with the goal of improving the physical understanding of MCSs, including more reliable short-term forecasting of the duration, intensity and movement of heavy rainfall, and the potential for severe weather. PRE-STORM, as the name implies, was a preliminary experiment designed to address some of the potential problems with the proposed STORM-Central project. This experiment tested several new remote sensing systems, such as wind profilers and airborne Doppler radar. It needed to be determined how to best operate these systems in coordination with the rest of the integrated observation network in order to achieve the most reliable and useful observations of MCSs. PRE-STORM was also supposed to provide more detailed observations to focus the scientific objectives of the STORM-Central project.

Three subprograms were incorporated into the observational program of PRE-STORM. The first subprogram was the surface observational program, which included an upper-air network, NWS surveillance radars, Doppler radars, wind profilers, a surface mesoscale network, and a lightning location network. The layout for the surface observational program is shown in Fig. 2.1.

The upper-air network consisted of National Weather Service (NWS) and military-operated sites. Fourteen NWS sites in the region took soundings in addition to the standard 0000 UTC and 1200 UTC observations on operational days. The supplemental soundings were taken every three hours, with the exception of Oklahoma City, Amarillo and Dodge City, which had the ability to launch a rawinsonde every 90 minutes. The twelve military sites took upper-air observations at three hour or 90 minute intervals as well.

The surveillance radar network consisted of six NWS-operated sites using the conventional WSR-57 radars. The radars were located at Oklahoma City, OK, Amarillo, TX, Monett, MO, Wichita and Garden City, KS, and Limon, CO. These sites operated in conjunction with the PRE-STORM project, producing digitized radar volumes at 2° radial and 1nm gate spacing, with elevation spacing at 2° up to a maximum of 22°. The scanning strategy of the radars at maximum speed resulted in a minimum volume time of 10 minutes.

Two Doppler radar pairs were also incorporated into the surface observation system. A pair of the National Severe Storms Laboratory (NSSL) 10-cm Doppler radars were located at Norman and Cimaron, OK and a pair of the NCAR 5-cm Doppler radars were located at Cheney Reservoir and Nickerson, KS. The radar pairs usually operated independently, yet could be coordinated if an MCS was located over both pairs.

Three 50 MHz wind-profilers operated in the PRE-STORM experiment. They were located in Liberal and McPherson, KS and Norman, OK. The two systems in KS were three beam systems and the one in Norman was a two beam system. An acoustic sounder was also located at the McPherson site to sample wind data in the lowest 1 km of the atmosphere.

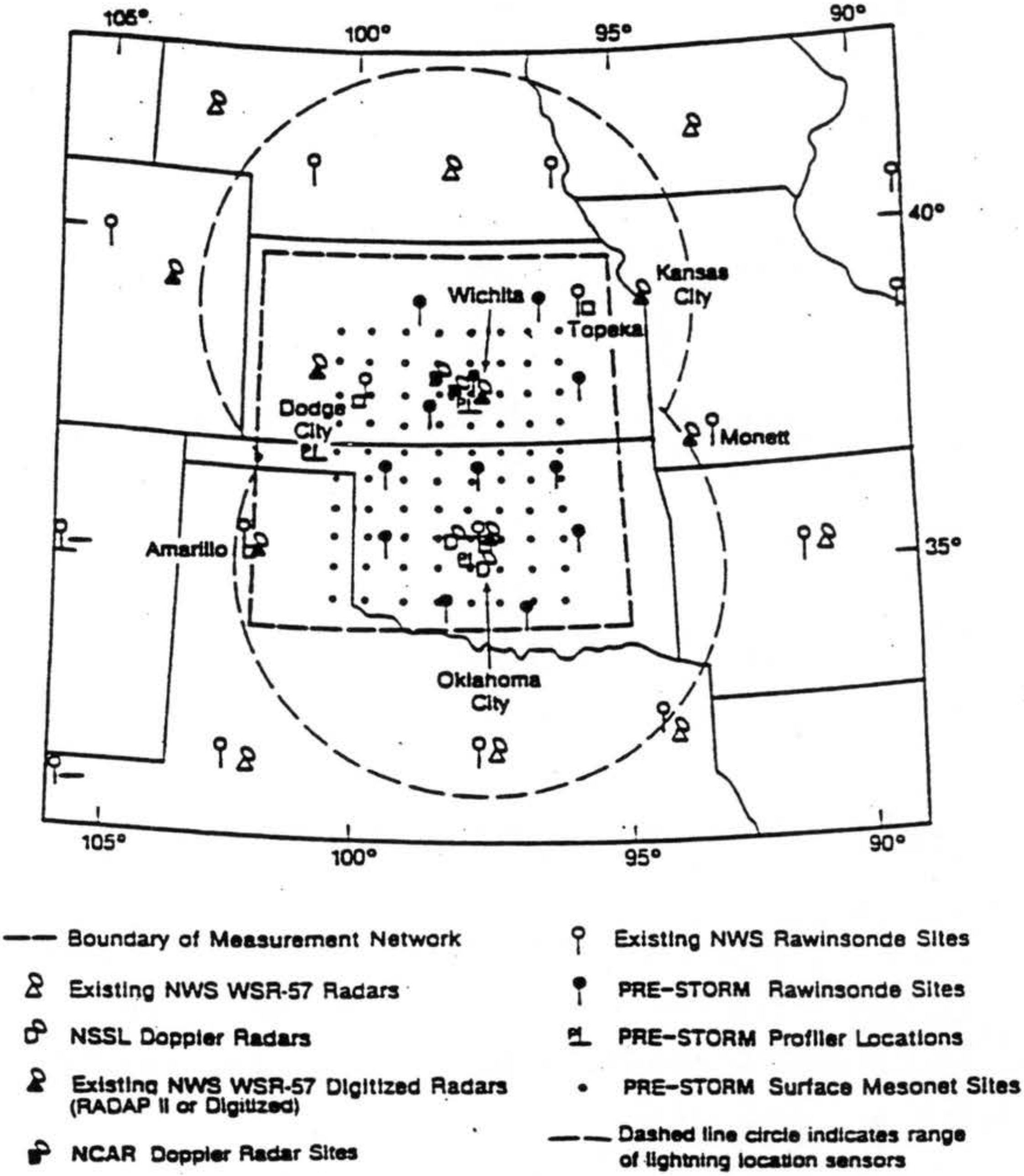

Figure 2.1: The PRE-STORM observational mesonetwork (from Meitin and Cunning, 1985).

Eighty-four surface stations, with an average station spacing of 50 km, comprised the surface mesoscale network. Half the sites, provided by NCAR, were PAM-II (Portable Automated Mesonetwork) stations. The other half, provided by NSSL, were SAM (Stationary Automated Mesonetwork) stations. Most of the PAM sites were in KS, while the SAM sites were in OK. Two PAM systems were collocated with two SAM sites to facilitate intercomparison of the data provided by both types of systems.

A lightning location network made up the final component of the surface observation network. The NSSL cloud to ground lightning location system (MacGorman *et al.* 1985) was expanded to include Kansas and Nebraska for the PRE-STORM project.

An aircraft program made up the second subprogram in the PRE-STORM observational effort. A NOAA P-3 aircraft and the University of Wyoming King Air aircraft were used during May and two P-3's were used during June. The P-3 flights used *in situ* measurements, radiometers, and Doppler radar to document the internal structure of MCSs. The King Air focused more on the development of the nocturnal low-level jet and the microphysics associated with the MCSs.

The satellite program was the final component in the PRE-STORM experiment. Visible, IR, VAS (VISSR (visible infrared spin scan radiometer) Atmospheric Sounder, and RISOP (Rapid Interval Scanning Operations) data were available for real-time forecasting during PRE-STORM operations and for subsequent research on MCSs. For more details on the PRE-STORM experiment and the available datasets, see Cunning (1986) and Meitin and Cunning (1985).

2.2 Upper-air data and analysis

Supplemental soundings from the 14 NWS and 12 Military sites were not taken for this particular case. Therefore analyses were only performed on the conventional upper-air data network of the NWS at the standard times of 0000 UTC and 1200 UTC. The raw temperature, dewpoint temperature, geopotential height, windspeed and wind direction data were objectively interpolated on constant pressure levels using NASA's GEMPAK software. A Barnes scheme (Barnes 1964) was used to interpolate the raw data to a grid centered over the continental US, with 33 grid points in the x-direction and 19 grid points in the y-direction. The grid points were separated by 2.16° of latitude in each direction. This grid spacing was selected by the GEMPAK software as being optimum for the average spacing of the input dataset.

2.3 Mesonet data and analysis

The data from 84 surface mesonet sites were used to construct surface analyses using GEMPAK. Each PAM/SAM station recorded dry and wet bulb temperatures, wind direction, speed, and gusts, station pressure, and accumulated rainfall as five minute averages. As in the upper-air analyses, a Barnes objective analysis (Barnes, 1964) was performed to interpolate the data to a 21 (x-direction) by 25 (y-direction) point grid with 0.25° of latitude grid spacing.

The raw station pressures needed special attention before interpolation in order to retrieve meaningful results from the objective analyses. The adjustments were patterned after Loehrer (1992). Since the elevations of the PRE-STORM mesonetwork stations were not uniform, the station pressures were correspondingly biased. In order to reduce these effects, the station pressures were hydrostatically adjusted to the mean elevation of the mesonetwork stations (480 m). Assuming that the surface virtual temperature was approximately equal to column average of the virtual temperature from the station elevation to 480 m, the following equation can be applied to adjust the station pressures to 480 m:

$$P_{480} = P_s \exp\left(\frac{g(z_s - 480)}{R_d \overline{T}_v}\right) \tag{2.1}$$

(2.1),

where P_{480} is the pressure at 480 m (mb), P_s is the surface station pressure (mb), g is the gravitational acceleration (9.8 ms^{-2}), z_s is the station elevation (m), R_d is the dry air gas constant (287 J kg^{-1} K^{-1}), and $\overline{T}_v$ is the mean virtual temperature of the column from the station elevation to 480 m. Effects of the diurnal tide were also removed from the pressure data using the adjustments described in Stumpf (1988). The station bias pressure corrections for this case were taken from Loehrer (1992) and are listed in Table 2.1. Individual station bias was accounted for by using pressure data from the well calibrated NWS sites surrounding the PRE-STORM network. Pressure data from the NWS sites were first hydrostatically adjusted to 480 m and then objectively interpolated using a Barnes analysis. The interpolated NWS pressures were then compared to the individual mesonet pressures during periods of undisturbed weather conditions within one or two days of the particular case of interest and the differences recorded. The differences were then averaged over a three hour period to come up with the final correction.

2.4 Doppler radar data and analysis

Single and dual-Doppler analyses were performed on the radar data from the NCAR CP-3 and CP-4 5-cm wavelength Doppler radars located near Nickerson and Cheney Reservoir, KS respectively. These radars measure both the returned power from meteorological targets within the sampling volume of the radar beam and the average velocity of the targets (within the sampling volume) along the radar beam (radial velocity). The characteristics of the radars are listed in Table 2.2. The Nyquist velocities for the two radars were set to just over 15 ms^{-1}, meaning that radial velocities with an absolute value greater than this threshold would be ambiguous, or "folded". This type of folding was common, due to the intensity of the mesoscale circulations associated with this convective system. Radial velocities were first thresholded to eliminate regions of low signal to noise ratio.

Table 2.1: PAM and SAM pressure corrections for 27-29 May 1985 (from Loehrer 1992).

Station	Applied pressure correction (mb)	Station	Applied pressure correction (mb)
P01	1.56	S01	0.35
P02	1.86	S02	0.34
P03	0.00	S03	1.55
P04'	-0.57	S04'	1.28
P05	-0.32	S05	0.05
P06	-0.80	S06	0.50
P07	0.08	S07	-0.42
P08	-0.94	S08	0.03
P09	0.31	S09	-1.95
P10	-0.10	S10	1.19
P11	0.25	S11	0.11
P12	1.55	S12	1.25
P13	0.56	S13	1.10
P14	-1.53	S14	M
P15	0.46	S15	0.18
P16	0.04	S16	0.02
P17	-0.48	S17	-0.12
P18	0.18	S18	0.63
P19	0.44	S19	M
P20	-0.34	S20	0.54
P21	0.36	S21	-1.39
P22	-0.81	S22	0.56
P23	-0.01	S23	0.46
P24	-0.70	S24	M
P25	0.42	S25	0.58
P26	-0.38	S26	1.20
P27	-0.97	S27	0.23
P28	-1.61	S28	0.58
P29	1.87	S29	0.70
P30	0.70	S30	0.13
P31	1.27	S31	1.30
P32	-1.73	S32	0.20
P33	0.06	S33	-0.25
P34	0.34	S34	0.99
P35	-0.11	S35	0.54
P36	-0.08	S36	0.61
P37	0.40	S37	0.76
P38	0.03	S38	1.25
P39	1.75	S39	0.63
P40	0.02	S40	M
P41	-0.81	S41	2.06
P42	0.18	S42	-0.24

Table 2.2: Characteristics of the NCAR radars used in PRE-STORM (from Rutledge *et al.* 1988)

Parameter	Radar CP-3	Radar CP-4
Wavelength (cm)	5.45	5.49
Maximum range (m)	135	135
Nyquist velocity (ms^{-1})	15.37	15.24
Peak power (kW)	400	400
Pulse width (μ sec)	1.0	1.0
Pulse repetition frequency (Hz)	1111	1111
Minimum detectable signal (dBm)	-113	-112
Number of range gates	512	512
Azimuthal direction (deg)	0.8	0.8
Gate spacing (m)	260/150*	260/150*
Number of samples	64/256**	64/256**

* A gate spacing of 150 m was used for the EVAD and vertically pointing scans.

** Number of samples was set at 256 for the vertically pointing mode.

Ambiguous velocities were "unfolded" by adding (or subtracting) the correct number of Nyquist intervals to the folded velocities. The process of diagnosing and unfolding the ambiguous velocities was subjective. The radial velocities were unfolded and returned power (dBm) was converted to reflectivity (dBZ) using the NCAR software package RDSS (Research Data Support System, Oye and Carbone 1981). The processed radar files were then objectively interpolated to Cartesian grids, with a 1.5 km horizontal and 0.5 km vertical grid spacing using the NCAR REORDER package. A Cressman (1959) weighting scheme was used in the interpolation process, with a horizontal radius of influence of 2 km and a vertical radius of influence of 0.75 km. The grids were rotated such that the x-axis was oriented parallel to the direction of storm motion (toward 120°), thus storm velocity (16 ms^{-1}) could be removed from the radial velocity data in a vertical cross-section through the radar location. The objective interpolation to Cartesian grids served two purposes: 1) to facilitate plotting of reflectivity and velocity in horizontal and vertical cross-sections, and 2) to provide input for the dual-Doppler analysis.

When two Doppler radars are close enough to view the same storm in detail, the two radial velocity fields can be used to reconstruct the 3-D wind field within the storm. The first step is to edit the velocity fields from the two radars and interpolate them to the same Cartesian coordinates as described above. The coordinate system must be chosen carefully to ensure the grid location includes areas where the beam crossing angle is large (usually >30°, in order to minimize errors in diagnosed horizontal wind fields), and that the grid spacing is appropriate for the horizontal scale resolved by the two radars. The radar spacing, minimum beam crossing angle allowed, and the beam width of the radars determines resolution of the dual-Doppler analysis. For a beam crossing angle >30°, a radar separation of 62 km, and an azimuthal beam width of 0.8°, the horizontal grid spacing was determined to be 1.5 km for the CP-3 and CP-4 dual-Doppler grid. The dual-Doppler calculations were performed using the Cartesian Editing and Display of Radar data under Interactive Control (CEDRIC) software developed at NCAR by Mohr and

Miller (1983). Once the two radial velocity fields were interpolated to the proper grid, the horizontal wind field could be derived from the two radial velocity components at each grid point where the beam crossing angle exceeded 30°. Precipitation particle fall speeds, which contaminate the estimates of horizontal velocities, were removed using the reflectivity field to estimate the mean radius of the particles at each grid point, which can then be used to deduce the average fallspeed of the particles at that point. One relationship was used for levels above the melting level (ice particles) and one for below the melting level (rain). A divergence field was calculated for the corrected horizontal wind field using centered finite differencing techniques. The divergence field was then integrated downward using the anelastic continuity equation to obtain the vertical velocity with a boundary condition of zero velocity at the radar estimated cloud top. This typically results in a non-zero vertical velocity at the surface, because the radars underestimate the low-level divergence field, and errors accumulate in the downward integration. As a result, an O'Brien (1970) type adjustment was made, which imposes a zero vertical velocity at the surface, and adjusts the horizontal wind field to be consistent with this velocity profile. An adjusted divergence field was calculated from the new horizontal wind field, which was then integrated to obtain a new vertical velocity field. This procedure was reiterated until a solution was converged upon. This was determined to be when the mean of the absolute value of the change in horizontal wind components at each level from one iteration to the next was less than 0.1 ms^{-1}, which generally took 3 iterations.

Chapter 3

SYNOPTIC SETTING AND MESONET ANALYSIS

3.1 Genesis environment

The large scale features associated with the initial development of the MCS are examined using the conventional NWS surface and upper air network. A surface analysis at 0300 UTC 28 May (not shown) depicted a weak low pressure center over eastern Indiana with a trailing cold front extending through the Ohio Valley to southwestern MO. The front was stationary from the KS-OK border to the Front Range of the Rocky Mountains. Along the stationary front near the KS-OK border, the low-level flow was convergent and dewpoints were in excess of 60°F. The 0000 UTC 850 mb analysis (Fig. 3.1a) showed a pocket of warm, moist (high θ_e) air being advected into the PRE-STORM region by a low situated in the central Rocky Mountains. At 700 mb (Fig. 3.1b) a weak short-wave was moving out of the Rocky Mountains into a ridge of high θ_e air. This feature appeared to be more of a weakening of the ridge than a short-wave trough at 500 mb (Fig. 3.1c). A climatology of MCVs by Bartels and Maddox (1991) states that MCVs generally form under longwave ridges at 500 mb, which is consistent with this scenario.

The closest sounding to the pre-squall environment was taken at 1200 UTC at Oklahoma City, OK (OKC) (Fig. 3.2). This sounding is typical of a severe weather sounding, with a deep low-level moist layer capped by a subsidence inversion. Surface winds in the moist layer were from the southeast and a southerly low-level jet of 20 ms^{-1}

(a) (b)

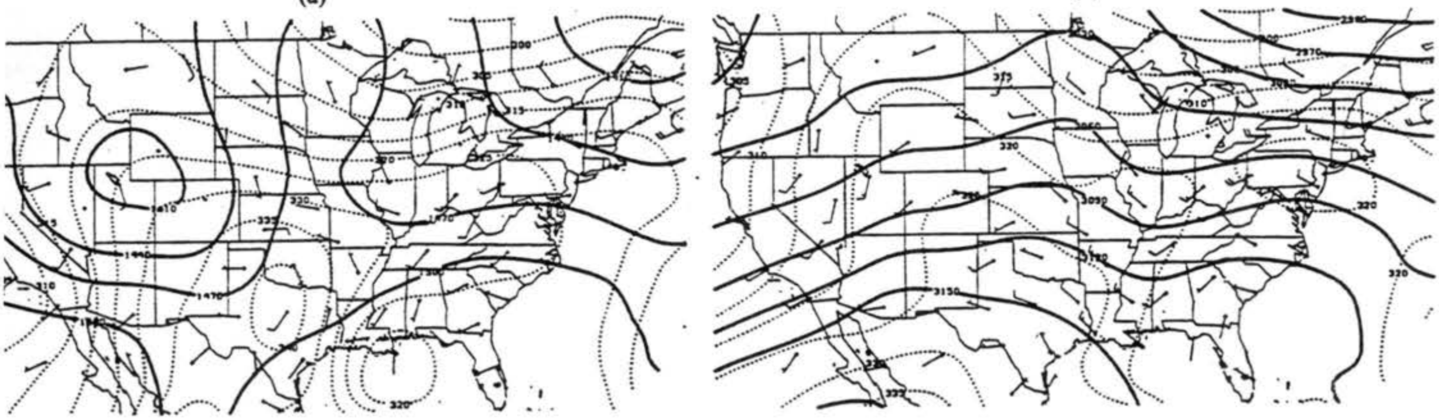

Figure 3.1. Upper air analysis at 0000 UTC, 28 May 1985. a) 850 mb level. b) 700 level.. Geopotential heights (solid) contoured every 30 m. θ_e (dotted) contoured every 5 °K. Wind barbs: full barb = 10 ms^{-1}, half barb = 5 ms^{-1}.

(c)

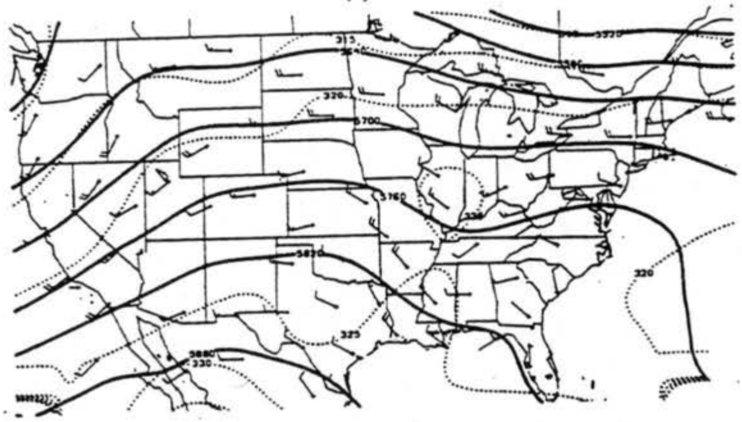

Figure 3.1: (c) Same as 3.1 (a),(b), except for 500 mb and heights contoured every 60 m.

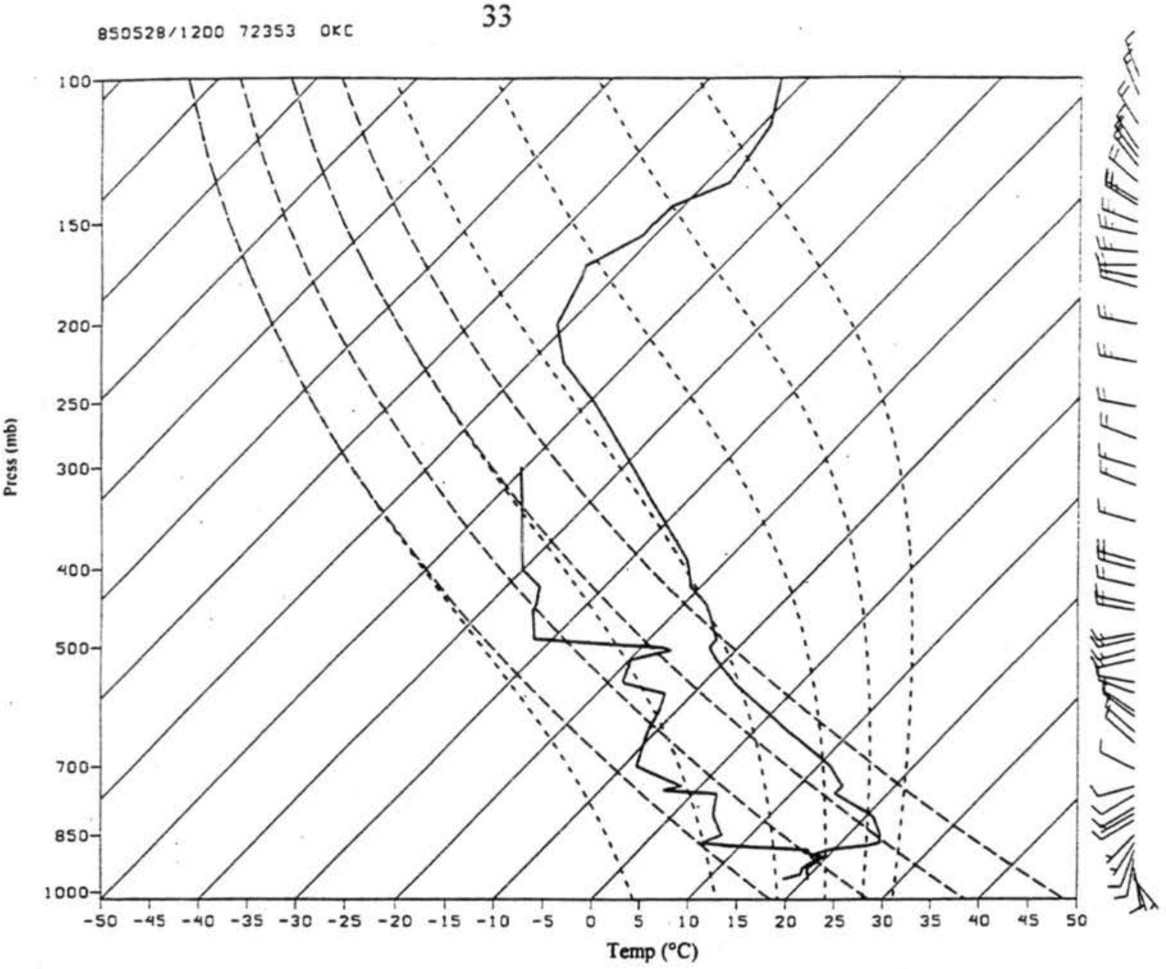

Figure 3.2: Sounding from Oklahoma City, OK (OKC) at 1200 UTC, 28 May 1985.

was situated just below the inversion, while warm, dry southwesterly flow capped the moist layer. The stability indices indicated a threat for strong convection (CAPE=1600 Jkg^{-1} ; Lifted index = -6 ; Total Totals index = 56). These indices are typical of what Bartels and Maddox (1991) found in the genesis environment of MCVs. The convective inhibition (437 Jkg^{-1}) was a little higher than found in the Bartels and Maddox climatology, but it should be noted that the MCS propagated just to the north of OKC (according to the Wichita WSR-57 radar analyses in Ch. 4), suggesting that the inversion was stronger near OKC than it was in the actual pre-squall environment. The lowest 5 km had a moderate westerly shear of 15 ms^{-1}, slightly less than the value of 20 ms^{-1} found necessary to simulate long-lived convective systems (Weisman 1993). Again, it should be pointed out that this sounding may not be completely representative of the actual pre-squall environment.

3.2 Mesonet analysis

Locations of the PRE-STORM mesonet stations used in the following analysis are shown in Fig. 3.3. Locations of the National Center for Atmospheric Research (NCAR) CP-3 and CP-4 radars, and the dual-Doppler domains used in this study, are also shown.

At 0935 UTC (Fig. 3.4a) the surface θ_e and wind fields indicated that the squall line associated with this MCS was entering the PRE-STORM mesonet. The synoptic flow was generally light southeasterly, but the northwestern PAM (Portable Automated Mesonetwork) stations were reporting northerly winds in excess of 10 ms^{-1}. In vicinity of the wind shift there was also a tight gradient in the θ_e field. This appears to be the gust front associated with the convective line; the single radar analysis in Ch. 4 will confirm that the convective system was moving through this region at this 0900 UTC. The synoptic flow was advecting high θ_e air over the gust front, fueling the convection. Convergence between the synoptically driven southeasterly flow ahead of the MCS and

Figure 3.3: Locations of the PAM/SAM mesonet stations and the NCAR CP-3 and CP-4 radars as deployed in PRE-STORM. The dual-Doppler analysis domains used in this study are also indicated.

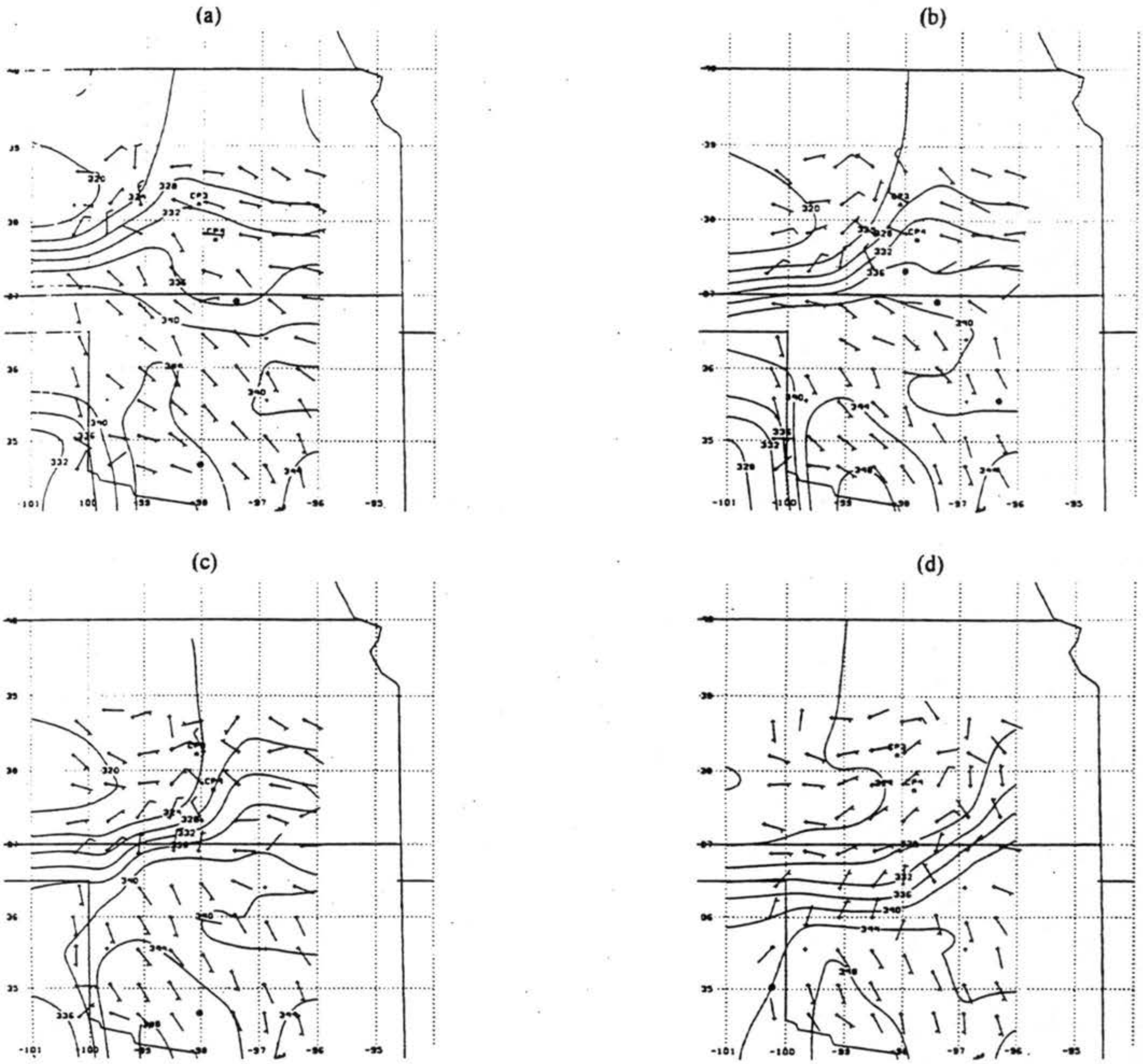

Figure 3.4: Surface mesonet analysis of θ_e (solid contours, °K), wind barbs (full = $10 ms^{-1}$; half = $5 ms^{-1}$). (a) 0935 UTC 28 May 1985; (b) 1050 UTC; (c) 1140 UTC; (d) 1315 UTC.

the convectively generated outflow acted to focus upward motion at the gust front, intensifying the convection. At 1050 UTC (Fig. 3.4b) the gust front had moved to the southeast some 65 km. In the equivalent-potentially cool air behind the gust front the winds were highly divergent, suggesting the presence of an organized downdraft. Doppler radar data presented below will confirm the presence of a mesoscale downdraft at this time. Note the gradient in θ_e was strongest on the southern end of the system. A recent modeling study by Skamarock *et al.* (1994) suggests that this feature is common in long-lived convective systems and results from the turning of the mesoscale outflow to the right of the storm motion by the Coriolis force. The enhanced gust front acts to strengthen the convection on the southern end of the MCS, which in turn strengthens the gust front, creating a positive feedback situation. The radar analyses in Ch. 4 will illustrate that the convection was indeed strongest on the southern edge of the MCS. Figs. 3.4c-d show the continued progression of the MCS to the east-southeast, with the strongest gust front surge on the southern edge of the system. By 1315 UTC (Fig. 3.4d), the mesoscale outflow was affecting the entire northern portion of the mesonet. At later times (not shown) the gust front appeared to slow in its southerly progression across the mesonet.

Surface pressure features are depicted in Fig. 3.5. At 0935 UTC (Fig. 3.5a), there was a localized high pressure area (mesohigh) entering the northwestern corner of the network behind the gust front. The mesohigh has been attributed to cooling due to rainfall evaporation (Sawyer 1946), as well as latent and sensible cooling of melting ice particles (Fujita 1959). An area of low pressure (wake low) trailed the mesohigh and a trough of low pressure (pre-squall low) preceded the gust front. The pre-squall low (Hoxit *et al.* 1976) and the wake low (Zipser 1977, Johnson and Hamilton 1988) have both been attributed to mesoscale subsidence warming generated by the convective system, although the mechanisms of such subsidence generating both the pre-squall and wake lows may be quite distinct. Pressure gradients across the southern portion of the gust front were as large as 4 mb/100 km. The mesohigh and wake low had intensified and moved to the

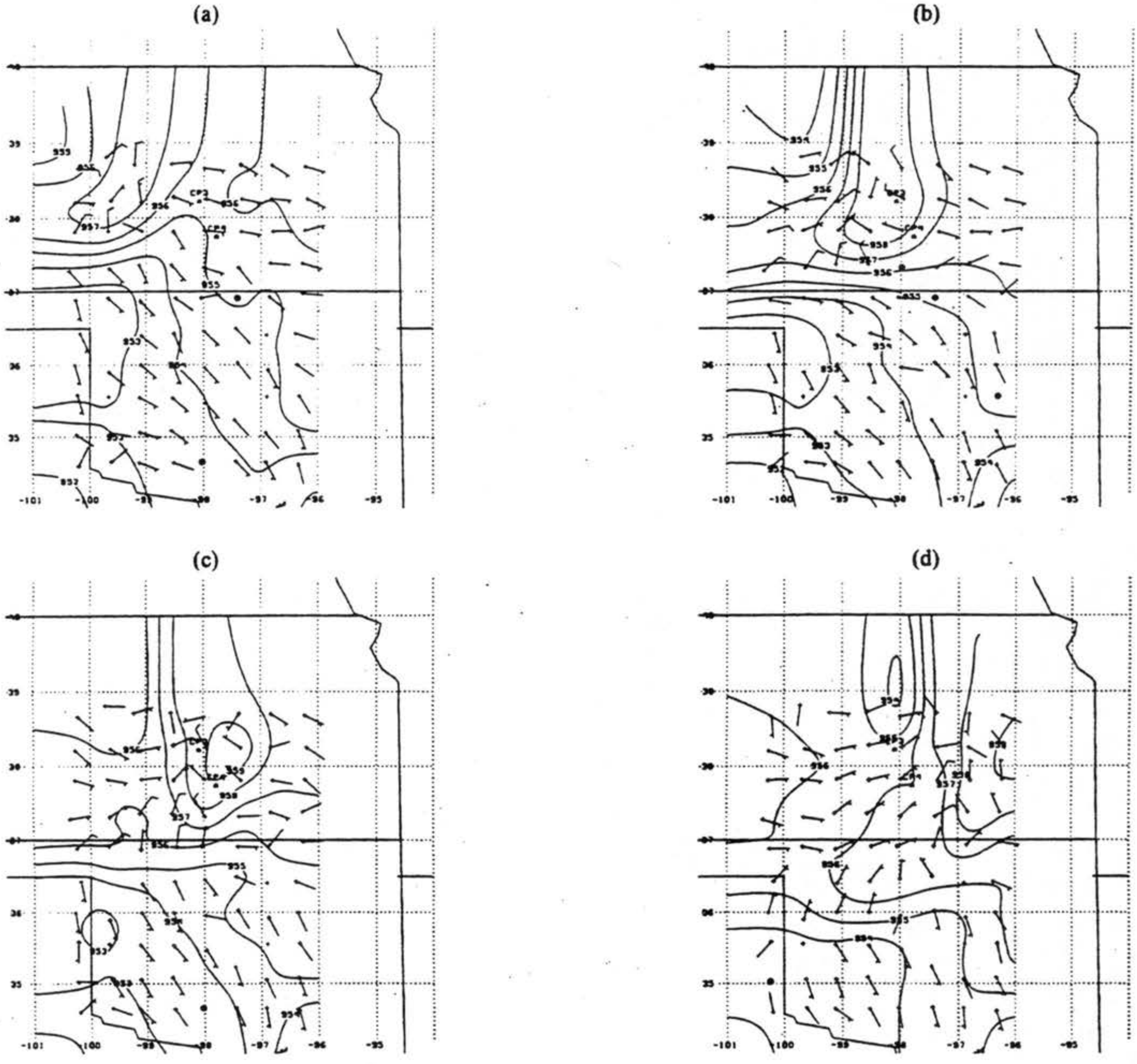

Figure 3.5: Surface mesonet analysis of station pressure (solid contours, mb), wind barbs (full = $10 ms^{-1}$; half = $5 ms^{-1}$). (a) 0935 UTC 28 May 1985; (b) 1050 UTC; (c) 1140 UTC; (d) 1315 UTC.

southeast by 1050 UTC (Fig. 3.5b), but the pre-squall trough weakened somewhat. An hour later (Fig. 3.5c) the mesohigh had continued its east-southeasterly progression, now with a central pressure of 959 mb. The wake low was not as pronounced as earlier, yet still was evident to the rear of the mesohigh. The 1315 UTC analysis (Fig. 3.5d) shows the mesohigh exiting the northeastern domain of the mesonet, while maintaining a central pressure greater than 959 mb. The wake low was now slightly deeper, with a central pressure near 954 mb. A low pressure trough ahead of the gust front was again evident in the southern domain of the mesonet. At later times (not shown) the mesohigh and wake low quickly exited the mesonet and surface pressures returned to values seen before the passage of the MCS.

Individual time series at two different PAM stations illustrate the difference in the progression of surface features on the northern and southern extremes of the MCS. The northern portion of the MCS is represented by the PAM 6 station (Fig. 3.6). The pressure trace (Fig. 3.6a) showed the passage of a broad mesohigh between 1030 and 1330 UTC. Pressures increased 2-3 mb as the MCS moved over the station. A very pronounced wake low, accompanied by high wind (Fig. 3.6b), followed the mesohigh. The pressure dropped nearly 8 mb in 10 minutes; one minute average winds were sustained at 18 ms^{-1} and gusts of 25 ms^{-1} were recorded. Surface temperatures increased and dewpoints dropped at this time as well (Fig. 3.6d), consistent with the theory that wake lows are a hydrostatic response to strong subsidence warming on the back edge of the stratiform cloud (Zipser 1977, Johnson and Hamilton 1988). The southern portion of the MCS had surface features distinct from those in the northern portion. The pressure trace at PAM 27 (Fig. 3.7a) was markedly different from the records at PAM 6. A strong pressure rise (4 mb) occurred from 10-11 UTC, but the high pressure jump was quite localized and did not last very long. At PAM 6 the pressure rise was not as strong and was much broader in a temporal sense. There was also no apparent wake low passage at PAM 27 and the high winds (Fig. 3.7b) were associated with the passage of a mesohigh, not a wake low.

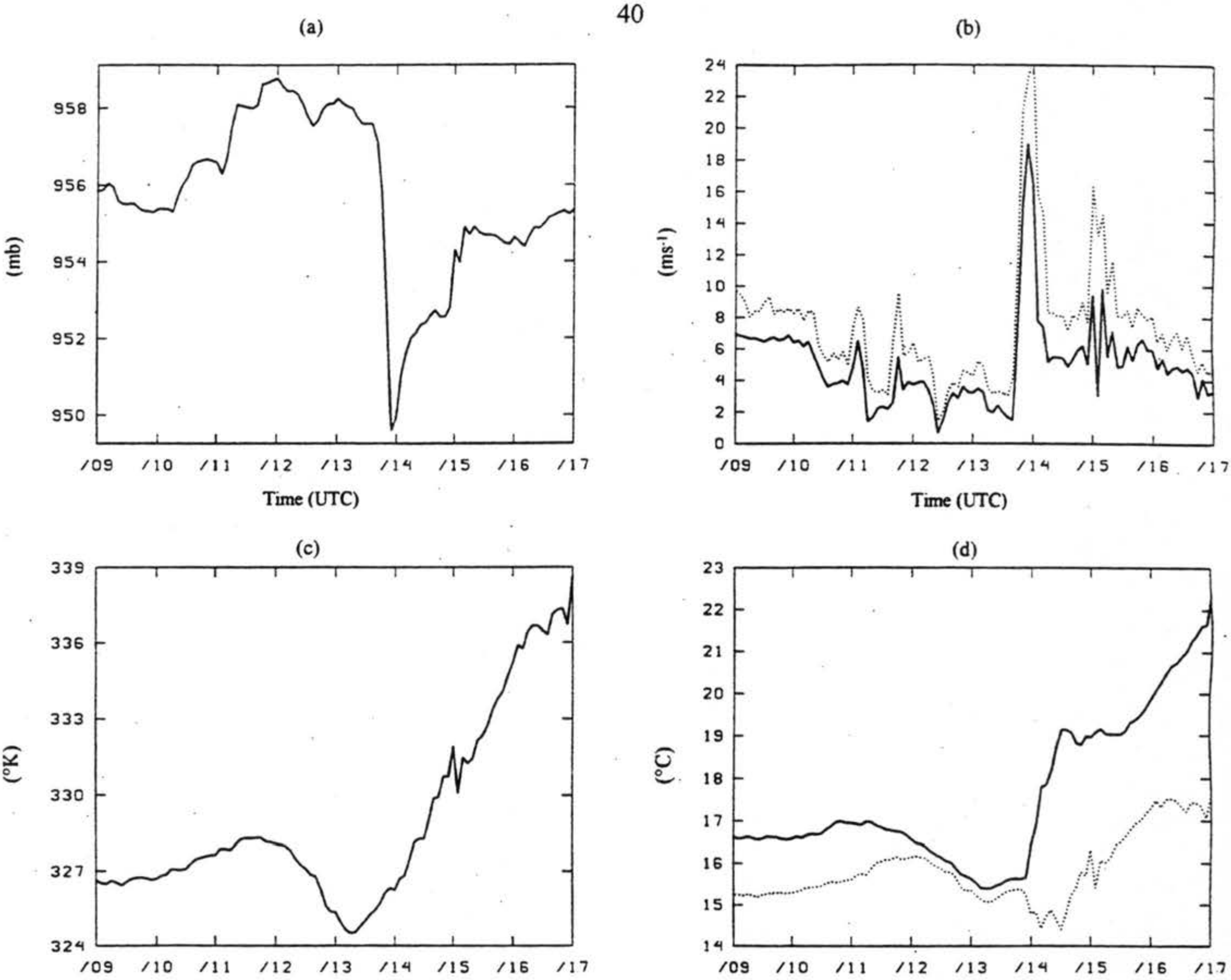

Figure 3.6: Time series of (a) station pressure (mb); (b) windspeed and gusts (ms^{-1}); (c) θ_e (°K); (d) temperature and dewpoint (°C) at PAM 6.

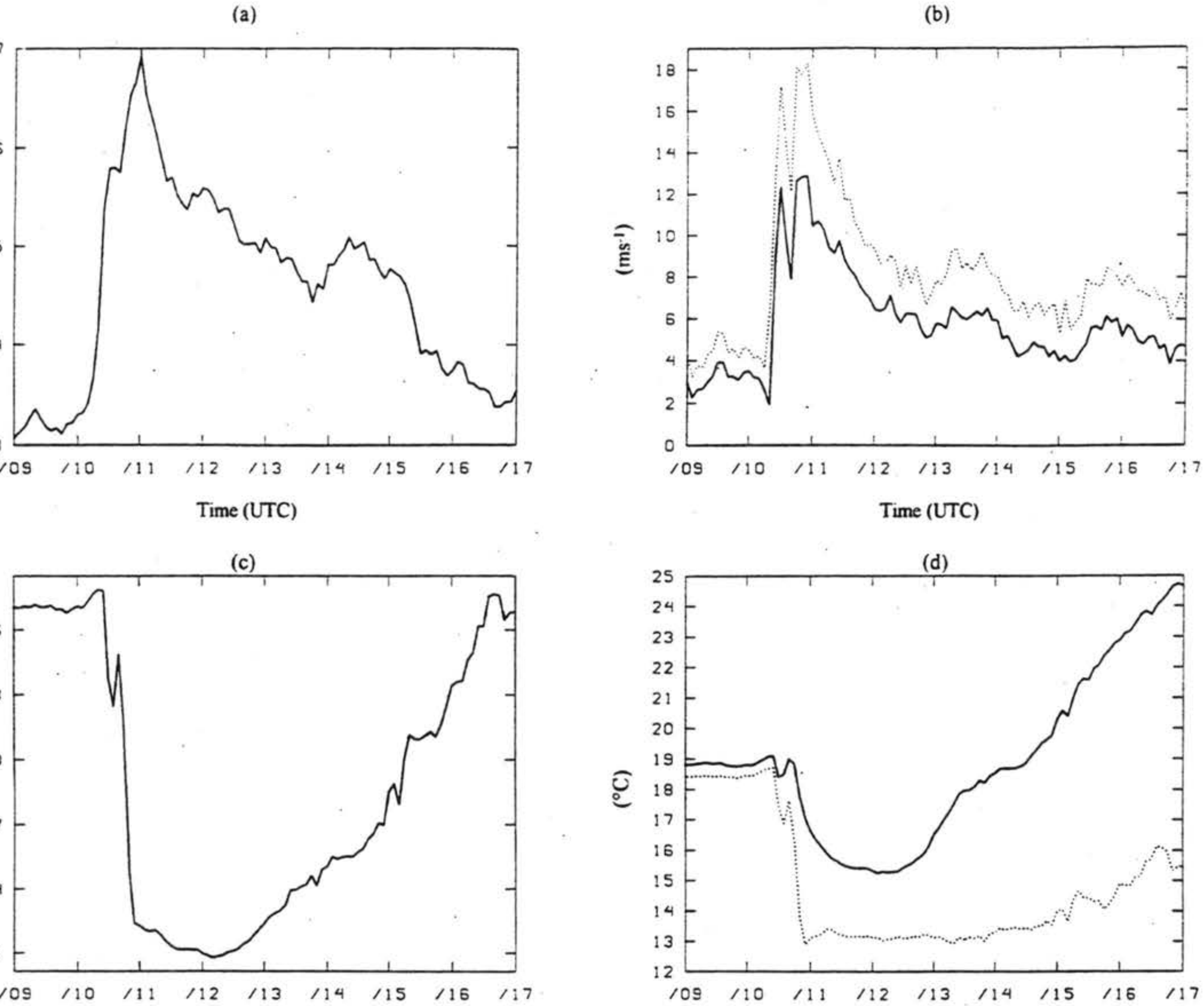

Figure 3.7: Time series of (a) station pressure (mb); (b) windspeed and gusts (ms^{-1}); (c) θ_e (°K); (d) temperature and dewpoint (°C) at PAM 27.

Furthermore, the passage of the strong mesohigh at PAM 27 was associated with a much cooler and dryer airmass than at PAM 6, as evidenced by the equivalent potential temperature (Fig. 3.7c), air temperature and dewpoint temperature traces (Fig. 3.7d). The profound differences in the surface features in the northern and southern portions of the MCS can be attributed to the asymmetry in the precipitation field. The weaker, broader mesohigh and the trailing wake low are more characteristic of stratiform precipitation (northern portion of the MCS), while the stronger, more localized mesohigh and absence of a wake low is more typical of convection (southern portion of the MCS). The radar analysis presented in the following chapter will also illustrate this asymmetry. In an analysis of a similar asymmetric MCS, Brandes (1990) also found a strong wake low in the northern portion of the system as well as a mesohigh to the south.

Skamarock *et al.* (1994) have shown how the presence of Coriolis effects in 3-D simulations of long lived squall lines can lead to this type of asymmetry. As the system matures, and Coriolis effects have had enough time to act on the flow (~6 hrs), the ascending mesoscale front to rear (FTR) flow is deflected to the right (north), which preferentially advects hydrometeors from the convective line into the northern portion of the system. This develops a broad stratiform precipitating region to the north. At the same time, the descending mesoscale rear to front (RTF) flow is deflected to the right (south). This descending RTF flow contains air that has been diabatically cooled through the processes of melting and evaporation of precipitation. This RTF flow contributes to the outflow or cold pool at the surface. As the cold pool is deflected to the south by the Earth's rotation, buoyancy gradients at the leading edge of the cold pool enhance convection in the southern portion of the MCS (Rotunno *et al.* 1988, Weisman 1992). The enhanced convection strengthens the cold pool, which provides positive feedback to the convection. The surface features presented above strongly support these hypotheses. For example, the cold pool in the southern portion of the MCS (Fig. 3.7c) had much stronger gradients and higher amplitude compared to the northern portion of the MCS

(Fig. 3.6c). This deflection of the cold pool to the south created stronger convection to the south and resulted in weaker convection with a broad stratiform region to the north, as will become apparent in the following radar analysis discussion. The intense wake low on the back edge of the northern stratiform cloud and absence of a wake low to the south is also a result of the asymmetry of the precipitation field.

Chapter 4

SATELLITE AND RADAR ANALYSIS

4.1 IR satellite images

The enhanced IR satellite imagery at 0700 UTC (Fig. 4.1a) shows the convective system was moving into northwestern KS. The cold cloud shield was already quite extensive, with the area of cloud top temperatures exceeding the requirements for an MCC as defined by Maddox (Table 1.1). The coldest temperatures (< -64 °C) were in the southern portion of the system, coincident with the region of strongest convection. By 1100 UTC (Fig. 4.1b) the MCS had moved into central KS, when the cold cloud shield became more symmetric. The area of coldest temperatures was now at its maximum extent, coincident with the most intense convective stage of the MCS. It is interesting to note the concavity or notching in the western extreme of the cirrus cloud shield. The following radar analyses will show that a strong and deep rear inflow jet was present in the western extreme of the MCS at this time. The warming of the cloud top temperatures in this region may be associated with strong subsidence in the rear inflow jet (i.e. the thinning of the cloud shield allowed IR upwelling from lower levels). At 1300 UTC (Fig. 4.1c) the MCS was on the decline. The area of < -64 °C cloud top temperatures was much smaller than at 1100 UTC. The notch of warmer IR temperatures on the western extreme of the MCS described in the previous image was still apparent at this time. The radar analyses will show the rear inflow jet was still present at this time. By 1600 UTC (Fig. 4.1d) the cirrus shield was nearly circular and the presence of temperatures < -64 °C was minimal.

(a)

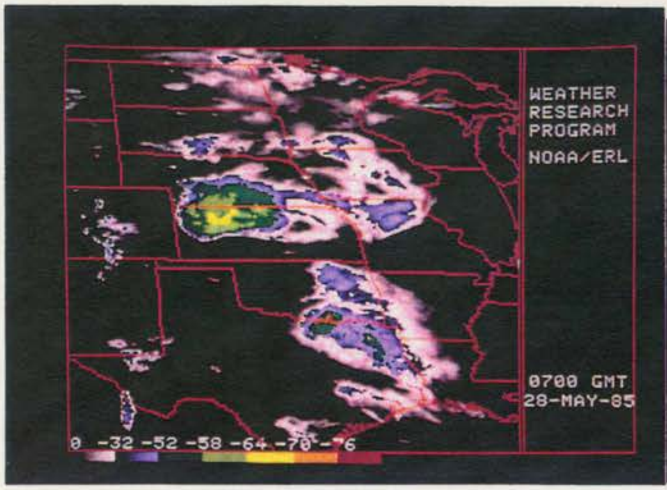

(b)

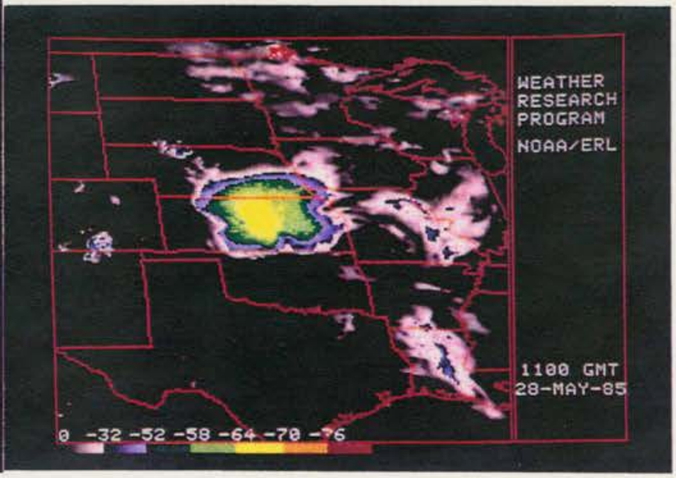

(c)

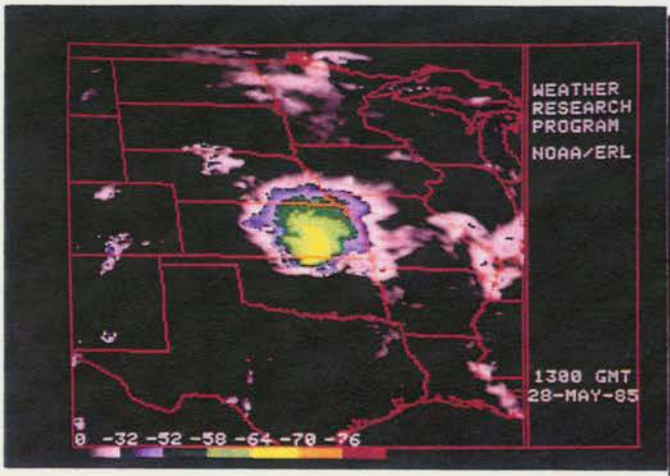

(d)

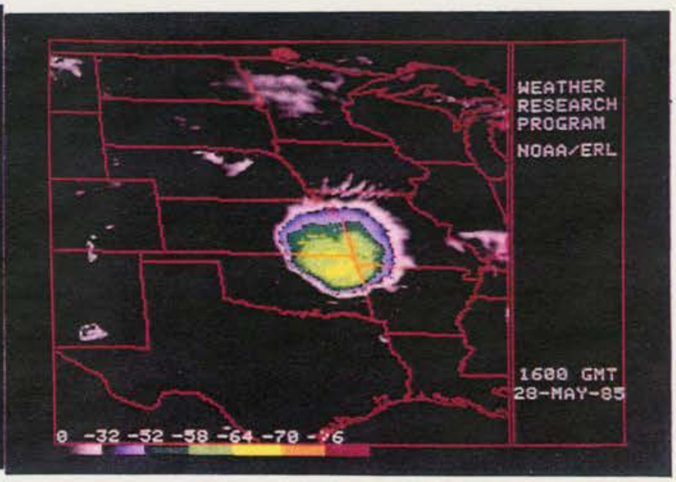

Figure 4.1: Infrared satellite images indicating cloud top temperatures (°C) for 28 May 1985 at (a) 0700 UTC, (b) 1100 UTC, (c) 1300 UTC, (d) 1600 UTC.

The radar data presented below will show that beneath this highly symmetric cloud top, the MCS had developed an asymmetric precipitation structure over time.

4.2 WSR-57 data

Digitized data from the National Weather Service WSR-57 radar in Wichita, KS captured a large perspective view of the low-level reflectivity patterns associated with this MCS. At 0900 UTC (Fig. 4.2a) the MCS was in northwestern KS and appeared to have a largely symmetric structure. Two hours later (Fig. 4.2b), the squall line was in central KS and had begun to show signs of asymmetry. The northern portion of the system had developed a trailing stratiform region, while the southern portion was largely composed of convection. The MCS had clearly become asymmetric by 1200 UTC (Fig. 4.3a). The northern stratiform region had broadened and notching on the back edge of the stratiform echo suggests a strong rear inflow jet had developed. This notching developed into a well defined hook-like echo by 1335 UTC (Fig. 4.3b). As will be shown in the dual-Doppler analysis, this feature is not only indicative of a strong rear inflow jet advecting dryer air into the MCS, but is also indicative of a strong low- and mid-level cyclonic circulation advecting hydrometeors from the stratiform region to the north of the dry air intrusion.

4.3 CP-3 data

The NCAR CP-3 C-band radar (which was situated roughly 100 km NW of Wichita) afforded a slightly smaller, yet more detailed view of the MCS. Horizontal cross-sections of reflectivity at 3.5 km (AGL) are depicted in Figs. 4.4 and 4.5. This time series is illustrative of the development of the rear inflow notch and the associated intensification of the cyclonic mesovortex circulation. At 1120 UTC (Fig. 4.4a) the notching of the reflectivity field was becoming apparent about 100 km due west of the radar. At 1148

(a)

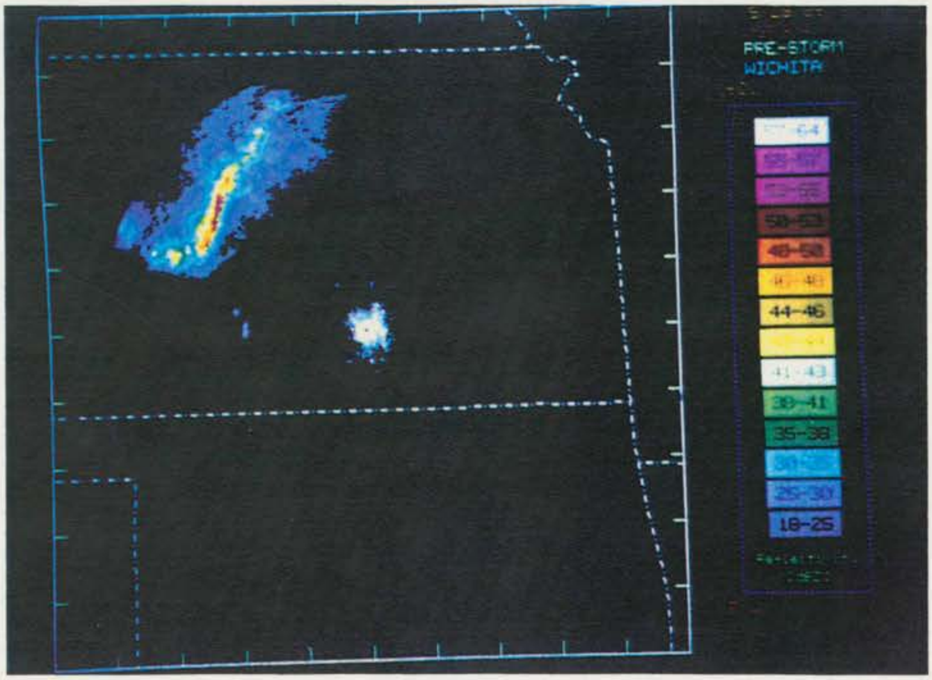

(b)

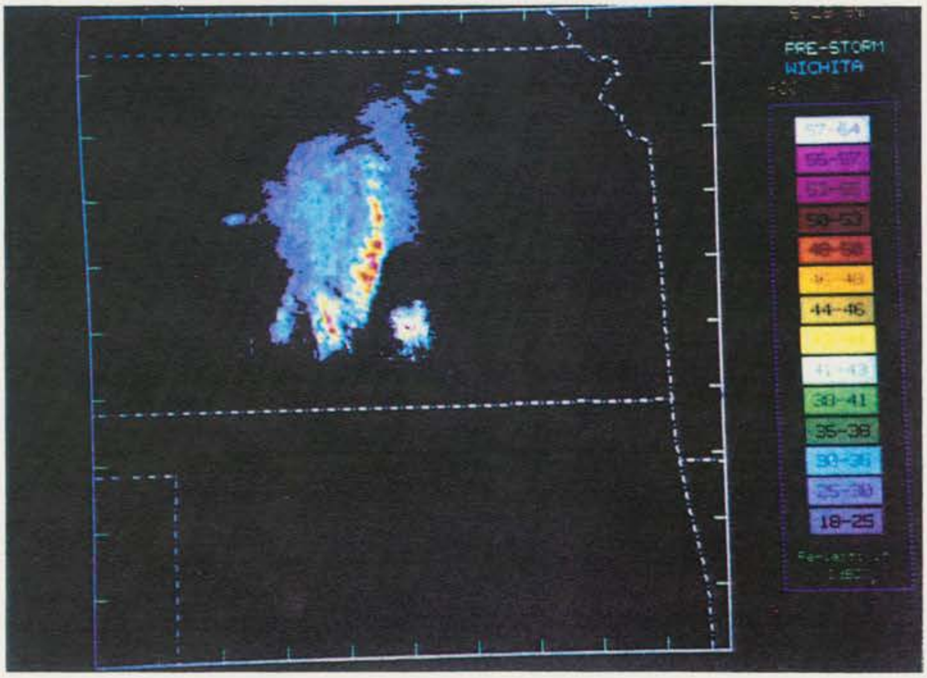

Figure 4.2: Low level (0.7° PPI) reflectivity from the National Weather Service WSR 57 radar located in Wichita, KS for 28 May 1985 at (a) 0859 UTC; (b) 1106 UTC.

(a)

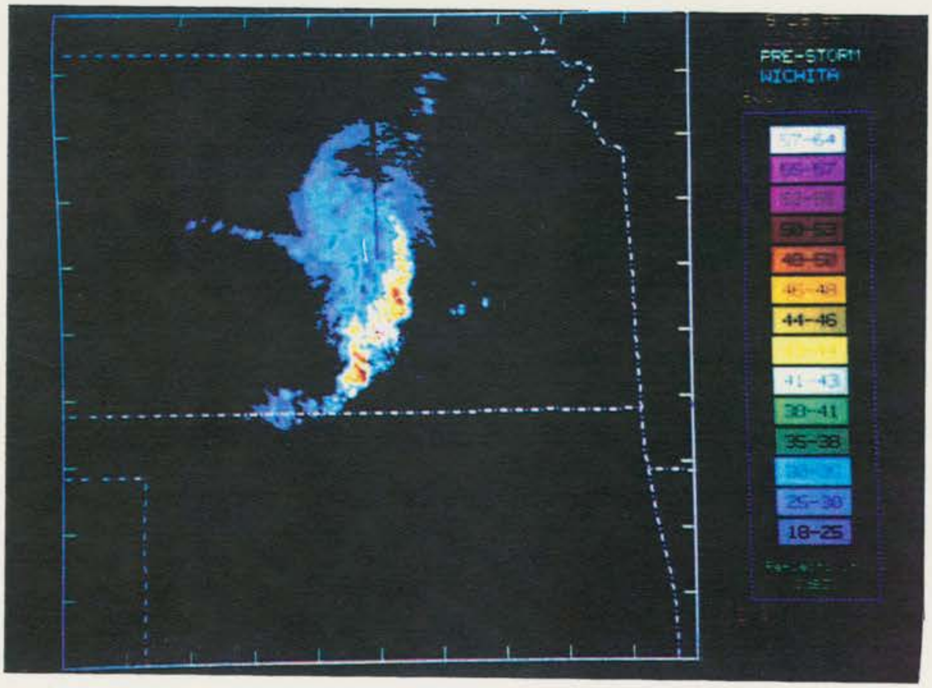

(b)

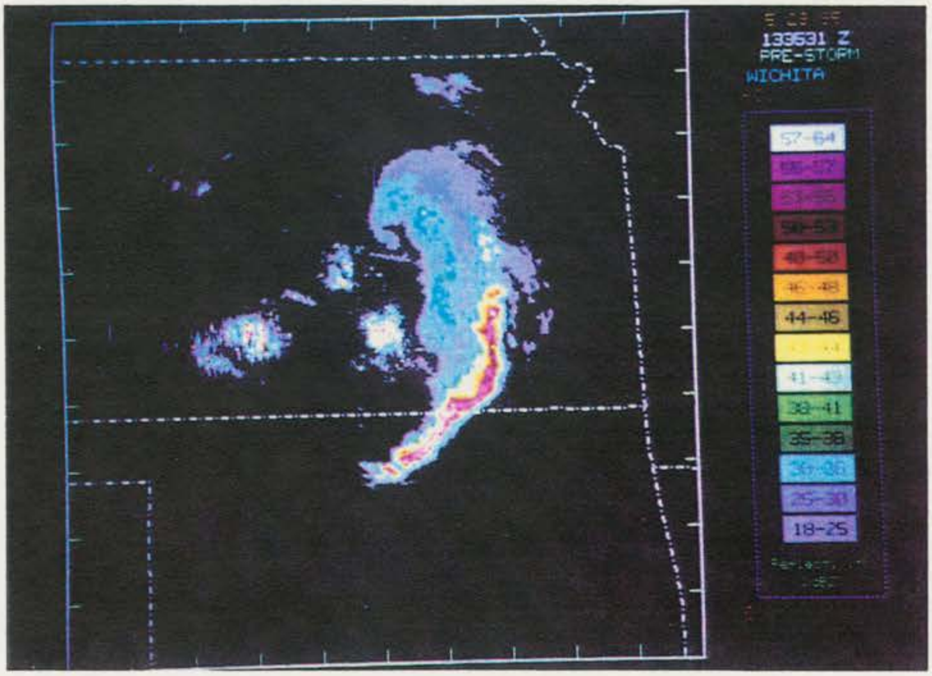

Figure 4.3: Same as figure 4.2, except at (a) 1202 UTC, and (b) 1335 UTC.

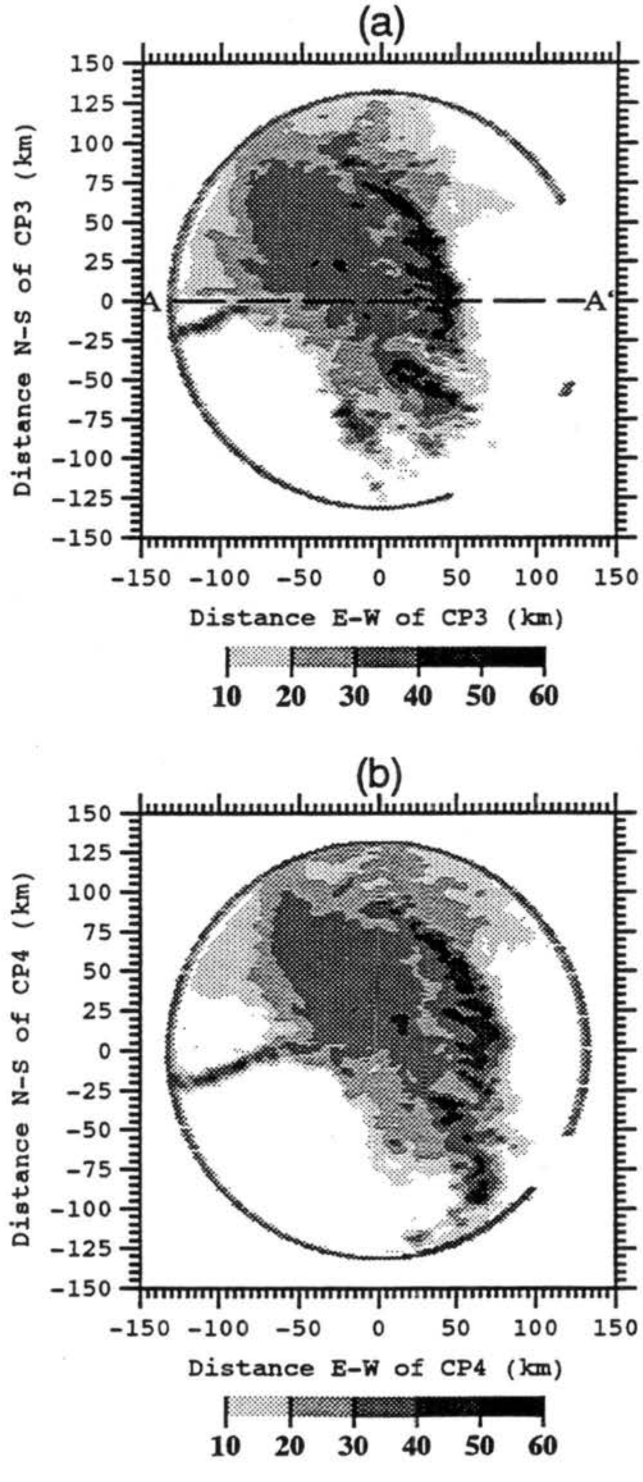

Figure 4.4: Low level (2.5 km) horizontal cross-sections of radar reflectivity (dBZ; gray shading) from the CP3 radar on 28 May 1985 at: (a) 1120 UTC; (b) 1148 UTC.

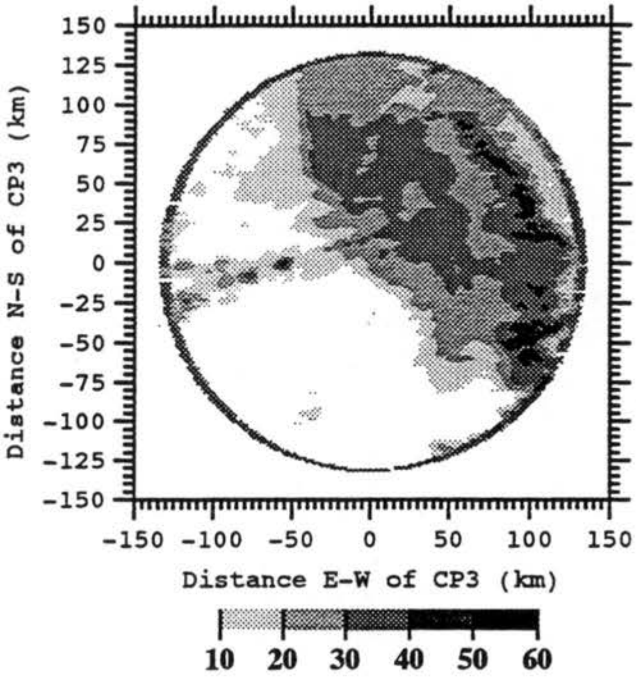

Figure 4.5: Same as 4.4 except at 1225 UTC.

UTC (Fig. 4.4b), the notching had broadened and penetrated deeper into stratiform echo. Also at this time, the line of convection on the southern side of the rear inflow intensified. Approximately 35 minutes later (Fig. 4.5) the inflow notching began to deform the northern portion of the stratiform echo into a hook-like pattern. This feature is a good indication that the cyclonic mesovortex circulation was intensifying, which will be confirmed by the dual-Doppler derived wind fields in the following section.

Vertical cross-sections of reflectivity and storm relative horizontal flow are depicted in Fig. 4.6 (along A-A' in Fig. 4.4a). The convective region was evident in the reflectivity pattern from x=25 to x=50 km, with the 30 dBZ contour extending up to 8 km AGL. It appears that there was a progression of cells from the leading edge rearward. A mature cell was at x=45 km and a decaying cell was centered at x=30 km. This indicates that new convection was forming out ahead of the older convection as the low-level convergence between the gust front and the environment overtook the previously leading convective cell. This is consistent with the conceptual model of a mature squall line from Houze *et al.* (1989). The dashed line at z=3.9 km indicates the melting level estimated by the 1200 UTC OKC sounding. Behind the convective line, a noticeable "bright-band" signature (>30 dBZ) can be seen immediately below the melting level.

Strong FTR flow (>25 ms^{-1}) into the convective line can be seen near x= -50 km. The FTR flow sloped upward toward the rear of the storm. A rear inflow jet descended from 8 km through the stratiform region to the surface near the convective line. This rear inflow jet was approximately coincident with the notching in the echo pattern in Fig. 4.4a, suggesting that the inflow was very dry (possibly due to subsidence) and hence eroded the stratiform echo through the processes of evaporation and sublimation. Negative buoyancy resulting from the evaporative and sublimational cooling was likely responsible for the descent of the rear inflow jet through the stratiform region. The initiation of the rear inflow jet above 8 km is consistent with the theory of Stensrud *et al.* (1991), in which they describe a sublimationally induced mesoscale downdraft and subsequent rear inflow. They

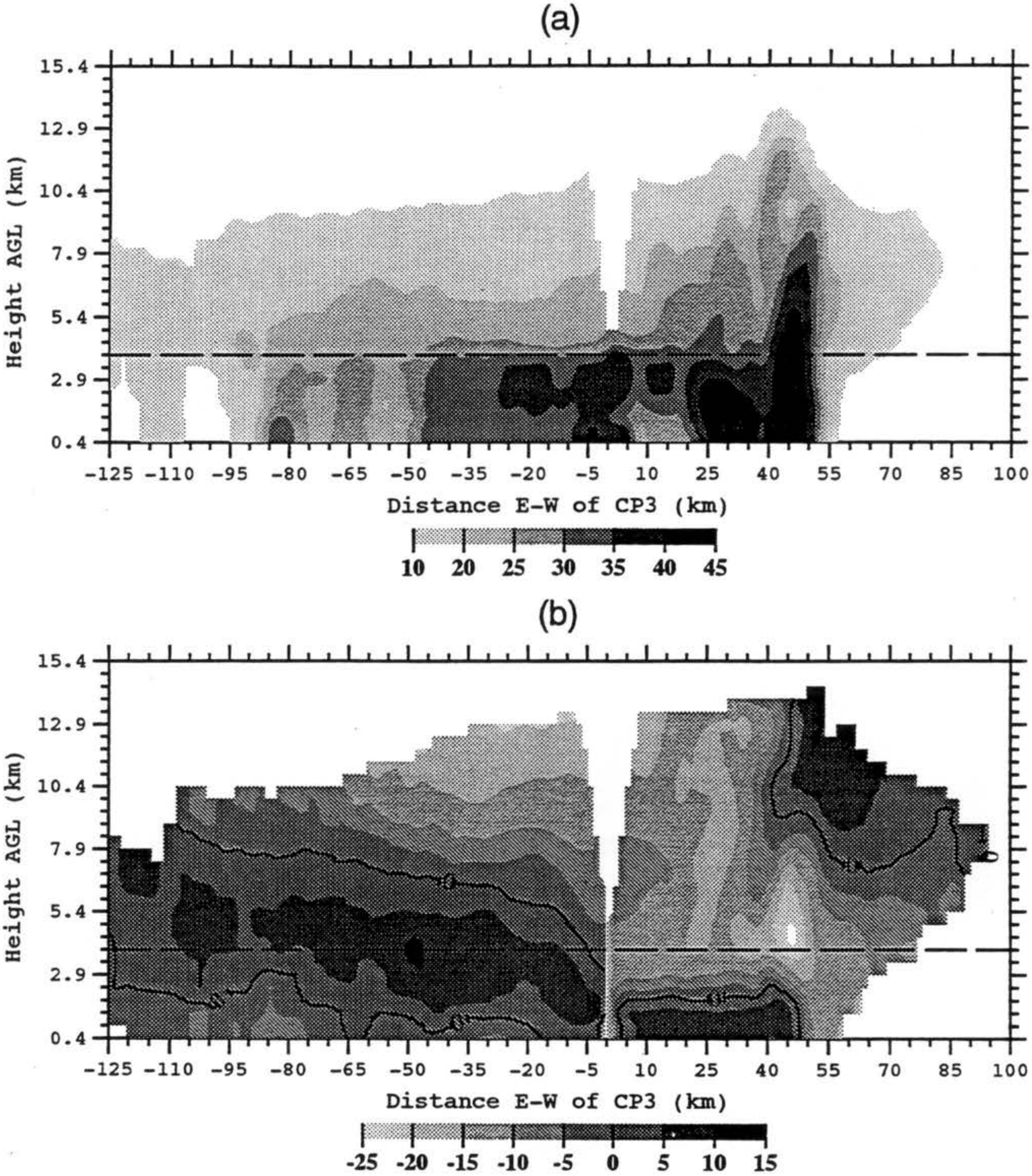

Figure 4.6: Vertical cross-section along the 300°-120° azimuths from the CP3 radar at 1120 UTC, 28 May 1985. (a) reflectivity (dBZ; gray shading); (b) storm relative velocity (ms^{-1}).

hypothesize that sublimation beneath the rear anvil of the trailing stratiform region creates negative buoyancy which transports higher momentum air from upper-levels to mid-levels, thus initiating the mesoscale downdraft and rear inflow. At this point another mechanism may contribute to the acceleration of the rear inflow jet. Smull and Houze (1987) propose that rear inflow jets are a dynamical response to mid-level mesolows in the trailing stratiform region. The mid-level mesolow is believed to be a hydrostatic response to a positive buoyancy anomaly above the melting level (due to latent heat release in the mesoscale updraft) and a negative buoyancy anomaly below (due to evaporative cooling and melting; Brown 1979, Leary and Houze 1979). The rear inflow is accelerated toward the convective line by this mid-level pressure gradient and accelerated downward by cooling due to sublimation, melting and evaporation. Strong low-level convergence was situated at x=50 km, where the rear inflow jet extended to the surface and met the oncoming environmental flow.

4.4 Dual-Doppler data

Dual-Doppler analyses of this case were performed using data from the NCAR CP-3 and CP-4 C-band Doppler radars, which were separated by 62 km in PRE-STORM, along a baseline oriented NNW-SSE. The first analysis captured the southern anticyclonic vortex in the "west" lobe of the dual-Doppler domain (Fig. 3.3). The second analysis is for the "east" lobe of the dual-Doppler domain captured the mesovortex couplet in the stratiform region and a portion of the mature squall line. The final dual-Doppler volume (also in the "east" lobe) depicts the mature cyclonic vortex dominating the stratiform circulation.

4.4.1 Analysis at 1050 UTC

A horizontal cross-section at z=2.4 km AGL (Fig. 4.7) reveals a strong storm-relative anticyclonic circulation on the southern flank of the MCS. This feature is quite similar to the southern counterpart of the "bookend vortices" (Fig. 4.8) as simulated by Weisman (1993), Skamarock *et al.* (1994) and Davis and Weisman (1994). The closed anticyclonic circulation was relatively shallow, being confined between 2 and 3 km AGL, had an average relative vorticity of -10^{-3} s^{-1} and a diameter of at least 85 km at 2.4 km AGL. Although the low-level reflectivity field at this time (Fig. 4.7) provides only a limited view of the MCS, it still shows that the convective system was beginning to show signs of asymmetry. The southern portion of the MCS was composed mainly of convective elements, while a small but developing trailing stratiform region was visible farther northward. There was strong southeasterly system-relative inflow into the convective elements, supplying warm, moist (high θ_e) air to the storm. The anticyclonic circulation was located in the developing stratiform region. The relatively low reflectivities on the northwest side of the vortex seem to indicate drier air was being entrained from the environment on the western edge of this system.

An east-west cross-section taken along the line A-A' (Fig. 4.9) depicts a deep and intense cell on the southern end of the MCS, possessing a reflectivity core of 45-50 dBZ extending to 8 km AGL. Convergence existed at low- and mid-levels in the reflectivity core, while strong divergence was present above 10 km. Maximum vertical velocities exceeded 15 ms^{-1} near 9 km. This cell most likely developed recently on the leading edge of the gust front depicted by the surface θ_e field in Fig. 3.4b. The convection farther to the north (cross-section from B-B', Fig. 4.10) was consistent with the mature squall-line conceptual model depicted in Houze *et al.* (1989). This B-B' cross-section indicates a leading convective cell (x = -15 km), a decaying cell following the leading cell (x = -30 km) and a transition zone (x = -45 km) separating the convective and stratiform regions.

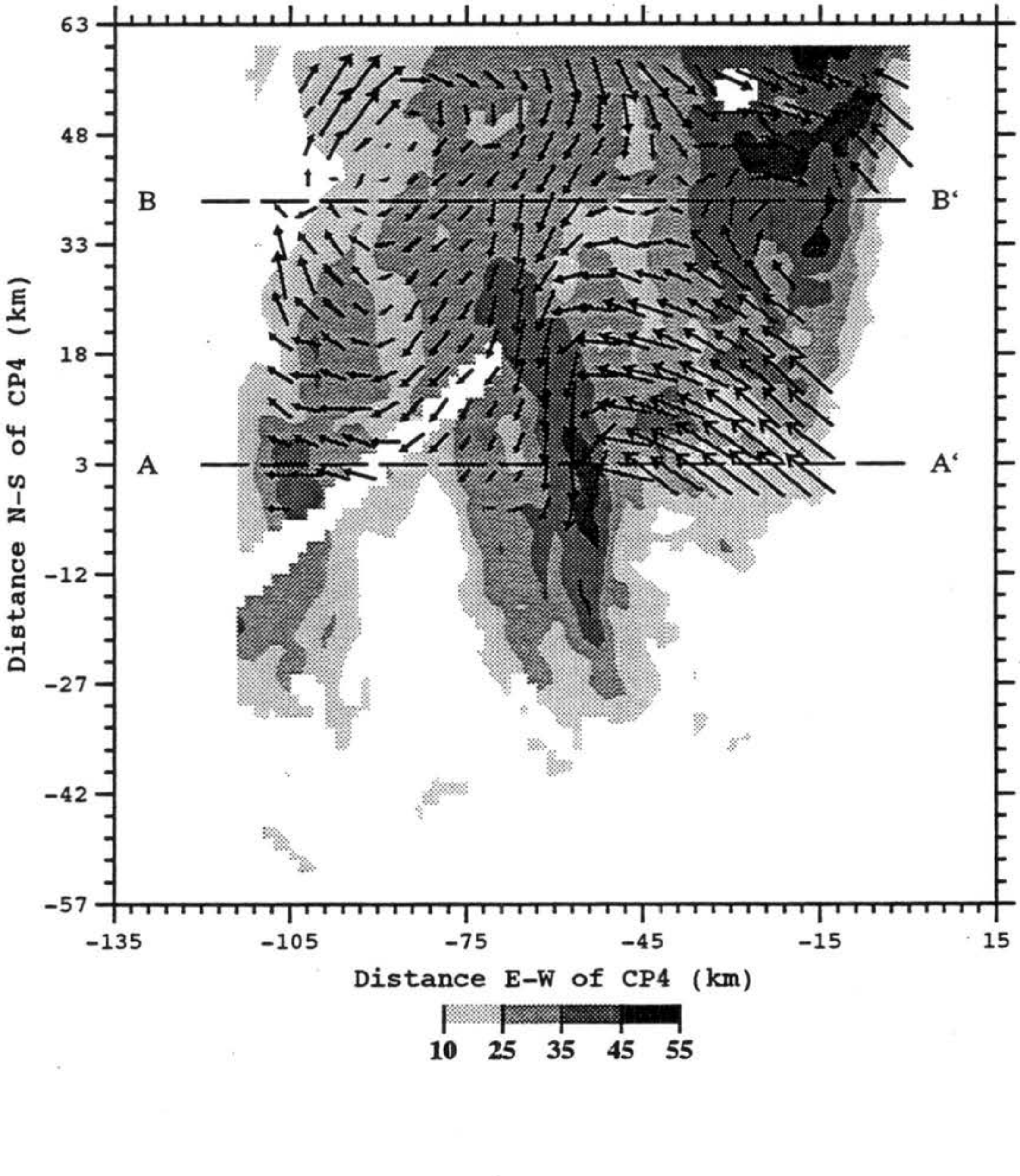

Figure 4.7: Low level (2.4 km) horizontal cross-section of reflectivity (dBZ; gray shading) and storm relative wind vectors (ms^{-1}; wind vectors 4.5 km long indicate a 20 ms^{-1} wind) from the 1050 UTC dual-Doppler analysis.

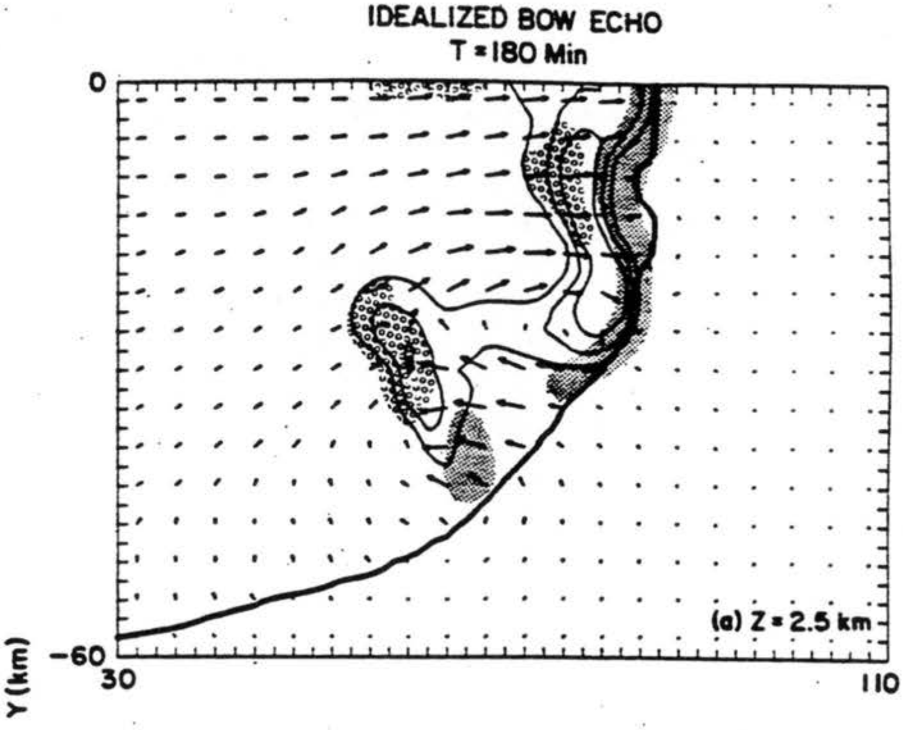

Figure 4.8: Horizontal cross section of rainwater concentration and storm relative flow vectors at 2.5 km, 3 hr into bow echo simulation. Rainwater contoured at 2 g kg^{-1} intervals. Wind vectors 2 grid intervals long = 25 ms^{-1} (from Weisman 1993).

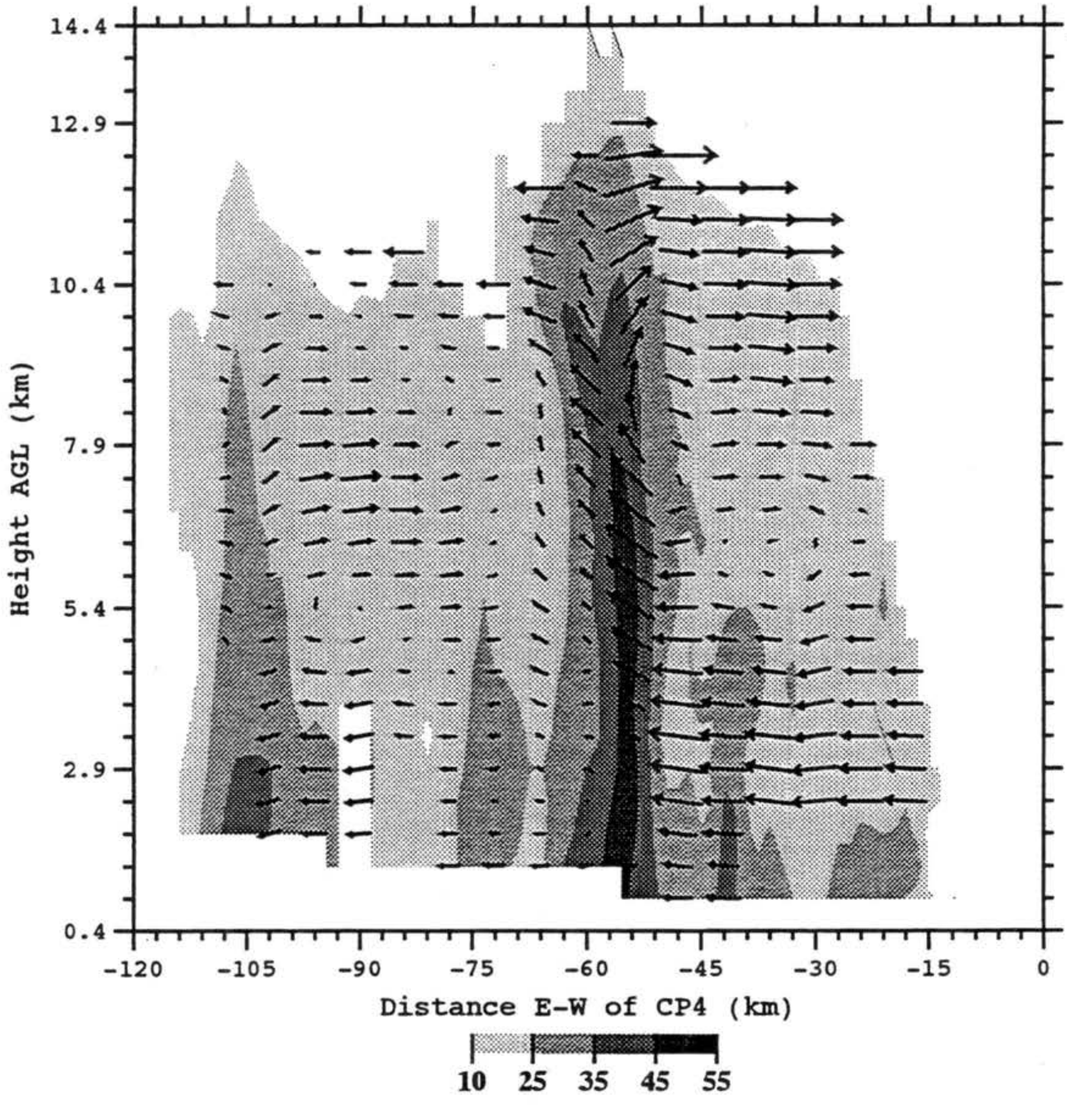

Figure 4.9: Vertical cross-sections of reflectivity (dBZ; gray shading) and storm relative wind vectors (ms^{-1}; wind vectors 4.5 km long indicate a 20 ms^{-1} wind) from the 1050 UTC dual-Doppler analysis along A-A'.

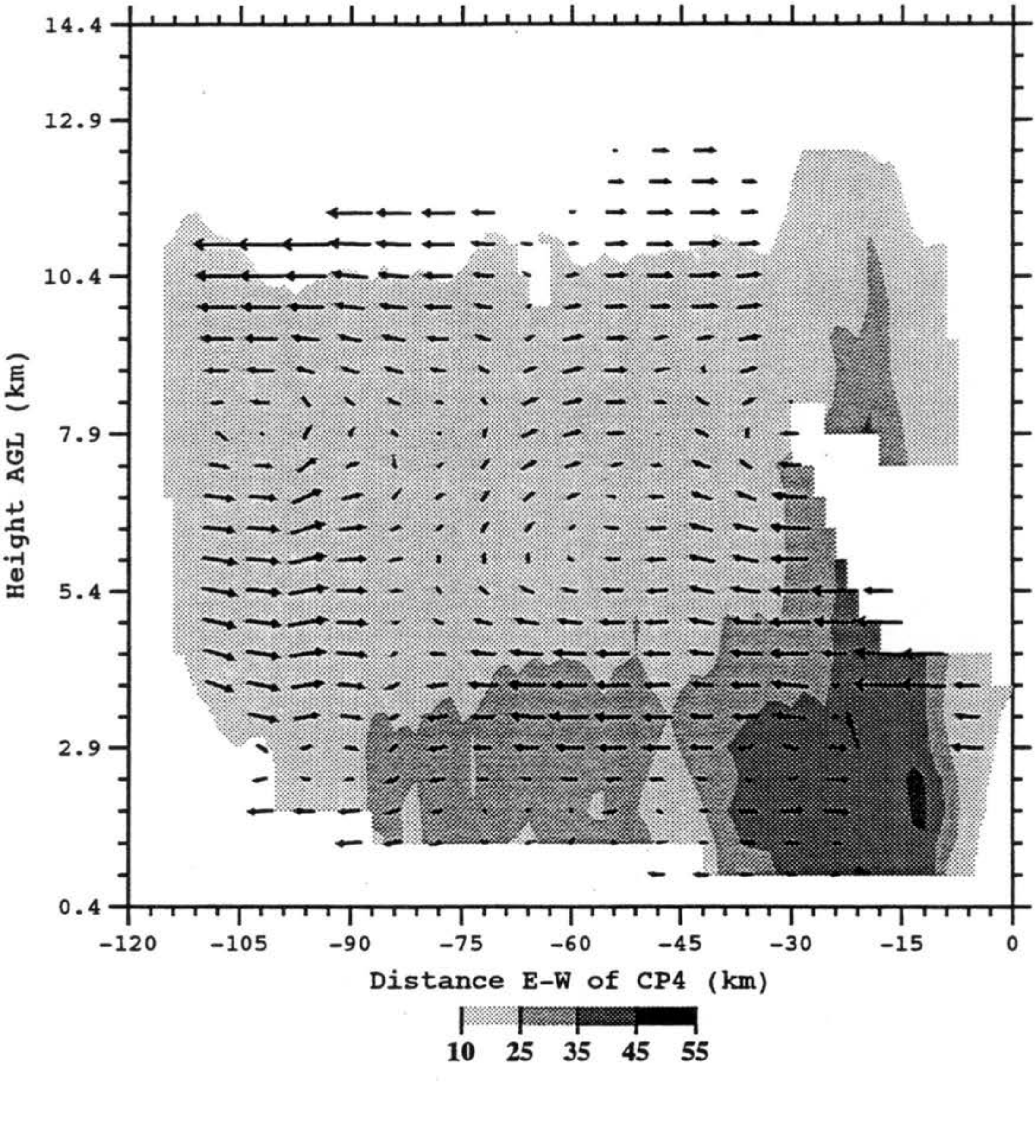

Figure 4.10: Same as 4.9, except along B-B'.

A mesoscale FTR flow emanated from the convective line and converged with a descending RTF flow at mid-levels near the back edge of the stratiform region. approximately coincident with the location of the center of the vortex. The fact that the developing convection was on the southern flank of the MCS and that the more mature convection accompanied by a stratiform region was further to the north is consistent with modeling studies of long lived convective systems that include Coriolis effects (Skamarock *et al.* 1994).

4.4.2 Analysis at 1140 UTC

A pair of counter-rotating vortices were observed in the dual-Doppler domain at this time. Horizontal cross-sections of storm-relative velocity and reflectivity (Figs. 4.7, 4.8) reveal a closed cyclonic circulation in the northern portion of the trailing stratiform region. The closed anticyclonic circulation present in the southern portion of the MCS was closer to the convective line than in the previous analysis. Above the 2.4 km level, the anticyclonic circulation was no longer closed and the cyclonic circulation appeared to tilt northwestward out of the dual-Doppler domain. The relative vertical vorticity in the southern vortex was as large as -2×10^{-3} s^{-1}, while the northern vortex was slightly weaker ($\sim10^{-3}$ s^{-1}). The vortex pair was separated by a strong rear inflow jet (10-15 ms^{-1}) that penetrated to the convective line. Arguments for the presence of an asymmetric structure at this time are stronger than in the previous analysis. It appears that the presence of the counter-rotating circulations not only deforms the shape of the system as the rear inflow jet between the circulations intensifies and bows the central portion of the convective line outward, but also creates a more expansive stratiform precipitating region to the north and enhances the convection to the south of these circulations.

Vertical cross-sections of reflectivity and relative velocity illustrate the differences between the northern and southern portions of the system. The cross-section along C-C'

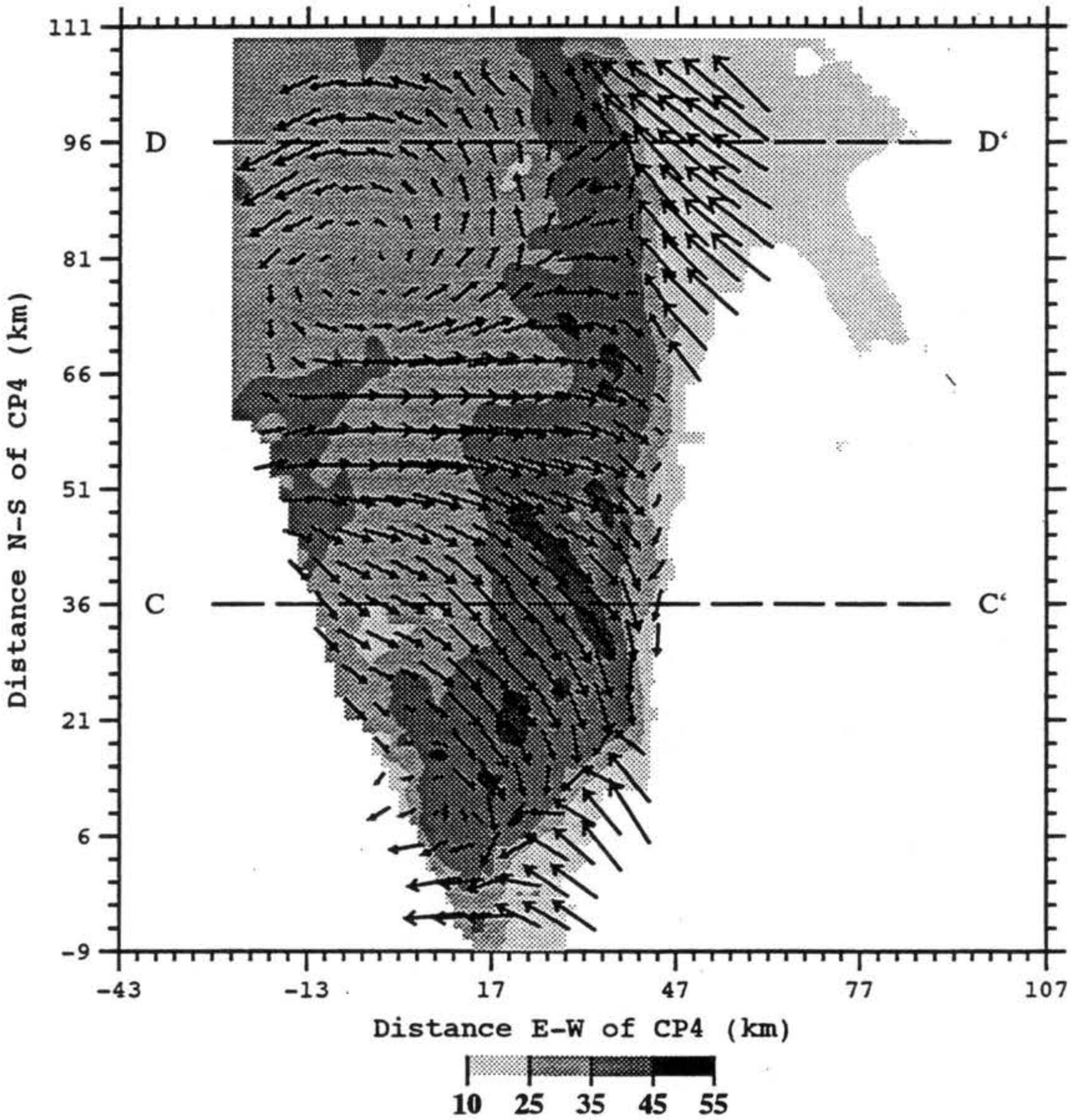

Figure 4.11: Low level horizontal cross-section of reflectivity (dBZ; gray shading) and storm-relative wind vectors (ms^{-1}; wind vectors 4.5 km long indicate a 20ms^{-1} wind) from the 1140 UTC dual-Doppler analysis 1.9 km.

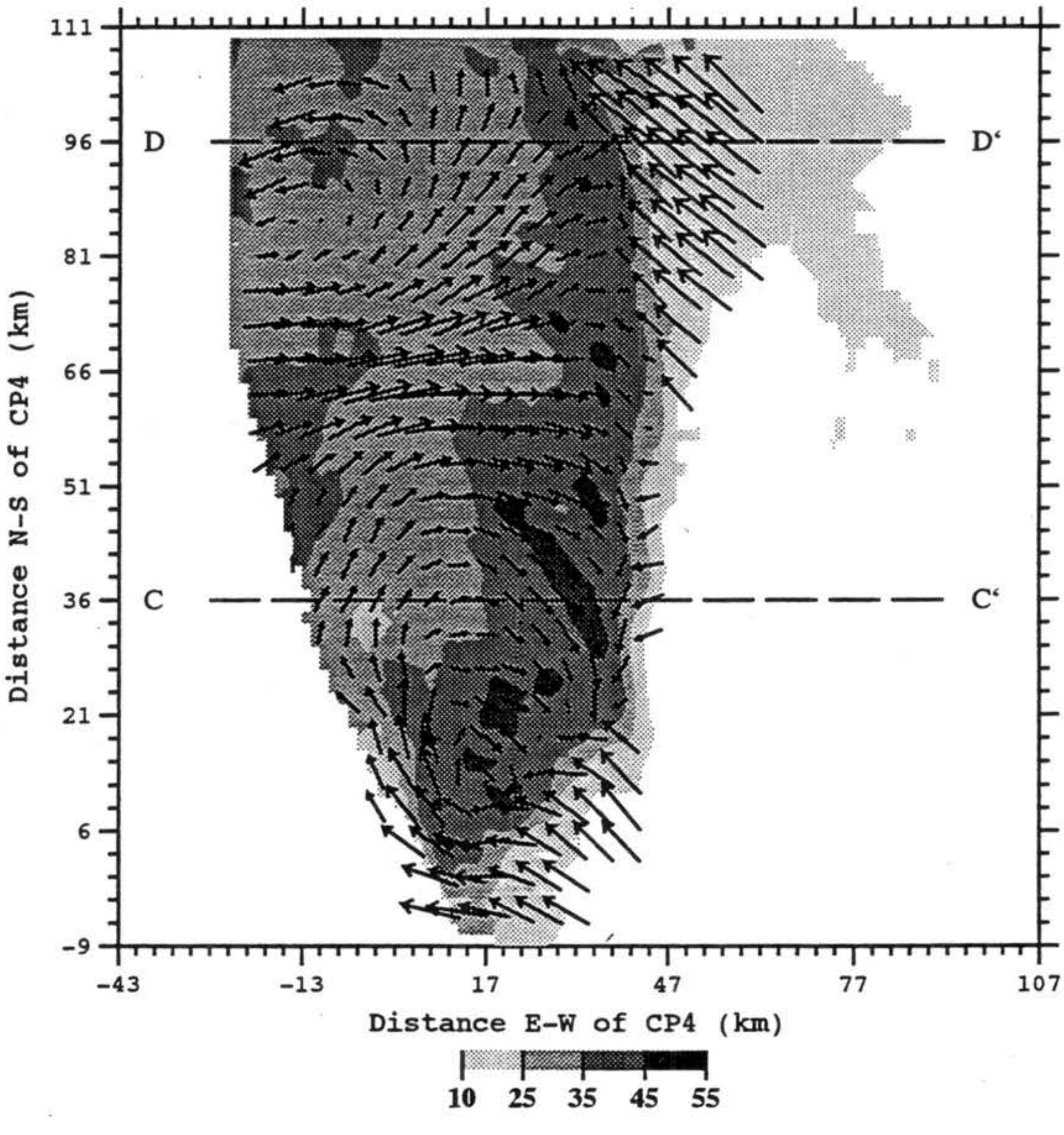

Figure 4.12: Same as 4.11, except at 2.4 km.

(Fig. 4.13) is representative of the southern, intense portion of the MCS, and the cross-section along D-D' (Fig. 4.14) is representative of the northern portion of the MCS, containing weaker convection and more extensive stratiform rain. The southern portion of the system was characterized by much stronger system relative FTR and RTF flow than found in the northern portion of the MCS. The low-level RTF flow contributed to enhanced low-level convergence at the leading line, resulting in stronger forcing of the convection in this region. Simulations of long lived convective systems by Skamarock *et al.* (1994) show that the deflection of the low-level cold pool to the right of the storm motion by the rotation of the Earth creates enhanced low-level convergence and subsequently stronger convection on the southern side of eastward propagating convective systems. The stronger θ_e gradient in the surface mesonet data in the southern portion of the dual-Doppler domain (see Fig. 3.4c) supports this hypothesis.

Along D-D' (Fig. 4.14), the RTF flow was more elevated (3-5 km) and was replaced at low-levels by FTR flow. This FTR flow was the northern branch of the cyclonic circulation as viewed in this cross-sectional sense. It appears that the rear inflow jet was blocked by the low-level cyclonic circulation such that the low-level convergence in the vicinity of the convective line was not as strong as it was in Fig. 4.13, where the leading edge of the rear inflow converged with the front to rear flow at the lower levels. Thus the northern portion of the cyclonic circulation contributes to the weakening of convection to the north, while the northern portion of the anticyclonic circulation (as well as the southern part of the cyclonic circulation) enhances the low-level rear inflow and hence the convection to the south.

4.4.3 Analysis at 1314 UTC

By 1314 UTC the intensity and depth of the cyclonic circulation had increased dramatically and the anticyclonic circulation was almost non-existent. The cyclonic

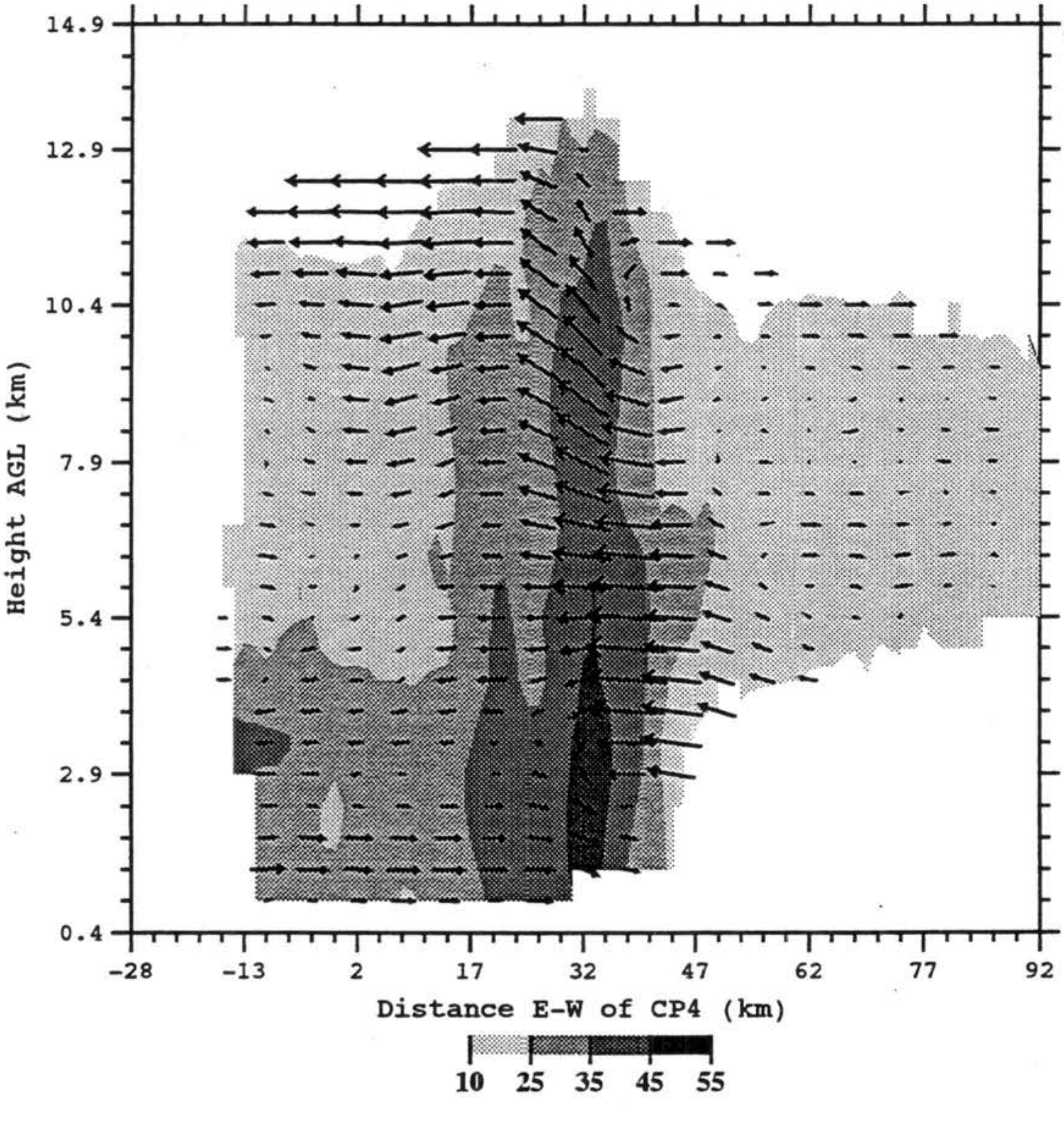

Figure 4.13: Vertical cross-sections of reflectivity (dBZ; gray shading) and storm relative wind vectors (ms^{-1}; wind vectors 4.5 km long indicate a $20ms^{-1}$ wind) from the 1140 UTC dual-Doppler analysis along C-C'.

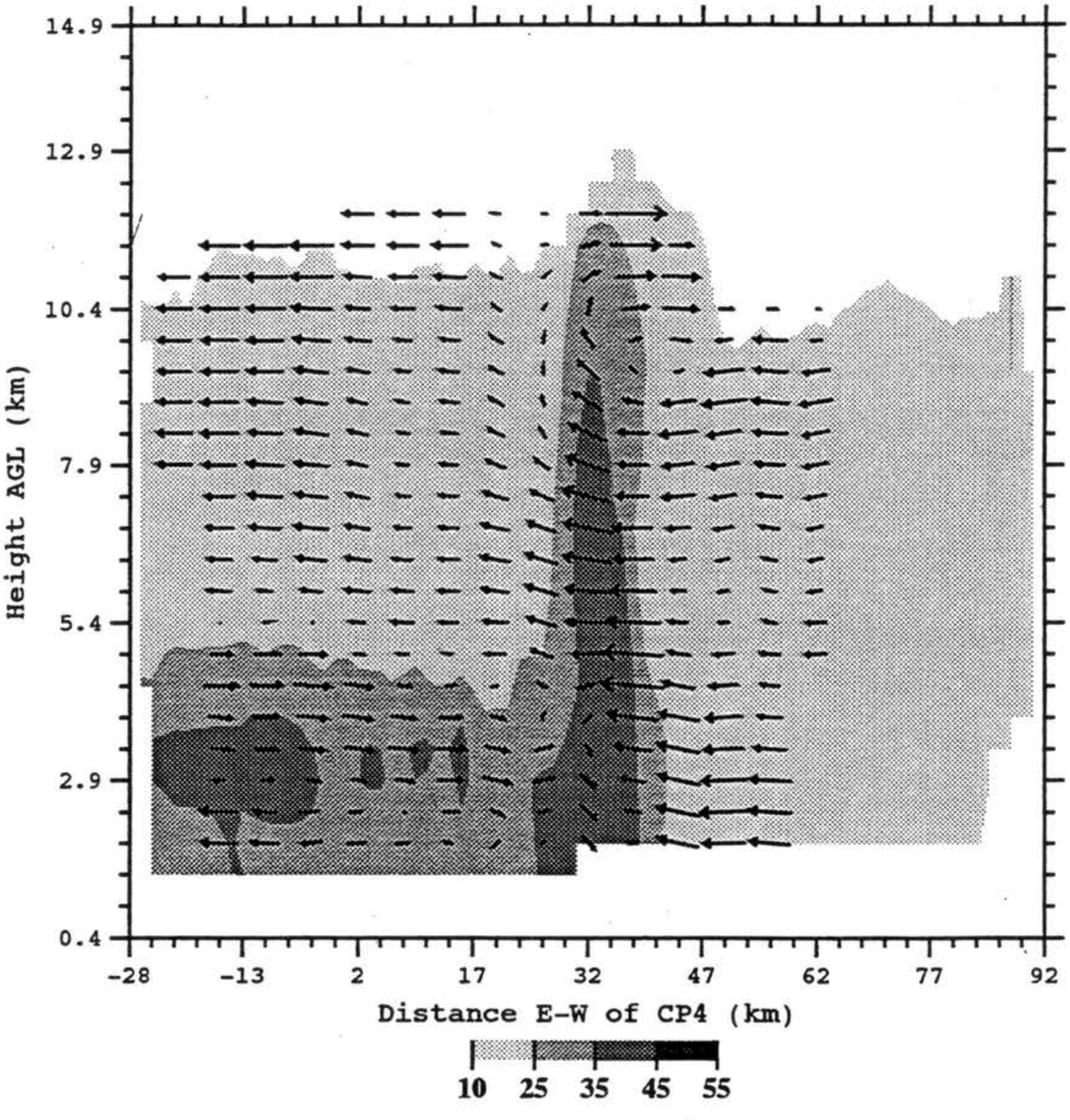

Figure 4.14: Same as 4.13, except along D-D'.

circulation was closed from 2-9 km, with the strongest vorticity located in vicinity of the melting level (3.9 km). At 2.9 km (Fig. 4.15) the cyclonic vortex dominated the wind field in the northern portion of the stratiform region. In sensitivity studies with Coriolis effects, Skamarock *et al.* (1994) found that the anticyclonic circulations in their bow echo simulations were weakened considerably as the positive buoyancy anomaly in the mesoscale updraft (FTR flow) was deflected to the north by the Earth's rotation over time. A similar effect may have contributed to the spin down of the anticyclonic circulation from 1140-1314 UTC.

The precipitation pattern at 1314 UTC (Fig. 4.15) had become highly asymmetric due to the extended presence of the cyclonic circulation. On the northern side of the vortex the reflectivities were relatively high (30-35 dBZ), because streamlines in this region originated from the decaying convective elements of the system; thus hydrometeors were being advected into this portion of the vortex, thereby elevating the reflectivities. Growth of hydrometeors in the mesoscale updraft would have also contributed to higher reflectivity in this region. On the southern side of the vortex there was a pronounced lowering of the reflectivity field where drier environmental air was drawn into the rear of the storm by the strong circulation, causing the hydrometeors to evaporate. Additional lowering of the reflectivity in this region can be attributed to subsidence warming in the mesoscale downdraft, enhancing the evaporation process. This notching in the reflectivity field was present in the single-Doppler analyses as well (Figs. 4.4, 4.5), suggesting that the cyclonic circulation was present as early as 1120 UTC (dual-Doppler analysis could not confirm the presence of the cyclonic vortex as early as 1120 UTC, because the area of the MCS that contained the MCV at later times was in the baseline of the two radars at 1120 UTC. The circulation at 6.9 km (Fig. 4.16) was still quite strong, but considerably weaker than the circulation at lower levels.

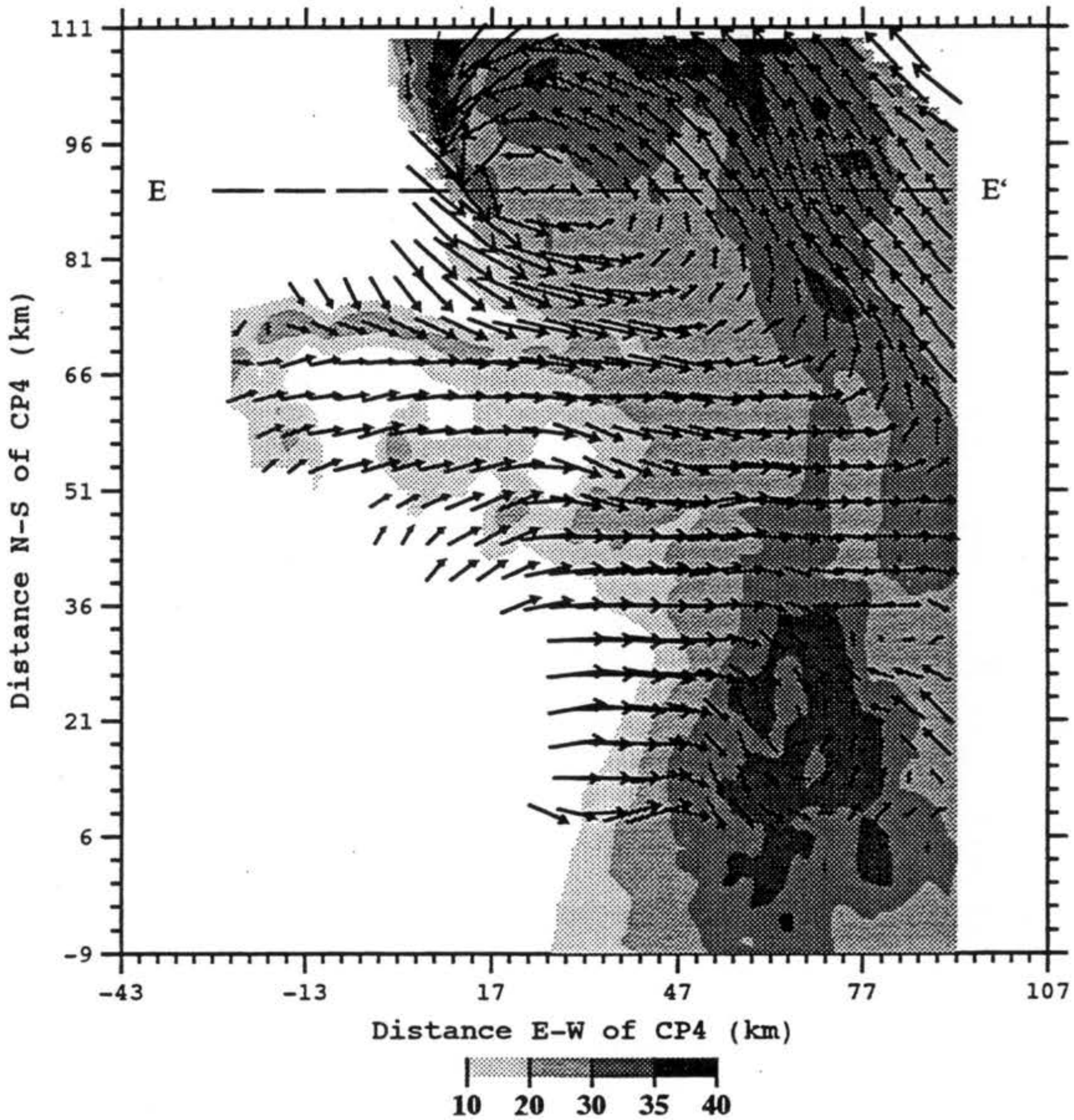

Figure 4.15: Horizontal cross-section of reflectivity (dBZ; gray shading) and storm relative wind vectors (ms^{-1}; wind vectors 4.5 km long indicate a $20ms^{-1}$ wind) from the 1314 UTC dual-Doppler analysis at 2.9 km.

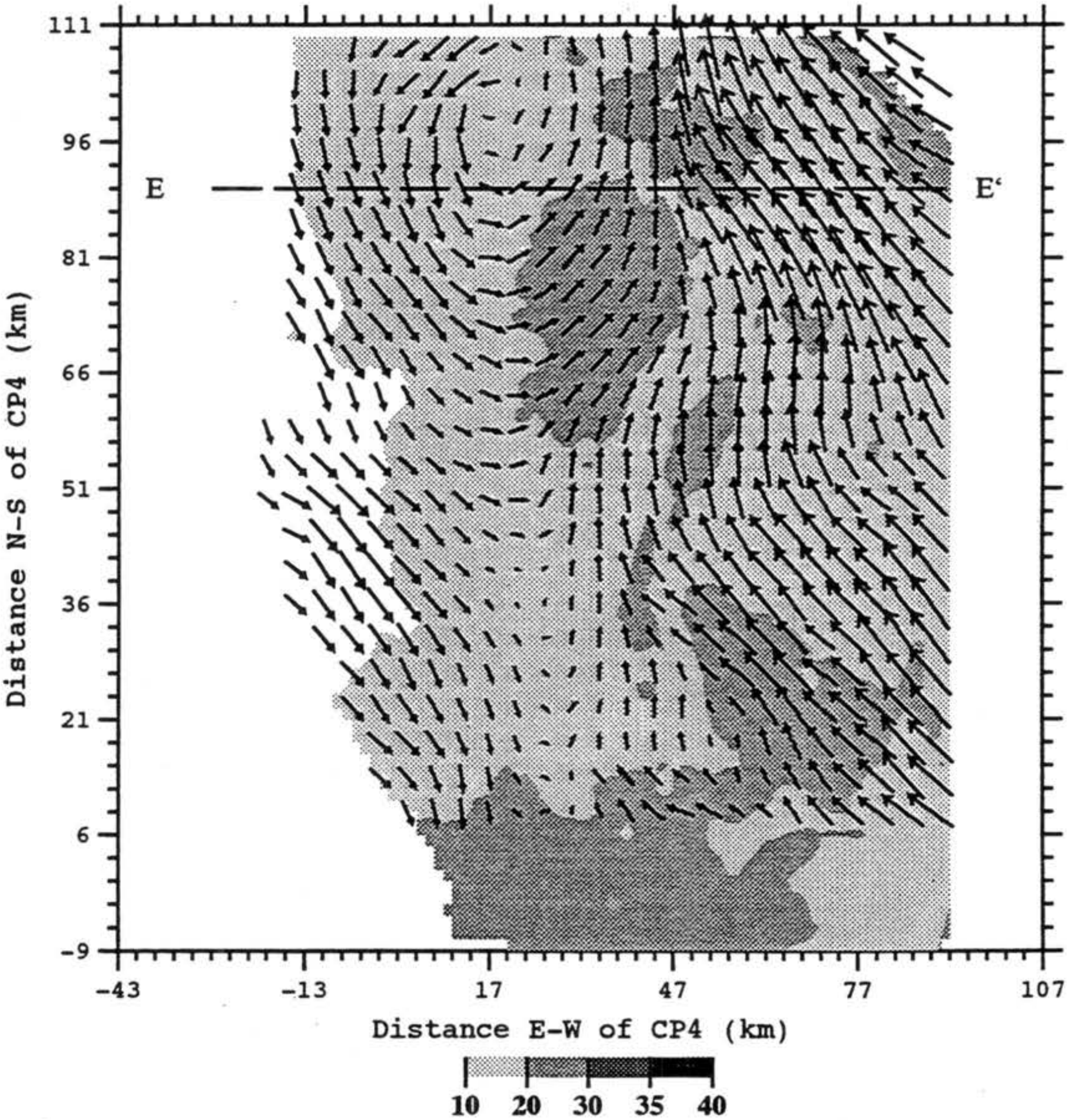

Figure 4.16: Same as 4.15, except at 6.9 km.

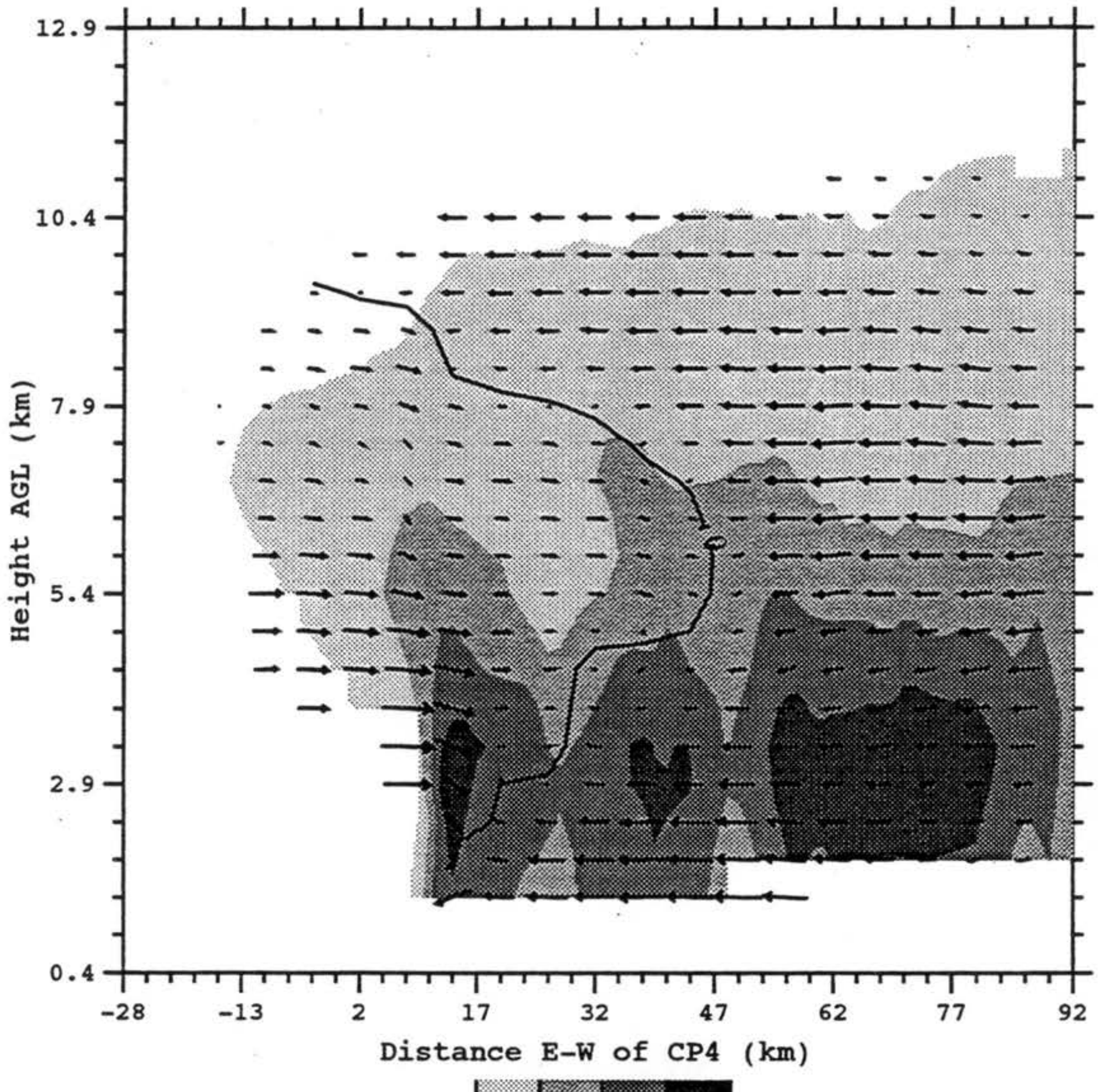

Figure 4.17: Vertical cross-sections along E-E' from the 1314 UTC dual-Doppler analysis of reflectivity (dBZ; gray shading) and storm relative velocity vectors (ms^{-1}; wind vectors 4.5 km long indicate a $20ms^{-1}$ wind).

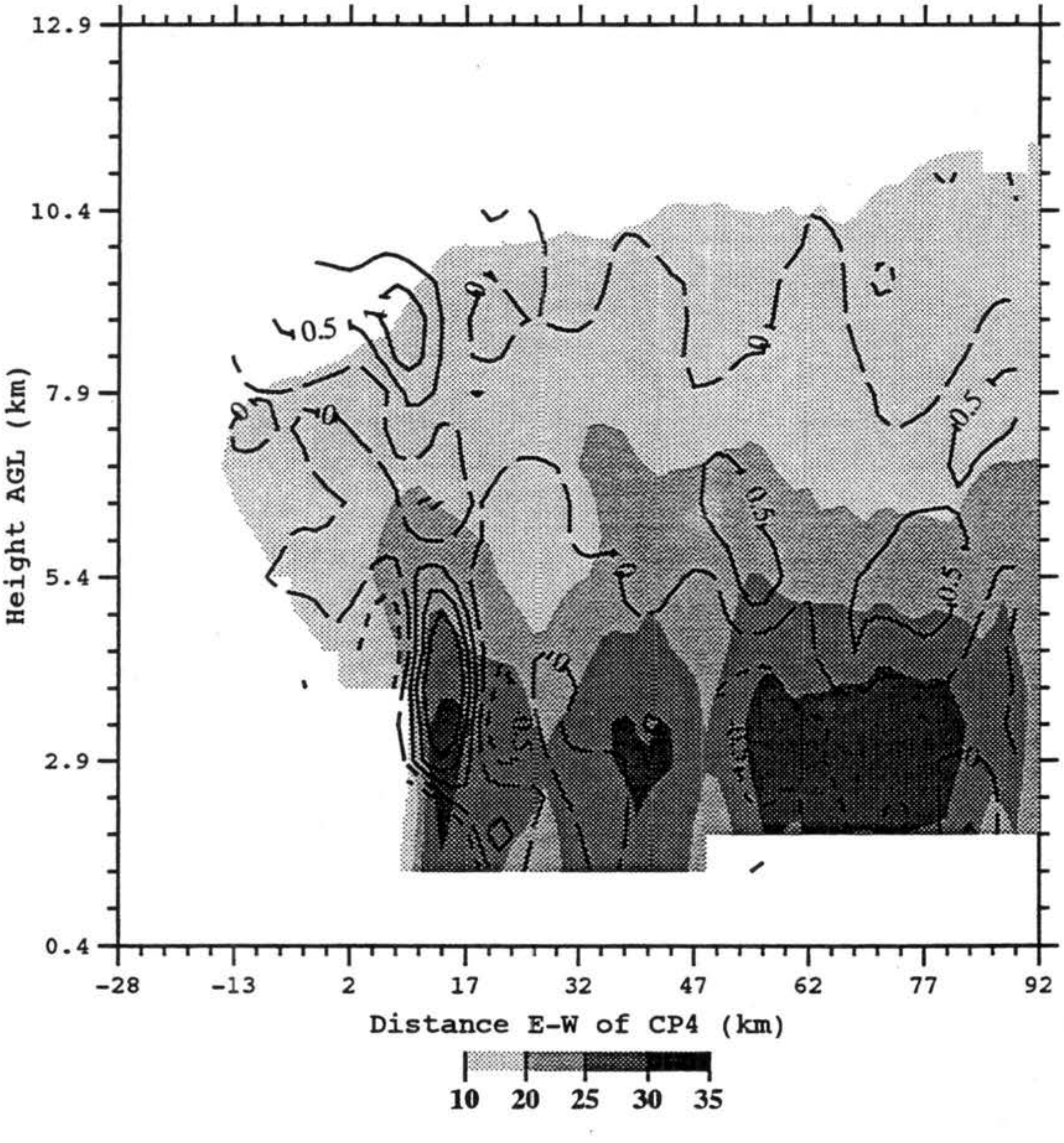

Figure 4.18: Same as 4.17 except for convergence (solid) and divergence (dash) (10^{-5} s^{-1}).

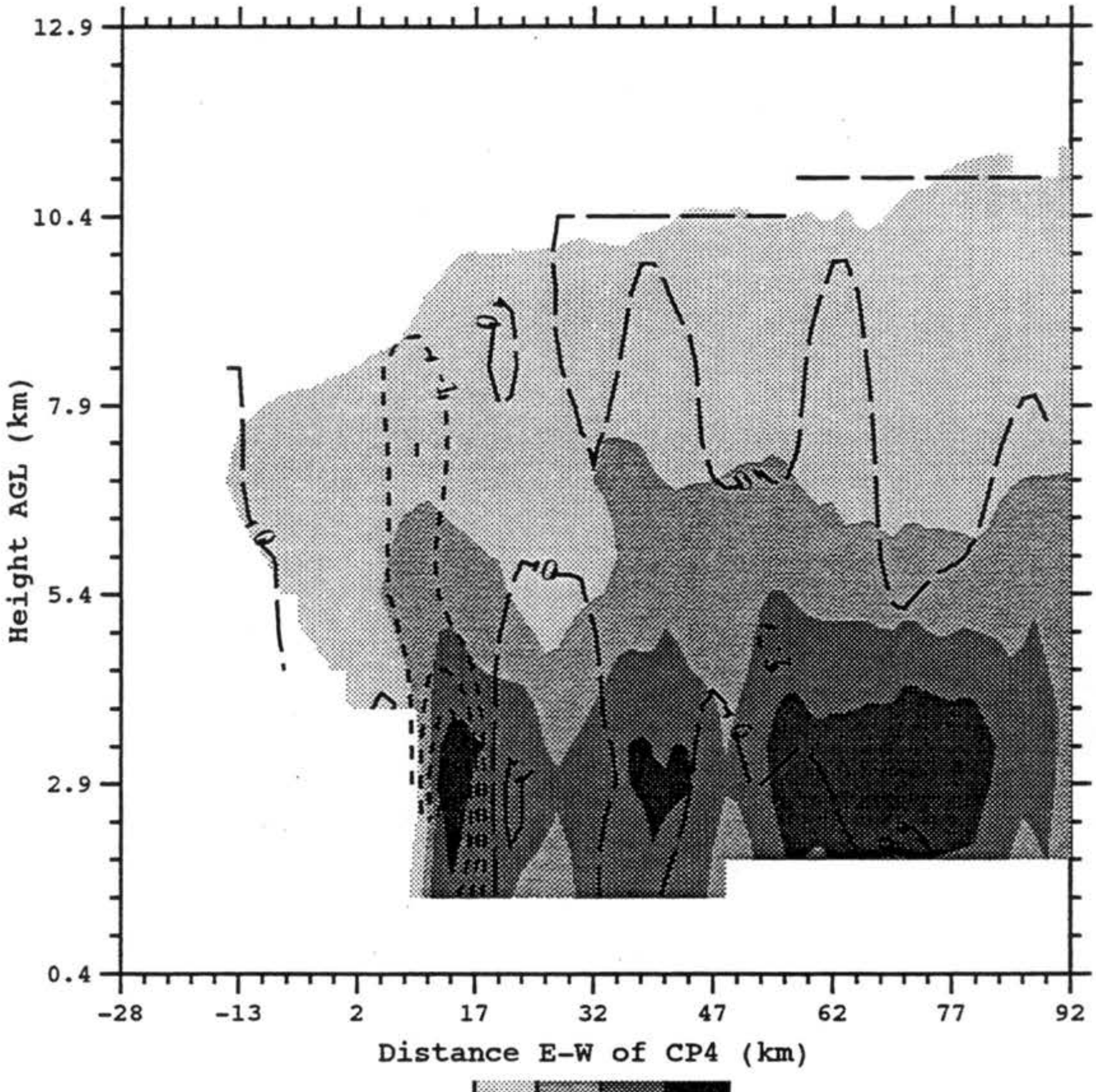

Figure 4.19: Same as 4.17, except for positive (solid) and negative (dash) vertical velocity (ms^{-1}).

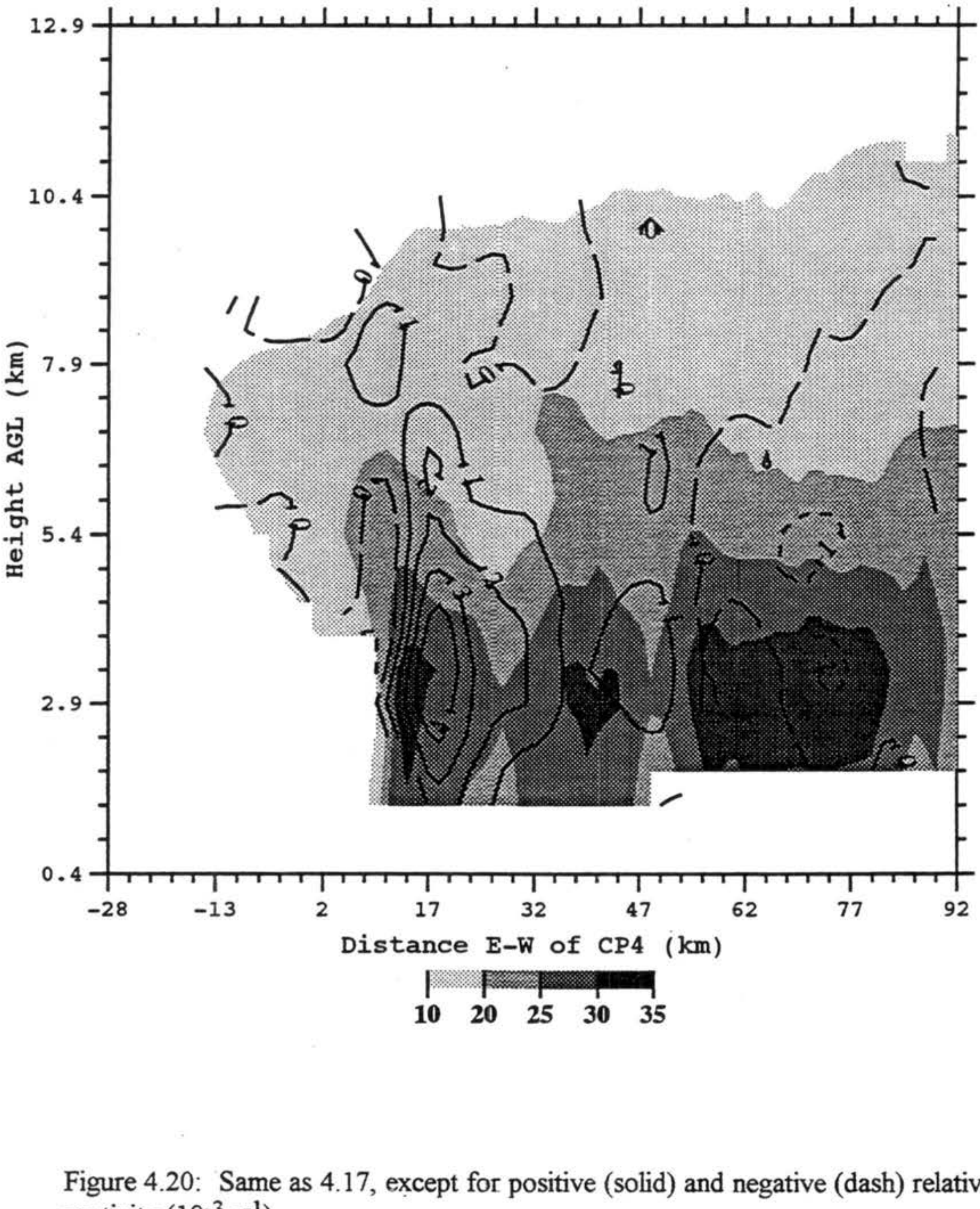

Figure 4.20: Same as 4.17, except for positive (solid) and negative (dash) relative vertical vorticity (10^{-3} s^{-1}).

Cross-sections along E-E' (Figs. 4.17-4.20) provide information regarding the vertical structure of the stratiform region containing the MCV. The storm relative velocity vectors (Fig. 4.17) indicate deep front to rear flow in the trailing stratiform region of the MCS, with a rear inflow jet encroaching on the rear edge of the system. The solid line indicates the demarcation between the FTR and RTF flows. The rear inflow entered the storm as high as 9 km, but was strongest near the melting level (3.9 km). The convergence field (Fig. 4.18) indicated a maximum ($>2\times10^{-3}$ s^{-1}) in the same region where the rear inflow was strongest. There was also strong divergence below the convergence maximum, both of which contributed to the strong downward vertical velocity (< -4 ms^{-1}) shown in Fig. 4.19. Exceptionally rapid descent (6-9 ms^{-1}) has also been obseved on the back edge of stratiform regions for two other PRESTORM cases (Stumpf *et al.* 1991, Johnson and Bartels 1992). This type of flow pattern is thought to be associated with strong surface pressure gradients and wake lows. The pressure retrieval (Ch. 6) will show that strong mid-level pressure gradients associated with the intense cyclonic vortex generated strong convergence and subsequent downward motion in this case. Upon comparison of the vertical velocity and convergence features with the relative vertical vorticity field (Fig. 4.20), it is seen that they were nearly coincident with the maximum in relative vertical vorticity ($>4\times10^{-3}$ s^{-1}). This would seem to indicate the presence of vortex stretching, creating a spin-up of the cyclonic circulation at this time. The following vorticity analysis will confirm this.

Chapter 5

VORTEX ANALYSIS

5.1 Motivation

Previous observational studies of MCVs have focussed on documenting the thermodynamic and kinematic structure of these intriguing features, in order to get a better idea of why they exist. Studies using sounding data (e.g., Bartels and Maddox 1991, Menard and Fritsch 1989, Brandes 1990) have provided the best documentation of the thermodynamic structure of these circulations, yet the coarse resolution of the upper air analyses may not fully capture the essence of the kinematics associated with MCVs. It is in this area that dual-Doppler analyses of MCVs are superior. The higher resolution of the retrieved wind fields provide the basis for detailed kinematic analyses of MCVs. Several published cases have used dual-Doppler data in this manner (e.g., Verlinde and Cotton 1990, Johnson and Bartels 1992, Keenan and Rutledge 1993, Brandes and Ziegler 1993, Jorgensen and Smull 1993). The complex nature and inherently 3-D structure of the MCVs in these cases required that the dual-Doppler derived kinematic fields be averaged over some fixed horizontal domain. This is done in order to produce vertical profiles of the average kinematics within the vortex circulations. The domains used in averaging in these cases were typically defined as rectangular or circular areas enclosing the circulation at mid-levels and the same domain was used for averaging at each vertical level in the data. There are limitations to this approach. First, the closed circulation of an MCV is not necessarilly well represented by a circular or rectangular boundary. Second, the vortex may expand, contract, change shape or orientation with height. Thus, the averaging in these cases is usually subject to aliasing, diluting the actual kinematics of the MCV. This thesis will present kinematic analyses of both cyclonic and anticyclonic MCVs using dual-Doppler averaging with a variable horizontal domain, thus allowing the domain in which the MCV is contained to expand, contract, and change shape or orientation, even with height. Since MCVs are neither cylindrical nor rectangular, this technique provides a more realistic view of the average vortex kinematics.

5.2 Methodology

Previous observational studies of (cyclonic) MCVs have relied on applying areal averaging techniques to get a more simplistic view of the complex kinematic structure within an MCV (Jorgensen and Smull 1993, Brandes and Ziegler 1993, Johnson and Bartels 1992, Keenan and Rutledge 1993). This study is no different in that respect, but a somewhat more sophisticated averaging technique is applied. Instead of defining a rigid boundary at mid-levels encompassing the closed circulation and using the same boundary for averaging at all levels, or simply averaging over the entire horizontal domain, a variable horizontal domain based on a vorticity threshold is used. The selection of the vorticity threshold for the averaging domain is, admittedly, subjective, although it is a good way to isolate the closed circulation from the rest of the data.

The procedure begins with calculating the relative vertical vorticity at each grid point within the dual-Doppler volume. This is done through centered finite differencing using the equation:

$$\zeta = \frac{\partial v}{\partial x} - \frac{\partial u}{\partial y} \qquad (5.1).$$

Vorticity tendencies were then calculated at each grid point using the following equation:

$$\frac{D}{Dt}(\zeta + f) = \underbrace{-(\zeta + f)\left(\frac{\partial u}{\partial x} + \frac{\partial v}{\partial y}\right)}_{stretching} \underbrace{-\left(\frac{\partial w}{\partial x}\frac{\partial v}{\partial z} - \frac{\partial w}{\partial y}\frac{\partial u}{\partial z}\right)}_{tilting} \qquad (5.2).$$

The stretching and tilting terms on the RHS of (5.2) were calculated directly, while the total tendency (LHS) was calculated as a residual. The solenoidal term could not be calculated due to the lack of thermodynamic data, thus the total tendencies indicated here assume the solenoidal generation of vorticity was small compared to the convergence and tilting terms. This assumption is supported by the studies of Skamarock *et al.* (1994) on simulated MCV circulations, who found the solenoidal generation of vorticity to be two orders of magnitude smaller than the generation of vorticity by stretching. Once all the vorticity terms had been calculated, the procedure for defining the horizontal domain enclosing the vortex could begin.

For this purpose, the entire dual-Doppler grids were read into a FORTRAN program. The program would step through each gridded value of relative vorticity, objectively defining areas of vorticity greater than (or less than for the anticyclonic vortex) a certain threshold. Different thresholds were tried until one that best represented the closed circulation at the most levels was chosen. All the grid points within each vorticity feature were horizontally averaged together. Comparisons between the vorticity features defined by the program and the actual wind circulation facillitated the selection of the proper vorticity threshold and the proper vorticity features to be used in the vertical profile. This part of the analysis was subjective. The horizontal averages at each height within the vortex were then combined to provide vertical profiles of vertical velocity, convergence, vertical vorticity, and the terms in the vorticity tendency equation (5.2).

5.3 Analysis of anticyclonic vortex at 1050 UTC

The presence of cyclonic rotation on the northern flank and anticyclonic rotation on the southern flank of bow echo type storms was first postulated by Fujita (1978). Studies discussing the cyclonically rotating MCVs have been numerous in the past ten years (e.g., Brandes 1990, Bartels and Maddox 1991, Jorgensen and Smull 1993, Brandes and Ziegler 1993), but confirmation of the anticyclonic counterpart to the cyclonic MCV has remained elusive. Recent modeling studies (Weisman 1993, Skamarock *et al.* 1994, Davis and Weisman 1994) have suggested that this anticyclonic feature may be a common component of long-lived convective systems that develop in the absence of large scale forcing. It may be that the anticyclonic vortex is shorter lived or more transient than its counterpart, thus making it more difficult to observe.

A vorticity threshold of $< -3\times10^{-4}$ s^{-1} was sufficient to isolate the anticyclonic circulation in this case. This value of vorticity was chosen because the closed circulation in the horizontal wind field was best represented by the area enclosed by this threshold. Although the wind vectors revealed that a closed circulation was confined between 2 and 3 km, the vorticity analysis showed that a strong anticyclonic vorticity signature extended above the closed circulation up to 7 km. The average vorticity values within the vortex ranged from -6.3×10^{-4} s^{-1} at z=1.9 km to -12.2×10^{-4} s^{-1} at z=4.4 km. The vertical profile (Fig. 5.1) shows that the tilting term had a positive tendency (i.e., it was destroying the anticyclonic circulation) throughout the depth of the vortex at this time. The positive contribution by the tilting term was largest below 4 km. The snapshot of the vortex presented here shows that stretching was acting to locally destroy the vortex below 3 km because of the strong divergence in the wind field. Above the melting level, the stretching term dominated the tendency equation, contributing to the spin up of the anticyclonic circulation. The total contribution due to stretching and tilting was to destroy the vortex below and enhance the vortex above the melting level. The vortex-averaged vertical

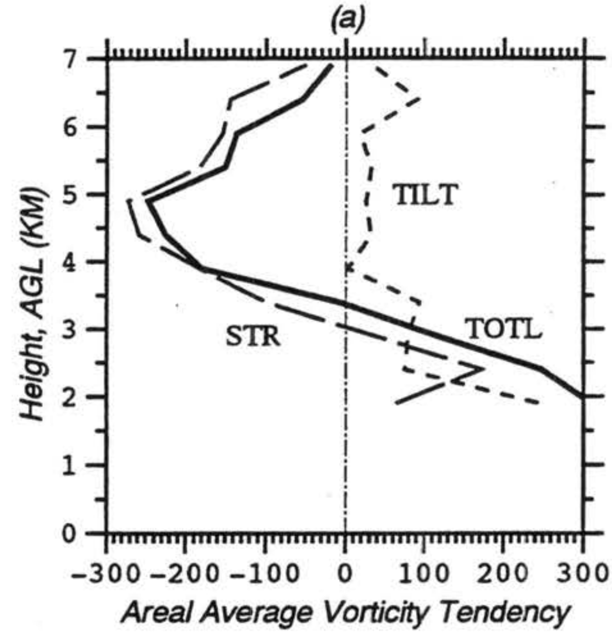

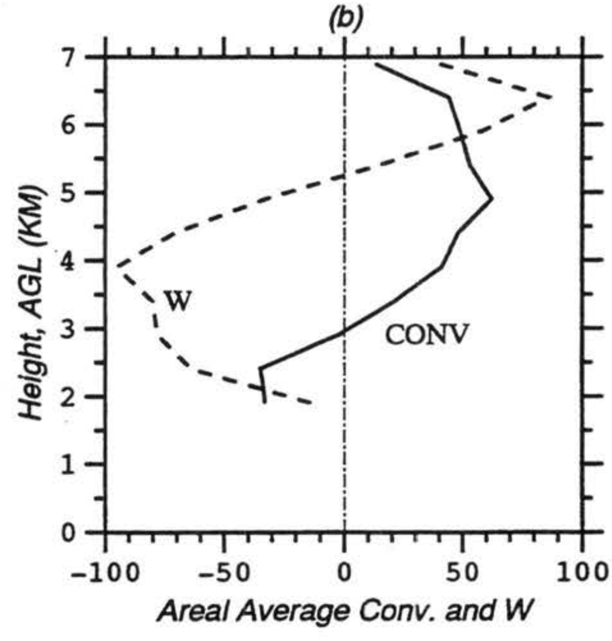

Figure 5.1: Vertical profiles averaged over the anticyclonic vortex at 1050 UTC. (a) relative vertical vorticity tendency (10^{-5} s^{-1} hr^{-1}): tilting (small dash), stretching (large dash) and total (solid). (b) vertical velocity (dash, cm s^{-1}) and convergence (solid, 10^{-5} s^{-1}).

velocity profile (Fig. 5.1b) showed strong mesoscale downward motion below 5 km, approaching -1 ms^{-1} at 3.9 km. Mesoscale ascent was found in the vortex above 5 km and approached 1 ms^{-1} at 6.4 km. A deep layer of convergence (Fig. 5.1b) was found in the vortex at mid-levels, which contributed to the negative tendency (spin up of the anticyclonic circulation) in the stretching term at this instant in time. This convergence can be attributed to the rear inflow jet penetrating the back edge of the stratiform cloud, as seen in Fig. 4.6b.

5.4 Analysis of the cyclonic vortex at 1314 UTC

In the vorticity analysis that follows, a vorticity threshold ($>10^{-4}$ s^{-1}) was used to isolate the closed circulation. The areal averaged convergence profile (Fig. 5.2a) shows the existence of strong divergence at low-levels followed by strong convergence at mid- and upper-levels. The convergence within the vortex was rather deep, extending over 6 km. This deep layer of convergence was in part caused by the confluence of the opposing FTR and RTF flows in this region. Another mechanism for convergence may be associated with a pressure gradient created by the strong rotation. In rotational flow, the square of vorticity is proportional to a low pressure perturbation (Rotunno and Klemp 1982); therefore the existence of strong rotation could lower the pressure in the vortex, causing mass to converge into the circulation. The pressure retrieval in the following chapter confirms the existence of lower pressure in the vortex circulation. Divergence at low-levels existed within the vortex, even though there was strong rotation and lower pressure. This can be explained by the fact that there were strong negative buoyancy effects (melting and evaporation) occurring below the melting level (3.9 km) which contributed to strong downward motion. The mass in the downdraft was forced to diverge as the effects of the ground began to be felt. As would be expected with upper-level convergence and low-level divergence, the average vertical motion (Fig. 5.2b) within

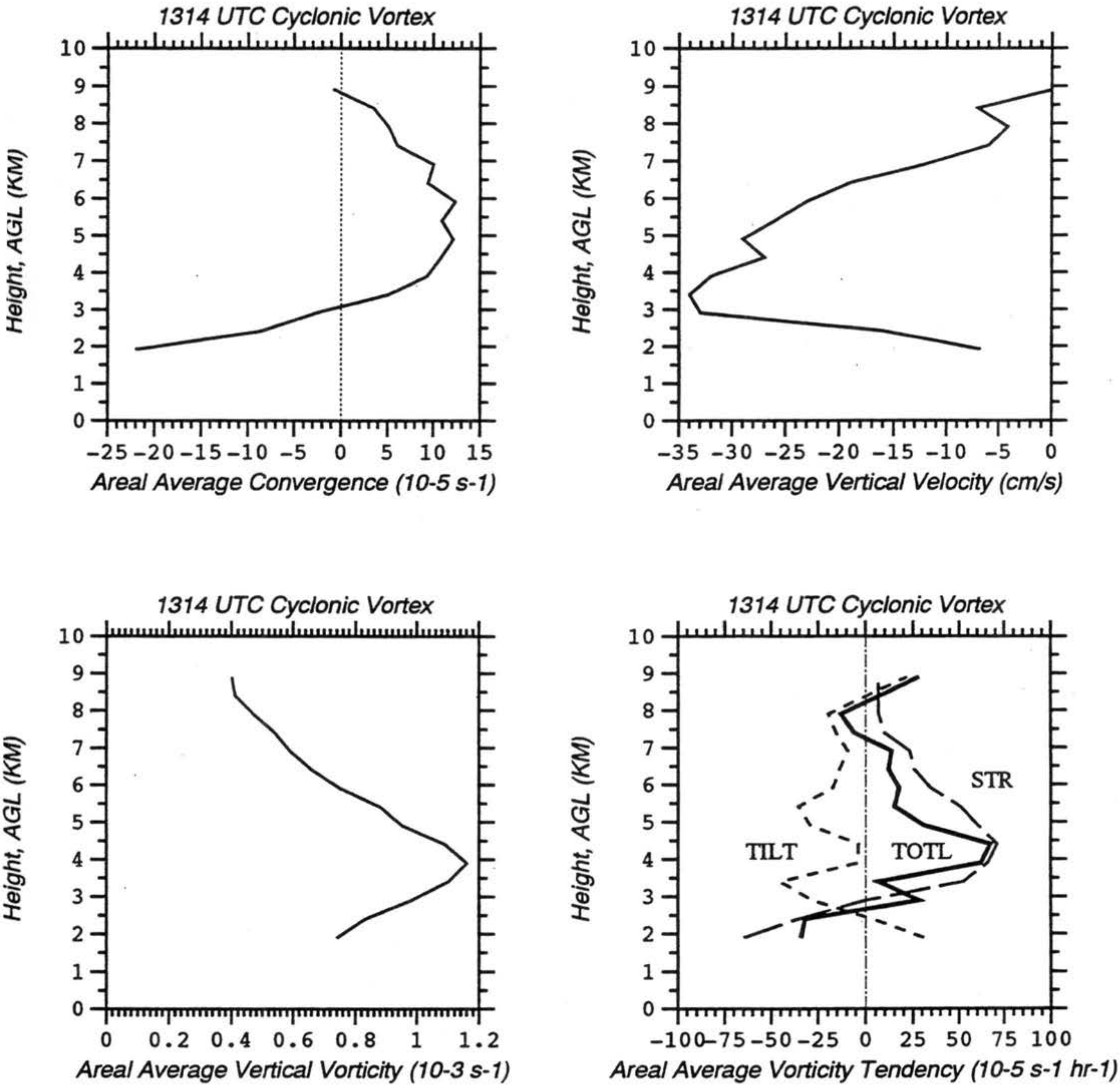

Figure 5.2: Vertical profiles averaged over the cyclonic vortex at 1314 UTC. (a) convergence (10^{-5} s^{-1}); (b) vertical velocity (cm s^{-1}); (c) relative vertical vorticity (10^{-3} s^{-1}); (d) relative vertical vorticity tendency (10^{-5} s^{-1} hr^{-1}): tilting (small dash), stretching (large dash), total (solid).

the vortex was downward. The effects of melting and evaporation can be seen in the layer between 2.9 and 3.9 km, where the average downward velocities exceed 30 cm s^{-1}. The average vertical vorticity profile (Fig. 5.2c) shows a steady increase in vorticity from 1.9 km to a maximum of 1.16×10^{-3} s^{-1} (or 13 times greater than the local Coriolis parameter) at the melting level, and then a steady decrease in vorticity to the top of the closed circulation.

The average vertical vorticity tendency profiles (Fig. 5.2d) show that at this time, the vortex was spinning up (a positive tendency) at nearly all levels. However, below 2.4 km, the tendency was strongly negative, due to the strong divergence creating negative stretching. The contribution of the tilting of horizontal vorticity into the vertical was positive, yet not strong enough to counteract the negative tendency due to stretching. Throughout the depth of the vortex, the tilting term was generally opposite in sign and smaller in magnitude than the stretching term. The "total" vorticity tendency maximum was just above the melting level. The stretching term was maximized at this level, in a region of high vorticity and strong convergence, while the tilting term was relatively small. This analysis suggests that during the mature phase of the MCV, stretching of existing vertical vorticity was the primary mechanism for the maintenance of the circulation. The modeling studies of Zhang (1992), Weisman (1993), Davis and Weisman (1994) and Skamarock *et al.* (1994) propose that tilting of horizontal vorticity into the vertical by differential vertical motion is the primary mechanism for the genesis of MCV circulations, which are subsequently enhanced by horizontal convergence. Since the MCV in this case was already mature at the time it was completely in the dual-Doppler analysis domain, we can only speculate on the mechanisms involved in the generation of the cyclonic circulation.

The vortex averaged profiles of convergence, vertical velocity and vertical vorticity in this study are quite similar in structure, but dissimilar in magnitude to those found by Brandes and Ziegler (1993) using dual-Doppler data. Similar to this study, Brandes and Ziegler found strong mid- and upper-level convergence and low-level divergence in vicinity of the vortex, which contributed to strong downward motion. The magnitudes of the divergence and vertical velocities calculated from dual-Doppler data were 2-3 times stronger in the Brandes and Ziegler study compared to those found in this study. The vertical vorticity profile in Brandes and Ziegler was also quite similar, with the maximum vorticity near the melting level. However, the magnitudes of the average vorticity in their study were nearly an order of magnitude smaller that those found in this case. Their analysis of the vorticity tendency had a distinctly different profile. The tilting term dominated the stretching term and the peak vorticity production occurred at higher levels (6.5 km) than in this case. The peak amplification rates in Brandes and Ziegler (1993) were also about 3-4 times smaller than those found in this study.

Jorgensen and Smull (1993) analyzed an MCV using airborne-Doppler radar data. The vortex in their study was shallower (~5 km) and weaker than the 28 May 1985 case. The peak relative vertical vorticity, again found near the melting level, was on the order of 3×10^{-4} s^{-1}. The flow within the vortex was again convergent and downward. The amplification rates of the vortex were found to be an order of magnitude smaller than in this study.

Several cases involving both convergent and downward air motion within MCVs, as well as peak rotation rates near the melting level have now been documented. These findings correspond well with theories developed from numerical simulations that suggest mesolows near the melting level, as well as tilting of horizontal vorticity into the vertical by mesoscale downward motion and subsequent stretching of the resultant vertical vorticity by convergence, are responsible for the strong low- and mid-level rotation found in the stratiform regions of MCSs. The presence of a mid-level pressure minimum within the mature MCV is verified by the following analysis.

Chapter 6

PRESSURE RETRIEVAL

6.1 Motivation

Previous observational studies of MCVs have diagnosed areas of low pressure associated with these features using upper-air sounding networks (e.g., Gallus and Johnson 1992, Smull and Augustine 1993, Menard and Fritsch 1989). Other studies using upper air data (Bartels and Maddox 1991, Brandes 1990) have shown that the mesoscale environment of the MCV is cold core below the melting level and warm core above the melting level. This can be viewed as a low pressure perturbation at mid-levels (LeMone 1984). Dual-Doppler data has also been used to diagnose areas of low pressure in MCV circulations (Matejka 1989). Extensive studies of MCCs (Maddox 1983, Cotton *et al.* 1989) have shown that the diabatic processes within these convective systems have a tendency to amplify pre-existing mid-level short-waves. This can also be viewed as a hydrostatic lowering of pressure at mid-levels. It is unclear whether the pre-existing mid-level pressure perturbations associated with the large scale environment were necessary for the MCCs to amplify the mid-level pressure perturbations and vorticity fields in these cases. Recent modeling studies (Weisman 1992, Davis and Weisman 1994, Skamarock *et al.* 1994) have shown that long-lived convective systems can generate low pressure at mid-levels, contributing to a balanced circulation, in the absence of large scale forcing. Since the MCS described in this thesis developed under a weak ridge at 500 mb, with weak vorticity advection (see Ch. 3), it was desirable to find out whether the strong cyclonic circulation that developed in the northern portion of the trailing stratiform region was associated with lower pressure. Since there were no supplemental soundings available for this case, it seemed that a pressure retrieval using the dual-Doppler derived winds would be the only way to confirm the existence of lower pressure in the MCV.

6.2 Methodology

The 3-D wind fields derived from dual-Doppler analysis provide the detail necessary for the retrieval of relative pressure perturbations through the manipulation of the equation of motion and the equation of state. This methodology for thermodynamic retrieval was first proposed by Gal-Chen (1978) and later refined by Gal-Chen and Hane (1981), Roux *et al.* (1984), Roux (1985) and Matejka (1989). It is convenient to formulate the retrieval in terms of the Exner function (π) and virtual potential temperature (θ_v).

The equation of state is:

$$p\alpha = R_d T_v \qquad (6.1),$$

where

p = pressure
α = specific volume
R_d = specific gas constant of dry air
T_v = virtual temperature.

The Exner function is defined as

$$\pi = \left(\frac{p}{p_{00}}\right)^{R_d/c_p} \qquad (6.2),$$

where

p_{00} = reference pressure, 10^5 Pa.

$C_p =$ specific heat at constant pressure of dry air.

Virtual potential temperature is defined as

$$\theta_v = T_v \left(\frac{p_{00}}{p} \right)^{R_d/C_p} \tag{6.3}$$

Additional relationships follow from equations 6.1-6.3.

$$p = p_{00}\, \pi^{C_p/R_d} \tag{6.4}$$

$$\alpha = \frac{\mathrm{R_d}\, \theta_v}{p_{00}\, \pi^{(C_p/R_d)-1}} \tag{6.5}$$

Any variable Q can be expressed in terms of a reference state (Q_0) and a departure from that reference state (Q'):

$$\mathrm{Q} = \mathrm{Q}_0 + \mathrm{Q}' \tag{6.6}$$

where the reference state (Q_0) is defined to be at most a function of z. This declaration will be used to simplify the equations of motion in the derivation that follows. The x-component of the momentum equation is defined as:

$$\frac{Du}{Dt} = -\alpha \frac{\partial p}{\partial x} + 2v\, \Omega \sin\varphi - 2w\, \Omega \cos\varphi + F_x \tag{6.7}$$

where

$$\frac{D}{Dt} = \frac{\partial}{\partial t} + u\frac{\partial}{\partial x} + v\frac{\partial}{\partial y} + w\frac{\partial}{\partial z}$$

$\Omega =$ angular velocity of the Earth's rotation

$\varphi =$ latitude

$F_x =$ the x - component of dissipation forces and apparent forces from unresolved turbulent mixing.

Equations (6.4) and (6.5) can be used to write

$$\alpha \frac{\partial p}{\partial x} = \left(\frac{R_d \theta_v}{p_{00} \pi^{(C_p/R_d)-1}} \right) \left(\frac{p_{00} C_p \pi^{(C_p/R_d)-1}}{R_d} \frac{\partial \pi}{\partial x} \right)$$
$$= C_p \theta_v \frac{\partial \pi}{\partial x} \quad .$$

This equation can be expanded about a reference state using (6.6).

$$\begin{aligned} \alpha \frac{\partial p}{\partial x} &= C_p \left(\theta_{v0} + \theta_v' \right) \frac{\partial}{\partial x} \left(\pi_0 + \pi' \right) \\ &= C_p \theta_{v0} \left(1 + \frac{\theta_v'}{\theta_{v0}} \right) \frac{\partial}{\partial x} \left(\pi_0 + \pi' \right) \end{aligned} \qquad (6.8).$$

Using (6.8) and $\frac{\partial \pi_0}{\partial x} = 0$, equation (6.7) becomes:

$$\frac{Du}{Dt} = -C_p \theta_{v0} \left(1 + \frac{\theta_v'}{\theta_{v0}} \right) \frac{\partial \pi'}{\partial x} + 2v\,\Omega \sin \varphi - 2w\,\Omega \cos \varphi + F_x \qquad (6.9).$$

If θ_{v0} is defined such that $\theta_v' << \theta_{v0}$, equation (6.9) can be rewritten as:

$$\frac{Du}{Dt} = -C_p \theta_{v0} \frac{\partial \pi'}{\partial x} + 2v\,\Omega \sin \varphi - 2w\,\Omega \cos \varphi + F_x \qquad (6.10).$$

Now, if G_x is defined as:

$$G_x \equiv \frac{1}{C_p \theta_{v0}} \left(-\frac{Du}{Dt} + 2v\,\Omega \sin \varphi - 2w\,\Omega \cos \varphi + F_x \right) \qquad (6.11),$$

then

$$\frac{\partial \pi'}{\partial x} = G_x \qquad (6.12).$$

The same transformation can be applied to the y-component of the momentum equation:

$$\frac{Dv}{Dt} = -\alpha \frac{\partial p}{\partial y} - 2u\,\Omega \sin \varphi + F_y \qquad (6.13),$$

where

F_y = the y - component of dissipation forces and apparent forces from unresolved turbulent mixing.

Equations (6.4) and (6.5) can be used to write

$$\alpha \frac{\partial p}{\partial y} = \left(\frac{R_d \theta_v}{p_{00} \pi^{(C_p/R_d)-1}} \right) \left(\frac{p_{00} C_p \pi^{(C_p/R_d)-1}}{R_d} \frac{\partial \pi}{\partial y} \right)$$
$$= C_p \theta_v \frac{\partial \pi}{\partial y} \quad .$$

This equation can be expanded about a reference state using (6.6).

$$\begin{aligned} \alpha \frac{\partial p}{\partial y} &= C_p (\theta_{v0} + \theta'_v) \frac{\partial}{\partial y} (\pi_0 + \pi') \\ &= C_p \theta_{v0} \left(1 + \frac{\theta'_v}{\theta_{v0}} \right) \frac{\partial}{\partial y} (\pi_0 + \pi') \end{aligned} \qquad (6.14).$$

Using (6.14) and $\frac{\partial \pi_0}{\partial y} = 0$, equation (6.13) becomes:

$$\frac{Dv}{Dt} = -C_p \theta_{v0} \left(1 + \frac{\theta'_v}{\theta_{v0}} \right) \frac{\partial \pi'}{\partial y} - 2u\, \Omega \sin \varphi + F_y \qquad (6.15).$$

If θ_{v0} is defined such that $\theta'_v << \theta_{v0}$, equation (6.15) can be rewritten as:

$$\frac{Dv}{Dt} = -C_p \theta_{v0} \frac{\partial \pi'}{\partial y} - 2u\, \Omega \sin \varphi + F_y \qquad (6.16)$$

Now, if G_y is defined as:

$$G_y \equiv \frac{1}{C_p \theta_{v0}} \left(-\frac{Dv}{Dt} - 2u\, \Omega \sin \varphi + F_y \right) \qquad (6.17),$$

then

$$\frac{\partial \pi'}{\partial y} = G_y \qquad (6.18).$$

Now we can solve for the horizontal perturbations of π. Define

$$\pi' \equiv \bar{\pi}' + \hat{\pi}' \tag{6.19}$$

where $\bar{\pi}'$ is defined to be an arbitrary function of z and t only. Therefore (6.12) and (6.18) contain no information on $\bar{\pi}'$, since

$$\begin{aligned} G_x &= \frac{\partial \pi'}{\partial x} \\ &= \frac{\partial \bar{\pi}'}{\partial x} + \frac{\partial \hat{\pi}'}{\partial x} \\ &= \frac{\partial \hat{\pi}'}{\partial x} \end{aligned} \tag{6.20}$$

$$\begin{aligned} G_y &= \frac{\partial \pi'}{\partial y} \\ &= \frac{\partial \bar{\pi}'}{\partial y} + \frac{\partial \hat{\pi}'}{\partial y} \\ &= \frac{\partial \hat{\pi}'}{\partial y} \end{aligned} \tag{6.21}$$

Equations (6.20) and (6.21) can be solved for $\hat{\pi}'$ at specific values of z and t, but $\bar{\pi}'$ will remain unknown.. In other words, (6.12) and (6.18) can be solved for π' to within an arbitrary function of z and t. At a specific z and t, (6.20) and (6.21) can be solved for $\hat{\pi}'$ by minimizing the functional

$$J_\pi = \sum_i \sum_j \left[\left(\frac{\partial \hat{\pi}'}{\partial x_{ij}} - G_{x_{ij}} \right)^2 + \left(\frac{\partial \hat{\pi}'}{\partial y_{ij}} - G_{y_{ij}} \right)^2 \right] + \lambda \sum_i \sum_j \hat{\pi}' \tag{6.22}$$

with respect to all the $\hat{\pi}'_{ij}$. Here the summation over i and j indicate summation over all grid points (i, j) in the (x, y) plane. A Lagrange multiplier is represented by λ, and the last term is used to complete the set of equations by requiring, without loss of generality, that the sum of $\hat{\pi}'$ on the (x, y) plane is zero. Any offset could have been used, since the offset is absorbed into the unknown $\bar{\pi}'$.

The retrieved values of $\hat{\pi}'$ are horizontal perturbations of π from unknown reference values of $\pi_0 + \tilde{\pi}'$. These unknown reference values are, in general, different for different heights and times. Therefore it is only meaningful to compare values of $\hat{\pi}'$ at particular times on particular horizontal planes. The non-dimensional horizontal perturbations of the Exner function ($\hat{\pi}'$) can be transformed into dimensional perturbations in the pressure field ($\hat{p}'$) by way of the following transformation.

$$p = p_{00}\,\pi^{C_p/R_d} \tag{6.4}$$

Now we expand (6.4) into reference and perturbations states:

$$\begin{aligned} p_0 + \tilde{p}' + \hat{p}' &= p_{00}\left(\pi_0 + \tilde{\pi}' + \hat{\pi}'\right)^{C_p/R_d} \\ &= p_{00}\,\pi_0^{C_p/R_d}\left(1 + \frac{\tilde{\pi}'}{\pi_0} + \frac{\hat{\pi}'}{\pi_0}\right)^{C_p/R_d} \end{aligned} \tag{6.23}$$

Similarly, (6.4) can be expanded in this manner:

$$\begin{aligned} p_0 + \tilde{p}' &= p_{00}\left(\pi_0 + \tilde{\pi}'\right)^{C_p/R_d} \\ &= p_{00}\,\pi_0^{C_p/R_d}\left(1 + \frac{\tilde{\pi}'}{\pi_0}\right)^{C_p/R_d} \end{aligned} \tag{6.24}$$

Equation (6.24) can now be used to eliminate $p_0 + \tilde{p}'$ from equation (6.23).

$$\hat{p}' = p_{00}\,\pi_0^{C_p/R_d}\left[\left(1 + \frac{\tilde{\pi}'}{\pi_0} + \frac{\hat{\pi}'}{\pi_0}\right)^{C_p/R_d} - \left(1 + \frac{\tilde{\pi}'}{\pi_0}\right)^{C_p/R_d}\right] \tag{6.25}$$

If $\frac{\tilde{\pi}'}{\pi_0}$ <<1 and $\frac{\hat{\pi}'}{\pi_0}$ <<1, then (6.25) can be simplified using the first two terms of a binomial series expansion: $(1+x)^m = 1 + mx + \frac{m(m-1)x^2}{2!} + \ldots$ The third and higher order terms can be neglected since in the case of (6.25), $x \ll 1$. Thus (6.25) becomes:

$$\hat{p}' \approx p_{00}\pi_0^{C_p/R_d}\left(1+\frac{C_p}{R_d}\frac{\tilde{\pi}'}{\pi_0}+\frac{C_p}{R_d}\frac{\hat{\pi}'}{\pi_0}-1-\frac{C_p}{R_d}\frac{\tilde{\pi}'}{\pi_0}\right)$$

$$= p_{00}\pi_0^{C_p/R_d}\left(\frac{C_p}{R_d}\frac{\hat{\pi}'}{\pi_0}\right) \qquad (6.26).$$

$$\hat{p}' \approx \frac{p_{00}\pi_0^{(C_p/R_d)-1}C_p\hat{\pi}'}{R_d}$$

The above retrieval equations were applied to three dual-Doppler analysis times separated by 11 minutes, centered at 1314 UTC, using CEDRIC (Mohr and Miller 1983). In order to minimize errors associated with finite differencing, the three radar volumes were advected to a storm-relative coordinate system. In other words, the Cartesian grid was set up in such a way that each grid point remains in the same location relative to the storm at all three analysis times. Storm motion was also subtracted from the velocity fields before application of the equations. The total derivatives and Coriolis terms in (6.11) and (6.17) were calculated using the input radar data. The vertical profile of the base state virtual potential temperature (θ_{vo}) was estimated from the 12 UTC OKC sounding (Fig. 3.2). Actually, any profile of (θ_{vo}) could have been used as long as the requirement of $\theta_v' << \theta_{vo}$ was satisfied. Parameterization of the dissipation forces ($F_{x,y}$) was not attempted, because of the possibility of introducing uncertainties to the retrieval (T. Matejka, personal communication). Therefore, the dissipation forces were assumed to be small and were left out of the calculations. Equation (5.4) was then solved for using a CEDRIC function specifically designed for thermodynamic retrieval. The resulting horizontal perturbations of the Exner function ($\hat{\pi}'$) were then converted to horizontal perturbations of pressure ($\hat{p}'$) using (6.26).

6.3 Results

At z=2.9 km (Fig. 6.1a,b), it is apparent that a low pressure perturbation was coincident with the strong cyclonic circulation in the northern portion of the stratiform region. In fact, the minimum in the horizontal pressure perturbation (-1.4 mb) was directly in the center of the dual-Doppler derived circulation, with the flow rotating around the pressure minimum, suggesting the presence of gradient balance in the flow. The retrieval at 3.9 km (Fig. 6.2a,b) also depicts a strong low pressure perturbation (-1.5 mb) coincident with the vortex circulation center. Both analyses also show the strongest pressure gradient on the western side of the vortex. As was shown in Ch. 4 and 5, this was a region of strong convergence between the rear inflow jet and the vortex circulation. It appears that this intense pressure gradient was aiding in the acceleration of the rear inflow jet on the western edge of the storm. The resulting convergence contributed to the spin-up of the MCV circulation through the process of vortex stretching.

Observations of low pressure minima in vicinity of MCV circulations have been reported in previous studies (e.g., Matejka 1989, Gallus and Johnson 1992, Smull and Augustine 1993). Gallus and Johnson (1992) found a closed low in the northern portion of the trailing stratiform region of a linear squall line system using the PRE-STORM rawinsonde network. They attributed the mid-level meso-low to latent heating in the upper levels of the anvil cloud and latent cooling within the stratiform rain below cloud base. Their findings were consistent with the pressure retrieval performed on the radar-derived wind fields of the same MCS (Matejka 1989). Smull and Augustine (1993) also diagnosed a pressure minimum in the trailing stratiform region of an MCS containing a mesovortex, yet the pressure minimum in this case was not collocated with the positive vorticity center. This may be explained by the fact that the vortex in that case was primarily composed of cyclonic shear instead of a closed circulation (at least in the early stage of its life-cycle).

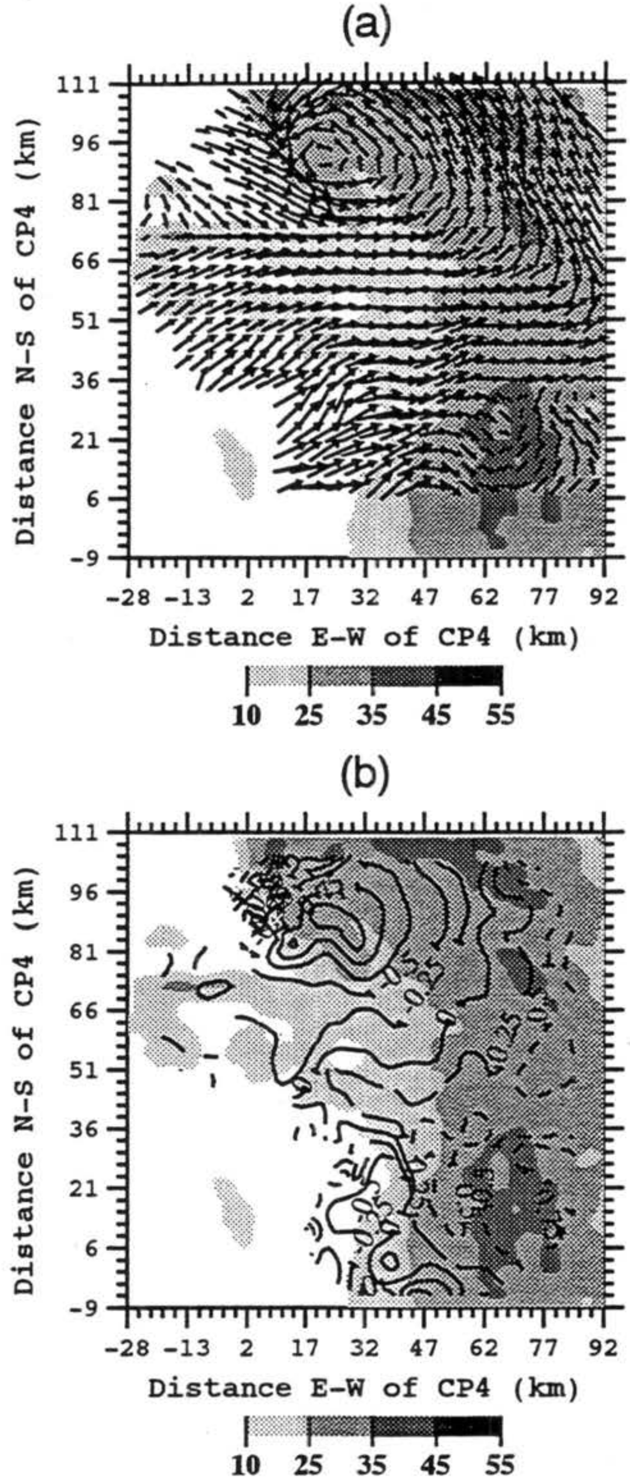

Figure 6.1: Horizontal cross-section of reflectivity (dBZ; gray shading) at z=2.9 km from the 1314 UTC dual-Doppler analysis and: (a) storm relative wind vectors (ms^{-1}; wind vectors 4.5 km long indicate a $20ms^{-1}$ wind); (b) retrieved horizontal pressure perturbations (mb, solid contours indicate negative perturbations, short dash contours indicate positive perturbation, contour increment is 0.25 mb).

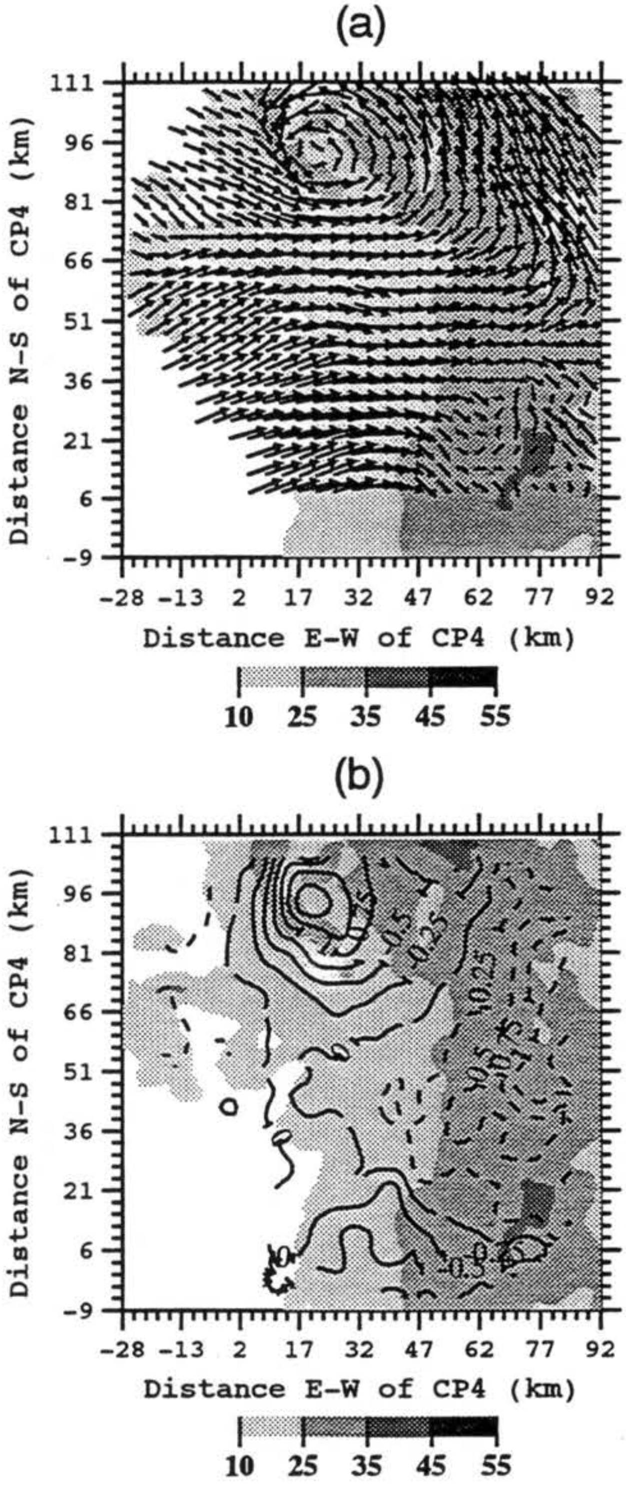

Figure 6.2: Horizontal cross-section of reflectivity (dBZ; gray shading) at z=3.9 km from the 1314 UTC dual-Doppler analysis and: (a) storm relative wind vectors (ms^{-1}; wind vectors 4.5 km long indicate a $20ms^{-1}$ wind); (b) retrieved horizontal pressure perturbations (mb, solid contours indicate negative perturbations, short dash contours indicate positive perturbation, contour increment is 0.25 mb).

In simulations of long-lived bow echoes, Weisman (1993) found low pressure centers collocated with counter-rotating "bookend" circulations (Fig. 6.3). A decomposition of the pressure field revealed that vertical gradients in buoyancy dominated the pressure term, yet a dynamic reduction of pressure became significant in the vicinity of the "bookend" vortex. The dynamic reduction in pressure was attributed to "the strong curvature in the flow field". It seems likely that the low pressure perturbation within the mature MCV in the 28 May case had contributions from both the buoyancy and dynamic terms as well. In simulations including Coriolis effects, Skamarock *et al.* (1994) show results that are strikingly similar to the pressure retrieval in this thesis (Fig 6.4). The minimum pressure perturbation is situated in the center of the northern portion of the trailing stratiform region and is associated with a positive buoyancy perturbation. Notice the asymmetric organization of the buoyancy field is quite similar to the asymmetry in the reflectivity fields shown in Ch. 4. The storm relative circulation center (Fig. 6.5) is also collocated with the low pressure perturbation. The low pressure within the vortex is in part due to the positively buoyant convective outflow being advected northward by the system relative flow at 8.9 km (Fig. 6.6). The strongest convection was about 100 km south of this cross-section at this time (Fig. 4.3b). The system relative FTR flow was deflected northward by the Coriolis effect over time. The upper-air analyses (Ch. 3) confirm that there was no pre-existing line-parallel flow in the environment. Therefore, the southerly line parallel flow in Fig 6.6 was solely a result of the Coriolis effects on the system generated mesoscale flow.

6.4 Error analysis

Errors associated with pressure retrieval have usually been estimated by the "momentum checking" parameter introduced by Gal-Chen and Hane (1981). This parameter (*Err*) calculates the standard deviation between the input data (G_x , G_y) and the retrieved gradients $\left(\dfrac{\partial \hat{\pi}'}{\partial x}, \dfrac{\partial \hat{\pi}'}{\partial y}\right)$ from equation (6.22). *Err* is defined by

$$Err = \frac{\iint\limits_{D(z)} \left[\left(\frac{\partial \hat{\pi}'}{\partial x} - G_x \right)^2 + \left(\frac{\partial \hat{\pi}'}{\partial y} - G_y \right)^2 \right] dxdy}{\iint\limits_{D(z)} \left[G_x^2 + G_y^2 \right] dxdy}$$

(6.27),where D(z) is the horizontal domain at each altitude (z). *Err* is proportional to the relative statistical errors in the input and output fields at each altitude (z). Numerical tests using "idealized" data have shown that the "critical" value of *Err* is 0.50 (Gal-Chen and Hane 1981), meaning reliable results should have values of *Err* < 0.50. Roux *et al.* (1984) found the reliable range of *Err* to be 0.10-0.60. In dual-Doppler observations of the planetary boundary layer, Gal-Chen and Kropfli (1983) found typical values of *Err* to be 0.35. The results of the momentum checking for this study are shown in Fig. 6.7. All calculations of *Err* fall between 0.18 and 0.51. The levels that in which the vortex circulation was strongest (1.4-5.4 km) had a range of *Err* from 0.21-0.35, which is well within the acceptable range defined by Gal-Chen and Hane (1981) as well as Roux *et al.* (1984).

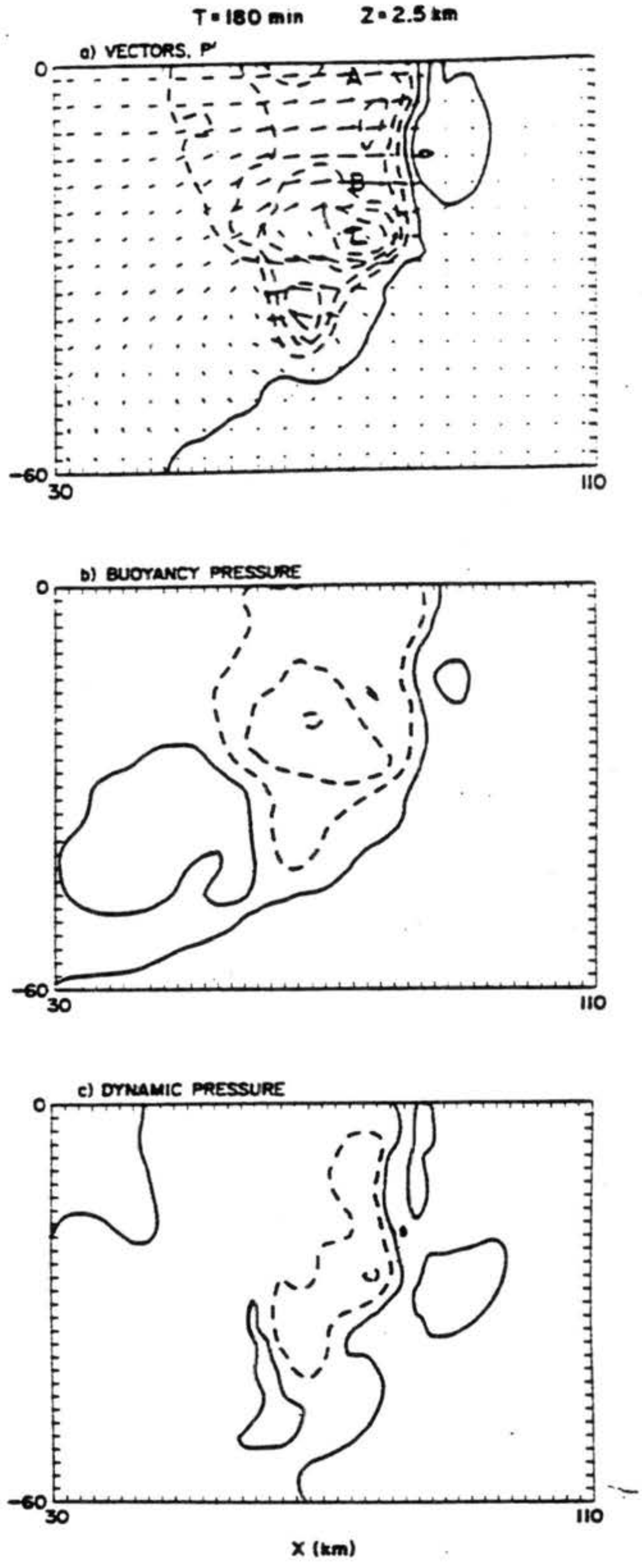

Figure 6.3: Horizontal cross section at 2.5 km of (a) pressure perturbations and flow vectors, (b) buoyancy contributions to the pressure field and (c) dynamic contributions to the pressure field at 3 hr into bow echo simulation. Pressure is contoured every 0.5 mb. (from Weisman 1993).

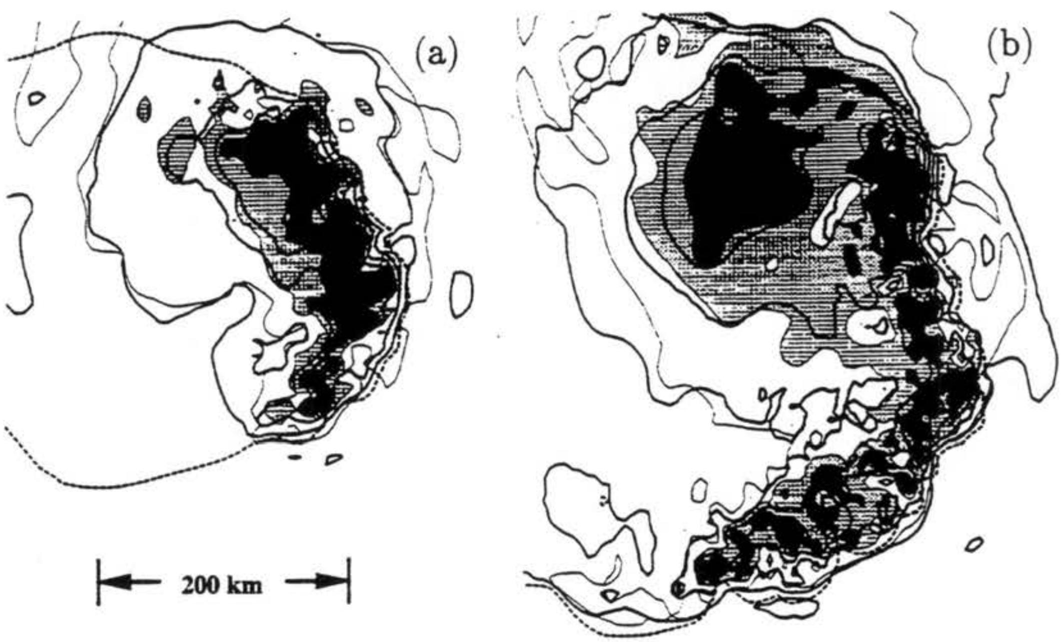

Figure 6.4: Buoyancy at 5.6 km and perturbation pressure at 3 km at (a) 6 hr and (b) 10 hr in the Coriolis simulation. Pressure contoured every 0.4 mb. Buoyancy stippled from light to dark at 300, 500, and 700 ms^{-2} in (a) and 500, 700 and 900 ms^{-2} in (b). (from Skamarock *et al.* 1994).

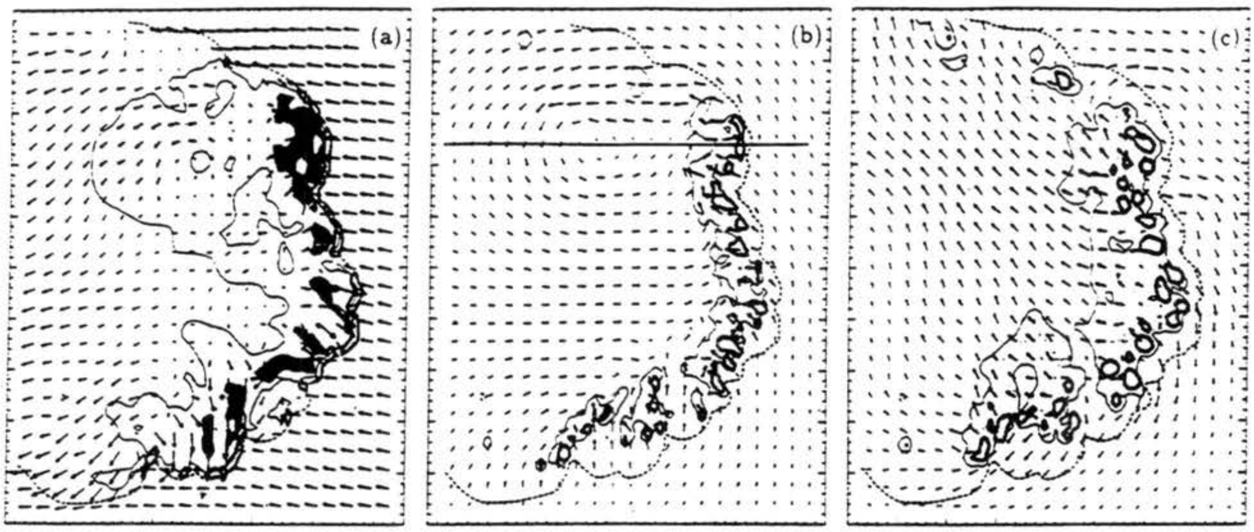

Figure 6.5: As in figure 1.5, except 10 hours into simulation (from Skamarock *et al.* 1994).

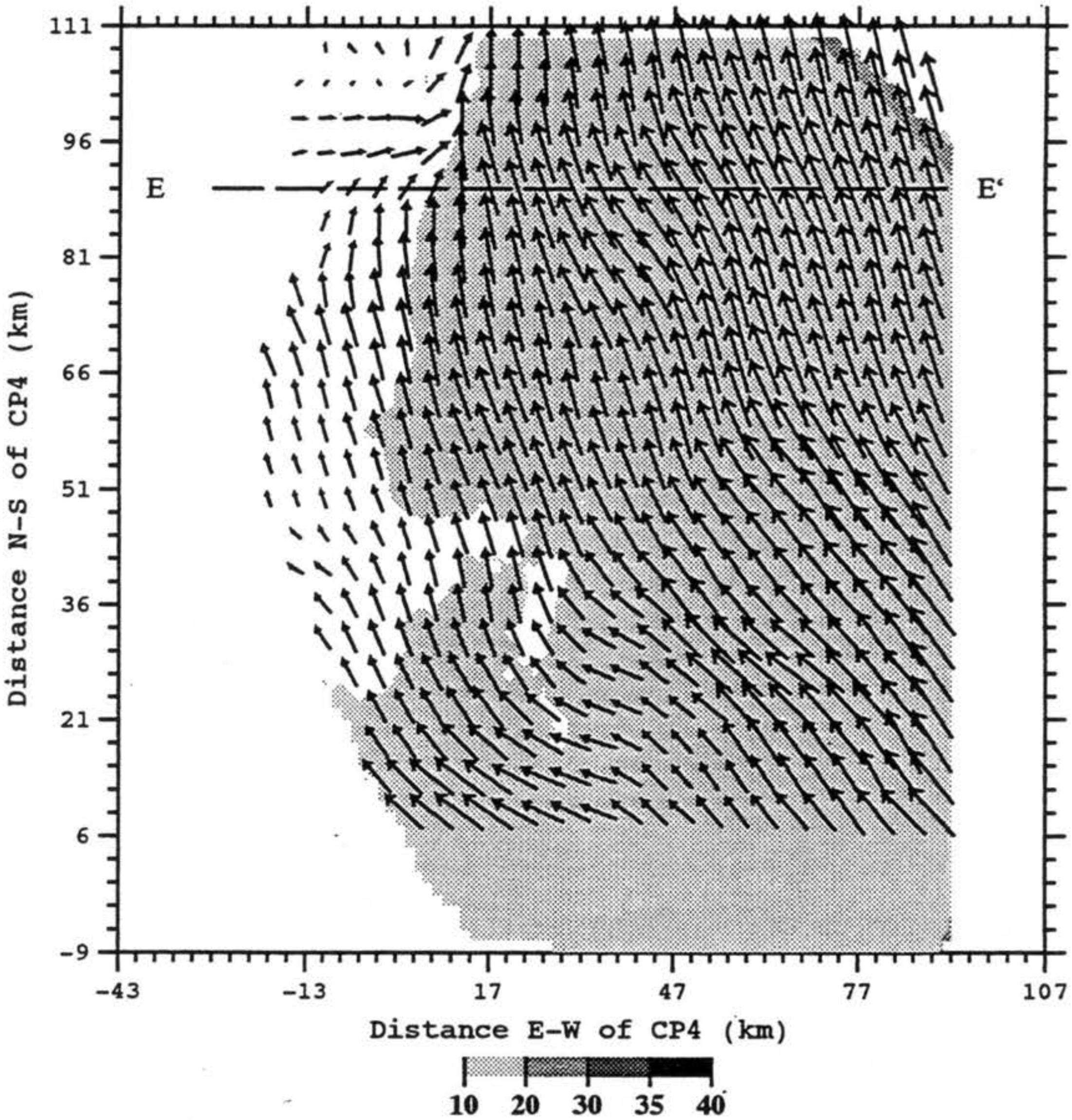

Figure 6.6: Same as 4.15, except for at 8.9 km.

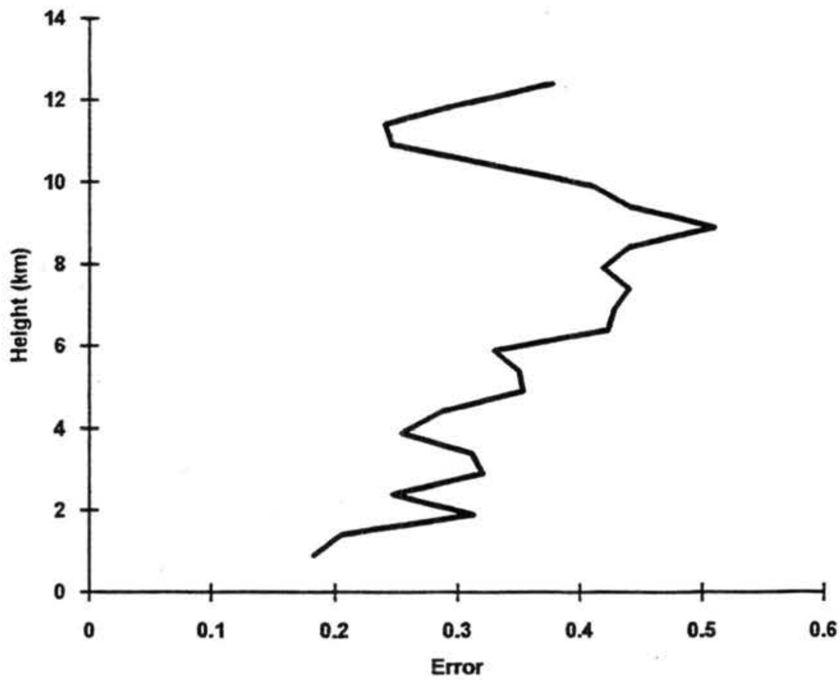

Figure 6.7: Vertical profile of the momentum checking parameter for the 1314 UTC pressure retrieval.

Chapter 7

CONCLUSIONS

7.1 Summary

The topic of MCV genesis and maintenance has been the subject of many investigations. The data collected during PRE-STORM have greatly increased our understanding of these mesoscale features, yet proof of the mechanisms involved in the generation and maintenance of these circulations has remained elusive. Some of the earlier numerical and observational studies of MCVs suggested that these circulations developed in the ascending FTR flow of MCSs and were considered "warm core" (Bosart and Sanders 1981, Zhang and Fritsch 1987, 1988, Menard and Fritsch 1989). More recent studies have shown that MCVs can also be generated in the relatively cool, descending RTF flow (Zhang 1992, Brandes and Ziegler 1993, Jorgensen and Smull 1993). Hertenstein and Schubert (1991) showed that the bipolar nature of stratiform latent heating profiles can lead to mid-level potential vorticity anomalies and cyclonic rotation. Thus the heating due to condensation in the mesoscale updraft and the cooling resulting from melting and evaporation in the mesoscale downdraft are both responsible for the generation of mid-level cyclonic rotation. The above studies, however, did not address the formation of anticyclonic rotation in stratiform regions of MCSs.

Studies by Weisman (1993), Skamarock *et al.* (1994) and Davis and Weisman (1994) propose mechanisms for the formation of counter-rotating cyclonic and anticyclonic circulations in MCSs, which are substantiated by this observational study.

These studies show that the CAPE and low-level wind shear are the most crucial factors in developing an MCS with counter-rotating vortices. An environment with high CAPE and weak to moderate wind shear in the lowest 2-5 km is essential for the development of convection that begins to tilt upshear with time (Rotunno *et al.* 1988, Weisman 1992). The ambient vertical wind shear initially causes a downshear tilt to the convection. As the convective outflow or cold pool develops, a wind shear opposite to that of the environment is found at the leading edge of the cold pool, where the strong horizontal buoyancy gradient generates horizontal vorticity. When this horizontal vorticity is equal and opposite to that of the environment, lifting is enhanced and the convection becomes more upright. The resulting stronger convection strengthens the cold pool, which eventually overwhelms the ambient shear, causing the convection to begin to tilt rearward over the cold pool. The upshear tilting of the system marks the onset of the mesoscale FTR flow and the development of a stratiform precipitating region. Latent heat release due to deposition and condensation in the ascending FTR flow creates a positive buoyancy anomaly aloft, which can be viewed hydrostatically as a pressure minimum at mid-levels (LeMone 1983, LeMone *et al.* 1984). The resulting horizontal pressure gradient at mid-levels on the back edge of the stratiform cloud initiates the acceleration of the RTF flow into the MCS (Smull and Houze, 1987). As drier air is entrained into the precipitating cloud, evaporation and sublimation create negative buoyancy and downward motion in the RTF flow. Rear inflow is maximized at mid-levels (usually near the melting level), where the mid-level mesolow is strongest, creating a westerly (RTF) speed maximum. This augments the low-level westerly shear in the ambient flow, creating horizontal vorticity that is positive in the northerly direction by the right-hand rule. Tilting of the horizontal vorticity into the vertical by meridional gradients in the mesoscale descent associated with the RTF flow creates a vorticity couplet that is cyclonic to the north and anticyclonic to the south. Convergence at the interface of the FTR and RTF flows subsequently enhances these counter-rotating circulations through the process of vortex stretching. These mid-level vorticity features also produce a dynamic response in the pressure field as shown in Rotunno and Klemp (1982) and Weisman (1992). For rotational flow, it is shown that pressure is proportional to the negative of the vertical vorticity squared. Thus, vorticity of either sign dynamically reduces the pressure within each vortex, which can lead to a quasi-gradient balance. Simulations of MCVs by Davis and Weisman (1994) have shown through a potential vorticity analysis that these circulations are primarily balanced flows. They also emphasize that the formation of the balanced vortex circulations hinge upon the fundamentally unbalanced processes that lead to the FTR and RTF flows.

The effects of the Earth's rotation on the evolution of MCV circulations have been explored by Skamarock *et al.* (1994). They found that for long-lived squall lines, the effects of the Coriolis force become important after about 6 hours of simulated time. Specifically, the positive buoyancy anomaly in the FTR flow is deflected to the north and the cold pool associated with the RTF flow is deflected to the south. The northern cyclonic vortex is enhanced by the lowering of the mid-level pressure as the positive buoyancy anomaly shifts northward. Both vortex stretching and a quasi-balanced response may enhance the circulation as the mid-level pressure drops. At the same time the northern vortex is spinning up, the southern vortex begins to spin down as the mid-level pressures increase due to the northward shift of the positive buoyancy anomaly. The superposition of the Earth's vorticity on the vortex circulations is also attributed to the dominance of the northern cyclonic vortex and the demise of the southern anticyclonic vortex.

Radar analysis documented the evolution of this convective system from a linear squall line, to a squall line with a trailing stratiform region (symmetric MCS), to an asymmetric MCS with a broad stratiform region to the north and stronger convection to the south. Recent modeling studies suggest that this is the typical life-cycle of long-lived convective systems in the absence of large scale forcing. This asymmetry in the radar echo pattern became strongly evident as the cyclonic circulation intensified, advecting hydrometeors from decaying convection northward and westward, and advecting drier environmental air from the rear of the system southward and eastward. The depth (~7 km) and intensity (>4×10^{-3} s^{-1}) of the MCV created a distinct hook-like appendage in the reflectivity field during the mature stage of the MCS. This leads to the question of how and why the MCV began to dominate the mesoscale flow characteristics of this MCS. The dual-Doppler analysis hints at some mechanisms that would feed back on each other, promoting the rapid growth of the circulation.

The presence of a strong and deep rear inflow jet appears instrumental in the maintenance and intensification of the MCV. First, the rear inflow jet provided mid- and upper-level convergence as it collided with the system relative FTR flow. Second, the rear inflow advected drier air into the system, producing negative buoyancy through the processes of sublimation, melting and evaporation. Both the mid- and upper-level convergence and negative buoyancy effects lead to strong downward motion and perhaps more importantly, strong gradients in vertical velocity at the back edge of the stratiform cloud. Third, the rear inflow jet had a maximum westerly velocity of 15 ms^{-1} near the melting level (3.9 km), which created strong westerly shear below this level, augmenting the ambient shear. The horizontal vorticity created by the rear inflow jet and the ambient flow could then be tilted into the vertical by the strong gradients in vertical velocity. The areal averaged vorticity tendencies showed that stretching contributed to positive vorticity at the same levels where the rear inflow jet was present, and was maximized just above the melting level (where the rear inflow was strongest). Furthermore, the closed circulation was only evident at levels where rear inflow was present. Thus it appears that the presence of the rear inflow jet was instrumental in the maintenance and amplification of the vortex circulation in this particular case.

It has been stated earlier that the rear inflow jet is believed be a dynamic response to the mid-level pressure gradients induced by positive buoyancy anomalies aloft in the mesoscale FTR flow (Smull and Houze, 1987). It has also been suggested that the rear inflow jet may produce vertical vorticity through the above mechanisms. The presence of the rotation itself can act to lower the pressure, which would intensify the mid-level mesolow and accelerate the rear inflow jet. The stronger stretching and tilting of vorticity by the rear inflow jet would contribute positively to the lower pressure at mid-levels. Lower pressure could also intensify the circulation by way of a quasi-balanced response. The retrieved horizontal pressure perturbations confirm that lower pressure existed at mid-levels, coincident with the cyclonic vortex circulation. The rotation of the flow around the pressure minimum suggests the presence of a quasi-gradient balance. The strong pressure gradient on the western side of the vortex also accelerated the rear inflow, which generated convergence and subsequently enhanced the cyclonic vorticity through vortex stretching. This is how rapid amplification of the MCV could occur.

The hypothesis on the rapid intensification of the cyclonic vortex and the destruction of the anticyclonic vortex in this case was based on observations which correspond well with theories developed in numerical modeling studies. Unfortunately the dual-Doppler data were not available during the period in which the cyclonic vortex was intensifying (1148 UTC-1303 UTC), as other scanning strategies were being followed during this time period. Thus the above hypothesis cannot be uniquely proven with this data set. Ideally, dual-Doppler and supporting thermodynamic data throughout the developing, mature and dissipating stages of an MCS would be needed to identify all the mechanisms involved in the generation and maintenance of the counter-rotating circulations found in long-lived convective systems. However, the inherent nature of these systems makes them very difficult to observe (system lifetimes exceed 10-12 hours).

7.2 Suggestions for future research

Observations of MCVs during their formative stages are still quite lacking. Since the details of the mechanisms involved in the genesis of these circulations are limited at best, it would seem that dual-Doppler and mesoscale upper-air observations of the development of rotation in MCSs is essential to further our understanding of these features. Of course, this is no simple task. It would take a research effort on the scale of PRE-STORM and a little luck. Hopefully, the research done in this thesis and in other published works would be able to focus such an effort. Airborne Doppler radars may be best suited for documenting the initiation and evolution of MCV circulations, because of their mobility. Specifically, the following questions regarding MCV genesis need to be answered. Does the rear inflow jet develop before or after the development of the MCV and how are the processes involved with the two features related?. Do all symmetric MCSs that evolve into asymmetric MCSs begin with counter-rotating "bookend" vortices, in which the cyclonic vortex later dominates? How frequently is this evolution observed? Is it the tilting of horizontal vorticity into the vertical or is it a balanced response to the vertical gradients in buoyancy that initially produces these circulations? In lieu of further observational evidence, numerical simulations will continue to provide high resolution data to develop theories for the evolution of circulations within MCSs. These numerically derived theories should then be validated by observations whenever possible.

REFERENCES:

Barnes, S. L., 1964: A technique for maximizing details in numerical weather map analysis. *J. Appl. Meteor.*, **3**, 396-409.

Bartels, D. L., and R. A. Maddox, 1991: Midlevel cyclonic vortices generated by mesoscale convective systems. *Mon. Wea. Rev.*, **119**, 3034-3065.

Biggerstaff, M. I., and R. A. Houze, 1991: Midlevel vorticity structure of the 10-11 June 1985 squall line. *Mon. Wea. Rev.*, **119**, 3066-3079.

Bosart, L. F., and F. Sanders, 1981: The Johnstown flood of July 1977: A long-lived convective storm. *J. Atmos. Sci.*, **38**, 1616-1642.

Brandes, E. A., 1990: Evolution and structure of the 6-7 May 1985 mesoscale convective system and associated vortex. *Mon. Wea. Rev.*, **118**, 109-127.

______, and C. L. Ziegler, 1993: Mesoscale downdraft influences on vertical vorticity in a mature mesoscale convective system. *Mon. Wea. Rev.*, **121**, 1337-1353.

Brown, J. M., 1979: Mesoscale unsaturated downdrafts driven by rainfall evaporation. *J. Atmos. Sci.*, **36**, 313-338.

Chen, S., and W. R. Cotton, 1988: The simulation of a mesoscale convective system and its sensitivity to physical parameterizations. *J. Atmos. Sci.*, **45**, 3897-3910.

Cotton, W. R., M. S. Lin, R. L. McAnelly and C. J. Tremback, 1989: A composite model of mesoscale convective complexes. *Mon. Wea. Rev*, **117**, 765-783.

Cressman, G. P., 1959: An operational objective analysis system. *Mon. Wea. Rev.*, **87**, 367-374.

Cunning, J. B., 1986: The Oklahoma-Kansas preliminary regional experiment for STORM-Central. *Bull. Amer. Meteor. Soc.*, **67**, 1478-1486.

Davis, C. A., and M. L. Weisman. 1994: Balanced dynamics of mesoscale vortices produced in simulated convective systems., *J. Atmos. Sci.*, **51**, 2005-2030.

Fritsch, J. M., R. J. Kane and C. R. Chelius, 1986: The contribution of mesoscale convective weather systems to the warm-season precipitation in the United States. *J. Clim. Appl. Meteor.*, **25**, 1333-1345.

Fujita, T. T., 1959: Precipitation and cold air production in mesoscale thunderstorm systems. *J. Meteor.*, **16**, 454-466.

______, 1978: Manual of Downburst Identification for Project Nimrod. Satellite and Mesometeorology Research Paper No. 156, Department of Geophysical Sciences, University of Chicago, 104 pp.

Gal-Chen, T., 1978: A method for the initialization of the anelastic equations: Implications for matching models with observations. *Mon. Wea. Rev.* **106**, 587-606.

______, and C. E. Hane, 1981: Retrieving buoyancy and pressure fluctuations from Doppler radar observations: A status report. *Atmos. Technol.*, **13**, 98-104.

______, and R. A. Kropfli, 1983: Deduction of thermodynamic properties from dual-Doppler radar observations in the PBL. *Preprints, 21st Conf. Radar Meteorology*, Edmonton, Amer. Meteor. Soc., 33-38.

Gallus, W. A., and R. H. Johnson, 1992: The momentum budget of and intense midlatitude squall line. *J. Atmos. Sci.*, **49**, 422-450.

Hertenstein, R. F. A., and W. H. Schubert, 1991: Potential vorticity anomalies associated with squall lines. *Mon. Wea. Rev.*, **119**, 1663-1672.

Houze, R. A., Jr., and P. V. Hobbs, 1982: Organization and structure of precipitating cloud systems. *Advances in Geophysics*, vol. 24, Academic Press, 225-315.

______, S. A. Rutledge, M. I. Biggerstaff, and B.F. Smull, 1989: Interpretation of Doppler weather radar displays of midlatitude mesoscale convective systems. *Bull. Amer. Meteor. Soc.*, **70**, 608-619.

______, B. F. Smull, and P. Dodge, 1990: Mesoscale organization of springtime rainstorms in Oklahoma. *Mon. Wea. Rev.*, **118**, 613-654.

Hoxit, L. R., C. F. Chappel, and J. M. Fritsch, 1976: Formation of mesolows or pressure troughs in advance of cumulonimbus clouds. *Mon. Wea. Rev.*, **104**, 1419-1428.

Johnson, R. H., and P. J. Hamilton, 1988: The relationship of surface pressure features to the precipitation and airflow structure of an intense midlatitude squall line. *Mon. Wea. Rev.*, **116**, 1444-1472.

______, W. A. Gallus, and M. D. Vescio, 1990: Near-tropopause vertical motion within the trailing stratiform region of a midlatitude squall line. *J. Atmos. Sci.*, **47**, 2200-2210.

______, and D. L. Bartels, 1992: Circulations associated with a mature-to-decaying midlatitude mesoscale convective system. Part II: Upper-level features. *Mon. Wea. Rev.*, **120**, 1301-1320.

Johnston, E. C., 1981: Mesoscale vorticity centers induced by mesoscale convective complexes. M. S. thesis, University of Wisconsin, 54 pp.

Jorgensen, D. P., and B. F. Smull, 1993: Mesovortex circulations seen by airborne Doppler radar within a bow-echo mesoscale convective system. *Bull. Amer. Meteor. Soc.*, **74**, 2146-2157.

Keenan, T. D., and S. A. Rutledge, 1993: Mesoscale characteristics of monsoonal convection and associated stratiform precipitation. *Mon. Wea. Rev.*, **121**, 352-374.

Leary, C. A. and R. A. Houze, Jr., 1979: Melting and evaporation of hydrometeors in precipitation from anvil clouds of deep tropical convection. *J. Atmos. Sci.*, **36**, 669-679.

LeMone, M. A., 1983: Momentum transport by a line of cumulonimbus. *J. Atmos. Sci.*, **40**, 1815-1834.

______, G. M. Barnes, and E. J. Zipser, 1984: Momentum flux by lines of cumulonimbus over the tropical oceans. *J. Atmos. Sci.*, **41**, 1914-1932.

Loehrer, S. M., 1992: The surface pressure features and precipitation structure of PRE-STORM mesoscale convective systems. M. S. Thesis, Dept. of Atmospheric Science, Colorado State University, 296 pp.

MacGorman, D.R., W. D. Rust, and V. Mazur, 1985: Lightning activity and mesocyclone evolution, 17 May 1981. *Preprints, 14th Conf. on Severe Local Storms,* Indianapolis, American Meteorological Society, 355-357.

Maddox, R. A., 1980: Mesoscale convective complexes. *Bull. Amer. Meteor. Soc.*, **61**, 1374-1387.

______, 1983: Large-scale meteorological conditions associated with mid-latitude mesoscale convective complexes. *Mon. Wea. Rev.*, **111**, 1475-1493.

Matejka, T. A., 1989: Pressure and buoyancy forces and tendencies in a squall line and their relation to its evolution. Preprints, *24th Conf. on Radar Meteorology.* Tallahassee, Amer. Meteor. Soc., 478-481.

Meitin, J. G., and J. B. Cunning, 1986: The Oklahoma-Kansas preliminary regional experiment for STORM Central (O-K PRE-STORM) Volume I. Daily Operations Summary. NOAA Tech Memo. ERL ESG-20, Boulder, CO 80303 313pp.

Menard, R. D., and J. M. Fritsch, 1989: A mesoscale convective complex-generated inertially stable warm core vortex. *Mon. Wea. Rev.*, **117**, 1237-1261.

Mohr, C. G., and L. J. Miller, 1983: A software package for Cartesian space editing, synthesis and display of radar fields under interactive control. Preprints, *21st Conf. on Radar Meteorology*, Edmonton, Alberta, Amer. Meteor. Soc., 569-574.

NCAR, 1984. The National STORM Program: STORM-Central Phase. Prepared by the National Center for Atmospheric Research, Boulder, CO, in consulation with the Interagency Team for STORM-Central. Boulder: NCAR.

O'Brien, J. J., 1970: Alternative solutions to the classical vertical velocity problem. *J. Appl. Meteor.*, **9**, 197-203.

Oye, R. and R. E. Carbone, 1981: Interactive Doppler editing software, *Proc. 20th Conf. Radar Meteorology*, Boston, Amer. Meteor. Soc., 683-689.

Rotunno, R., and J. B. Klemp, 1982: The influence of the shear-induced pressure gradient on thunderstorm motion. *Mon. Wea. Rev.*, **110**, 136-151.

______, _____, and M. L Weisman, 1988: A theory for strong, long-lived, squall lines. *J. Atmos. Sci.*, **45**, 463-485.

Roux, F., J. Testud, M. Payen, and B. Pinty, 1984: West-African squall-line thermodynamic structure retrieved from dual-Doppler radar observations. *J. Atmos. Sci.*, **41**, 3104-3121.

Rutledge, S. A., and D. R. MacGorman, 1988: Cloud-to-ground lightning activity in the 10-11 June 1985 mesoscale convective system observed during the Oklahoma-Kansas PRE-STORM project. *Mon. Wea. Rev.*, **116**, 1393-1408.

______, R. A. Houze, Jr., M. I. Biggerstaff, and T. Matejka, 1988: The Oklahoma-Kansas mesoscale convective system of 10-11 June 1985: Precipitation structure and single Doppler radar analysis. *Mon. Wea. Rev.*, **116**, 1409-1430.

______, C. Lu, and D. R. MacGorman: 1990. Positive cloud-to-ground lightning in mesoscale convective systems. *J. Atmos. Sci.*, **47**, 2085-2100.

Sawyer, J. S., 1946: Cooling by rain as a cause of the pressure rise in convective squalls. *Quart. J. Roy. Met. Soc.*, **72**, 168.

Schubert, W. H., J. J. Hack, P. L. Silva Dias, and S. R. Fulton, 1980: Geostrophic adjustment in an axisymmetric vortex. *J. Atmos. Sci.*, **37**, 1464-1484.

Skamarock, W. C., M. L. Weisman, and J. B. Klemp: 1994: Three-dimensional evolution of simulated, long-lived squall lines., *J. Atmos. Sci.*, in press.

Smull, B. F., and R. A. Houze, Jr. 1987: Rear inflow in squall lines with trailing stratiform precipitation. *Mon. Wea. Rev.*, **115**, 2869-2889.

______, and J. A. Augustine, 1993: Multiscale analysis of a mature mesoscale convective complex. *Mon. Wea. Rev.*, **121**, 103-132.

Stensrud, D. J., R. A. Maddox, and C. L. Ziegler, 1991: A sublimation-initiated mesoscale downdraft and its relation to the wind field below a precipitating anvil cloud. *Mon. Wea. Rev.*, **119**, 2124-2139.

Stumpf, G. J., R. H. Johnson, and B. F. Smull, 1991: The wake low in a midlatitude mesoscale convective system having complex organization. *Mon. Wea. Rev.*, **119**, 134-158.

Verlinde, I., and W. R. Cotton, 1990: Mesoscale vortex-couplet observed in the trailing anvil of a multi-cellular convective complex. *Mon. Wea. Rev.*, **118**, 993-1010.

Weisman, M. L., 1992: The role of convectively generated rear-inflow jets in the evolution of long-lived meso-convective systems. *J. Atmos. Sci.*, **49**, 1827-1847.

______, 1993: Genesis of severe, long-lived bow echoes. *J. Atmos. Sci.*, **50**, 645-670.

Zhang, D. L., 1992: The formation of a cooling-induced mesovortex in the trailing stratiform region of a midlatitude squall line. *Mon. Wea. Rev.*, **120**, 2763-2785.

______, and J. M. Fritsch, 1987: Numerical simulation of the mesoβ-scale structure and evolution of the 1977 Johnstown flood. Part II: Inertially stable warm-core vortex and convective complex. *J. Atmos. Sci.*, **44**, 2593-2612.

______, and J. M. Fritsch, 1988: A numerical investigation of a convectively generated, inertially stable, extratropical warm-core mesovortex over land. Part I: Structure and evolution. *Mon. Wea. Rev.*, **116**, 2660-2687.

Zipser, E. J., 1977: Mesoscale and convective-scale downdrafts as distinct components of squall-line circulation. *Mon. Wea. Rev.*, **105**, 1568-1589.